IMPERIAL COLLEGE LONDON

ELASTIC WAVE SCATTERING FROM RANDOMLY ROUGH SURFACES

by

Fan Shi

A thesis submitted to the Imperial College London for the degree of
Doctor of Philosophy

Department of Mechanical Engineering
Imperial College London
London SW7 2BX

August 2015

Declaration of Originality

The entire content presented in this thesis is the result of my independent research in the past three years under the supervision of Professor Mike Lowe. I have provided appropriate references wherever required in the thesis.

Fan Shi 11/10/2015

Copyright Declaration

Abstract

Elastic wave scattering from randomly rough surfaces and a smooth surface are essentially different. For ultrasonic nondestructive evaluation (NDE) the scattering from defects with smooth surfaces has been extensively studied, providing fundamental building blocks for the current inspection techniques. However, all realistic surfaces are rough and the roughness exists in two dimensions. It is thus very important to understand the rough surface scattering mechanism, which would give insight for practical inspections. Knowledge of the stochastics of scattering for different rough surfaces would also allow the detectability of candidate rough defects to be anticipated. Hence the main motivation of this thesis is to model and study the effect of surface roughness on the scattering field, with focus on elastic waves. The main content of this thesis can be divided into three contributions.

First of all, an accurate numerical method with high efficiency is developed in the time domain, for computing the scattered waves from obstacles with arbitrary shapes. It offers an exact solution which covers scenarios where approximation-based algorithms fail. The method is based on the hybrid idea to combine the finite element (FE) and boundary integral (BI) methods. The new method efficiently couples the FE equations and the boundary integral formulae for solving the transient scattering problems in both near and far fields, which is implemented completely in the time domain. Several numerical examples are demonstrated and sufficiently high accuracy is achieved with different defects. It enables the possibility for Monte Carlo simulations of the elastic wave scattering from randomly rough surfaces in both 2D and 3D.

The second contribution relates to applying the developed numerical method to evaluate the widely used Kirchhoff approximation (KA) for rough surface scattering. KA is a high-frequency approximation which limits the use of the theory for certain ranges of roughness and incidence/scattering angles. The region of validity for elastic KA is carefully examined for both 1D and 2D random surfaces with Gaussian spectra. Monte Carlo simulations are run and the expected scattering intensity

is compared with that calculated by the accurate numerical method. An empirical rule regarding surface parameters and angles is summarized to establish the valid region of both 2D and 3D KA. In addition, it is found that for 3D scattering problems, the rule of validity becomes stricter than that in 2D.

After knowing the region of validity, KA is applied to investigate how the surface roughness affects the statistical properties of scattered waves. An elastodynamic Kirchhoff theory particularly for the statistics of the diffused field is developed with slope approximations for the first time. It provides an analytical expression to rapidly predict the expected angular distribution of the scattering intensity, or the scattering pattern, for different combinations of the incidence/scattering wave modes. The developed theory is verified by comparison with numerical Monte Carlo simulations, and further validated by the experiment with phased arrays. In particular the derived formulae are utilized to study the effects of the surface roughness on the mode conversion and the 2D roughness caused depolarization, which lead to unique scattering patterns for different wave modes.

Acknowledgment

“知行合一。” ***‘Knowledge as action.’***

王阳明 (1472 BC-1529 BC, 明朝)

Yangming Wang (Philosopher) （1472 BC-1529 BC, Ming Dynasty, China)

Firstly, I would like to express my deepest gratitude to my supervisor Professor Mike Lowe for his excellent guidance and continued encouragement in the past three years. His patience and generosity have allowed me to investigate many research topics I am interested in, and to explore more unknown beyond the scope of the project with enthusiasms. From him I have not only learned the academic knowledge, but also the philosophy of life. I would also like to thank Professor Richard Craster from the Department of Mathematics for invaluable discussions about mathematics of wave motion, for organizing regular ‘wave meeting’ from which I have broadened my interests to many different topics, and for significant help to improve my academic writing.

A special thank to Professor Jennifer Michaels from Georgia Institute of Technology for introducing me to the area of NDE, and for training me with important skills for academic research. I want to give deep appreciations to Dr. Zheng (David) Fan and Dr. Xiaoyu (Trist) Xi for providing me with many valuable suggestions during my Ph. D, Dr. Wonjae Choi for helping me with numerical models in my first year with a lot of patience, and Dr. Elizabeth Skelton for discussions about numerical methods. I also want to acknowledge Professor Peter Cawley and Dr. Frederic Cegla for organizing such a great research group.

I must thank all my previous and current colleagues in the NDT group for their help and for creating a very enjoyable working environment, and the NDT squash team for organizing squash events every week. I would also like to extend my thanks to my flatmates Jie Zhou and Xiaotang Gu for all the movie nights, and the Texas poker nights we share.

Furthermore, I need to acknowledge the Engineering and Physical Science Research Council (EPSRC), Amec Foster Wheeler, EDF energy and Rolls Royce Marine for funding this work.

Finally but the most importantly, I am forever indebted to my family: my father Zhubin Shi and my mother Xiaolu You, who have raised me with a strong interest in physics, mathematics and engineering since I was a child. I must thank my parents for their continued support, encouragement and understanding throughout my Ph. D, although we are separated by a flight of more than 12 hours from London to Nantong. To them I dedicate this thesis.

Contents

List of Figures

Chapter 1

Introduction

1.1 Background and motivation

Conventional ultrasonic techniques for nondestructive evaluation (NDE) are typically based on understanding of the scattering response from defects with smooth geometries, for instance, a side-drilled hole (SDH) or a flat crack. However, all realistic defects are generally 'rough' in a statistical sense when formed naturally or during a manufacturing process. Examples showing the scattering patterns from surfaces with different levels of roughness are demonstrated in Fig. 1.1(a) to (c) [1]. As can be seen, the surface roughness has a significant effect on the scattering amplitude and its angular distribution. A strong main lobe is observed when the surface is flat or only slightly rough. However, the main lobe is significantly attenuated with a wide distribution as the surface becomes very rough. In addition, the scattering waveform also becomes much more complicated compared with the response from a flat surface as shown in Fig. 1.2(a) and (b), which are taken from the paper by Ogilvy [2].

In order to provide the reader with a general physical understanding of the effect of the height variation (roughness) on the scattered waves, and also to identify the key features and point to the needs for research and the objectives of the work of the thesis, a general examination of the effect of the surface roughness on scattering is summarized qualitatively [4], as illustrated in Fig. 1.3. According to Huygens' principle, each point on the surface acts as a secondary source, and the scattered waves at an observation point is a superposition of all contributions from these

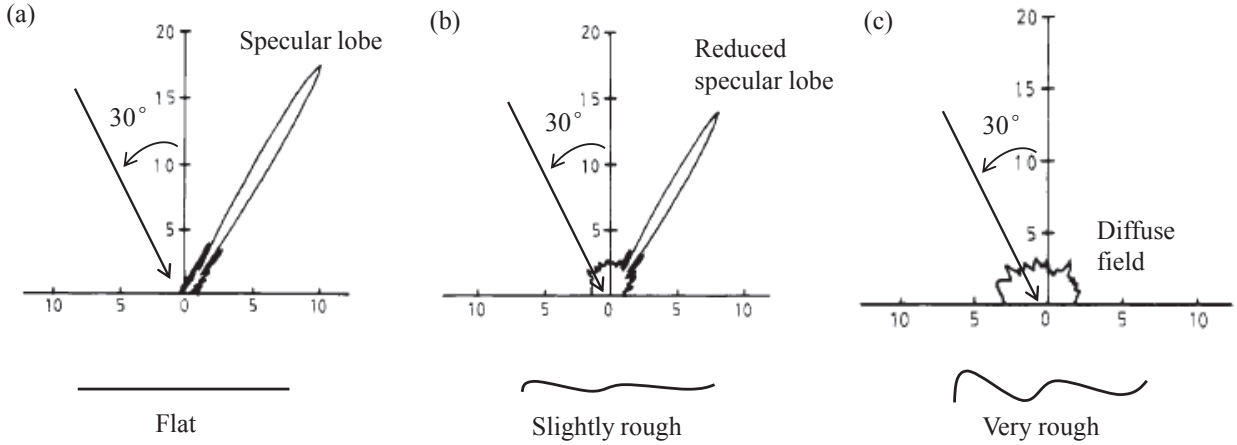

Figure 1.1: Mean intensities of scattered waves averaged over 20 realizations for an incident angle of 30^o from surfaces with different roughness (Pictures from [1]). (a) Flat surface. (b) Slightly rough. (c) Very rough.

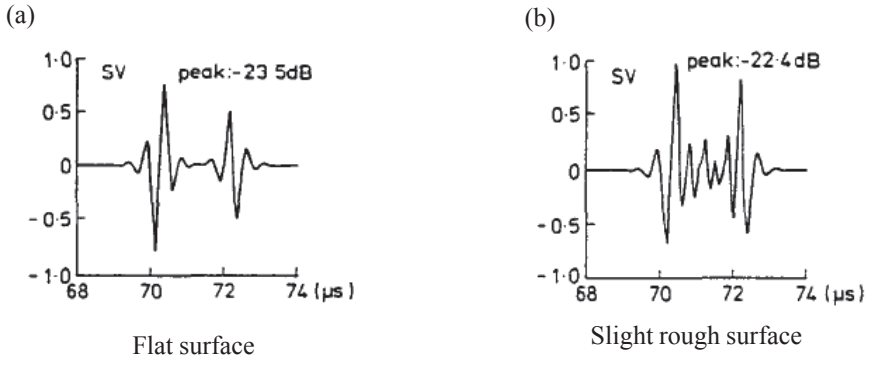

Figure 1.2: Received shear wave signals from a flat defect and a slightly rough defect in a time-of-flight inspection (Pictures from [2]).

surface points. The phase difference of the scattered waves from two surface points in 2D can be expressed as [4]:

$$\Delta\phi = k(\hat{\boldsymbol{k}}_{\boldsymbol{in}} - \hat{\boldsymbol{k}}_{\boldsymbol{sc}}) \cdot \boldsymbol{\Delta r} = k[(\sin\theta_i - \sin\theta_s)\Delta x - (\cos\theta_i + \cos\theta_s)\Delta h] \qquad (1.1)$$

where $\hat{\boldsymbol{k}}_{\boldsymbol{in}}$ and $\hat{\boldsymbol{k}}_{\boldsymbol{sc}}$ are the unit incident and scattering vectors, θ_i and θ_s are the incidence and scattering angles measured with respect to the vertical as shown in Fig. 1.3. $\boldsymbol{\Delta r} = (\Delta x, \Delta h)$ is the spatial variation of two surface points.

Starting from the scattering from a flat surface of a finite length when $h(x) = 0$,

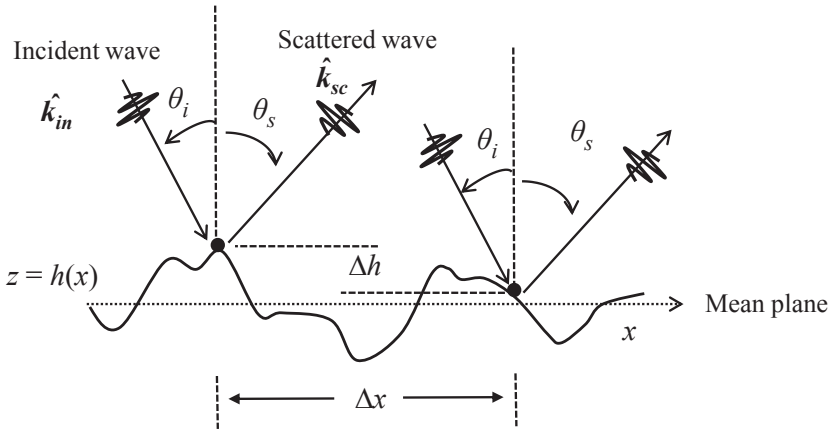

Figure 1.3: Physical illustration of the interference of waves scattered from a rough surface in 2D.

Eq. (1.1) can be simplified as:

$$\Delta\phi = k(\sin\theta_i - \sin\theta_s)\Delta x \tag{1.2}$$

Around the specular direction $\Delta\phi$ vanishes because $\theta_i = \theta_s$. The waves constructively interfere, forming a strong scattering main lobe with a very sharp angular distribution shown in Fig. 1.1(a). Away from the specular direction, the difference of the phase becomes larger and the destructive interference dominates, contributing to small side lobes at non-specular directions.

If the roughness is now imposed, implying that Δh is nonzero, in the specular direction the phase difference is:

$$\Delta\phi = 2k\cos\theta_i\Delta h \tag{1.3}$$

When the roughness (Δh) is small, the phase difference $\Delta\phi$ is also small and the waves will constructively interfere. On the contrary, as Δh increases $\Delta\phi$ becomes larger, and the waves start destructively interfering with each other. Hence the scattering amplitude is attenuated by the appearance of the roughness. In the time domain, it leads to a large variation in the arrival time for scattered waves from different points on the surface. Accumulation of these waveforms leads to a complicated signal as shown in Fig. 1.2(b) with a longer duration but smaller amplitude. At off-specular directions, $\Delta\phi$ is determined by both the height difference Δh and

the separation distance Δx in Eq. (1.1) . Generally the scattered waves destructively interfere, and the scattering energy is much more widely distributed than that from a smooth surface shown in Fig. 1.1(b) and (c).

Based on the above consideration of the phase difference, the scattering displacement field can be decomposed into the coherent and the diffuse parts:

$$u^t = u^c + u^d \tag{1.4}$$

The coherent component physically represents contributions from scattered waves relatively in phase, and hence it is concentrated around the specular direction. On the other hand, waves with random phases form the diffuse field, whose energy is widely spread for all angles and dominates at the off-specular angles. As a result, the coherent displacement u^c equals to the ensemble averaging $< u^t >$, as the averaging of u^d leads to zero due to the phase cancellation. The ensemble averaging $< \cdot >$ refers to the expectation of one quantity, and it can be replaced by a sample averaging from different realizations of surfaces, with a calculated response for each, for example using computer simulations. This is also known as the Monte Carlo method.

In reality, NDE inspectors are interested in the expectation of the scattering amplitude instead of the phase since the magnitude of the signal determines the detectability. The phase information can be avoided by only considering the intensity:

$$< I^t >= I^c + < I^d >= u^c \bar{u^c} + < u^d \bar{u^d} > \tag{1.5}$$

where $\bar{u}^c$ and $\bar{u}^d$ refer to the conjugate values of u^c and u^d respectively. The coherent intensity dominates when the surface roughness is small, while for high roughness the diffuse field is dominant. The expected total intensity can be obtained by a sample average of intensities computed from many realizations of surfaces with the same statistical profile. Alternatively it can be predicted analytically for example using the Kirchhoff theory that will be shown in Chapter 5.

With this general background of the physics, we have the basis to look at the current problems and the needs for the research that is reported in this thesis. It can be

seen from the above explanations that due to the complexity caused by the surface roughness, the unpredictable scattering behavior would possibly limit the inspection and sizing ability based on previous studies of the scattering from smooth defects. For instance, commonly used detection procedures seek an amplitude threshold of the inspection signal as an alarm to judge whether there is a defect or not. However, as noticed in Fig. 1.1(a) to (c), due to the increased diffuse effects the roughness greatly attenuates the scattering amplitude, which might be below the threshold to miss the opportunity to detect cracks [5]. Therefore for industrial applications, it is necessary to understand how the roughness changes the ultrasonic response, in order to improve the probability of detection (POD). In addition, wave scattering from randomly rough surfaces has been a common problem for a long time in many other fields, such as electromagnetic wave reflection from glaciers [6] and forests [7] for remote sensing, and for acoustic wave reflection from sea surfaces [8]. However, very few studies can be found in the community of elastic waves [9–11], in particular there seems to be a lack of general theoretical solutions to represent the elastodynamic scattering. Hence from a physical point of view, it is very important to study the surface scattering mechanism for elastic waves, which would serve as fundamental building blocks for industrial applications. Therefore the main motivation of this thesis is to investigate the effects of roughness on elastic wave scattering behavior, by developing both computational tools and elastodynamic theories.

A common problem that restricts the studies of wave scattering from randomly rough surfaces is the shortage of accurate and efficient numerical tools, especially in 3D [12] for either scalar or vector waves. For elastic waves it is even more difficult because of the increased number of degrees of freedom and the inclusion of mode conversions. A variety of numerical methods can be used and they are roughly divided into two categories: (1) volume meshing algorithms, such as the finite difference (FD) [13, 14] and finite element (FE) methods [15, 16], (2) boundary integration approaches, such as the boundary element (BE) method [17, 18], and methods based on Huygens' principle, such as the distributed point source method (DPSM) [19]. Each method has pros and cons in terms of the computational efficiency and generality. Recently for elastic wave scattering problems hybrid methods have been developed with application in NDE [20–22], which combines the volume meshing and the boundary integral methods. Some of the original hybrid methods have been

performed in the frequency domain in the far field, because the aim is to extract the scattering matrix which is frequency dependent [23]. However, in many situations the simulated full waveforms are needed, for instance with application to size the crack using the time-of-flight-diffraction (TOFD) technique [24]. In addition, in a real NDE inspection the transducer might not be located strictly within the far field from the defect. Therefore the first motivation is to develop an efficient numerical tool to calculate the transient elastic wave scattering in both near and far fields, which can be used to simulate the scattering from rough surfaces in 2D and 3D.

Efficient numerical methods can incorporate all of the scattering phenomena, so delivering more accurate results. However, they are still time consuming for any Monte Carlo approach as many simulations need to be run using hundreds or thousands of surface realizations. In contrast, approximation based approaches enable a rapid calculation of the scattering field, among which the Kirchhoff approximation (KA) is the most widely used [1, 2, 6, 25–27]. One essential problem is to know when the use of KA for scattering by randomly rough surfaces is accurate, in terms of the roughness and the scattering/incidence angle. Several attempts have been made to evaluate the validity of the KA for both scalar [8, 28, 29] and vector waves [30] during the history of this topic, while far fewer studies can be found for elastic waves [23, 31]. In addition, all previous studies have been limited to 2D simulations due to restrictions of the computational methods. However, the surface scattering in real life is inherently a 3D process due to the roughness in one additional direction, and therefore the behaviour in 3D with a 2D rough surface is expected to be different from that in 2D with a 1D surface. Hence the second motivation is to carefully evaluate the validity of KA in both 2D and 3D for elastic wave scattering from randomly rough surfaces, by comparison with the efficient numerical method developed in this thesis.

It is important to know the expectation of the scattering intensity and its angular distribution, as the information can be used for optimizing the detection plan by selecting reasonable inspection angles and frequencies. The expected value can be obtained using the sample average of the quantities via the Monte Carlo approach using the numerical method or the Kirchhoff model [2]. However, it is not easy to draw out the inner connection between the roughness and the scattered waves

from purely numerical data. Analytical solutions provide alternatives as they can offer simple mathematical expressions to represent the mean scattering intensity. The surface statistics are embedded in the formulae so that the inner relationship between the scattering properties and the roughness can be revealed explicitly.

The Kirchhoff approximation is a powerful tool and it has been utilized for deriving the theoretical solution for acoustic and electromagnetic waves [4, 28, 32]. For elastic waves analytical expressions can be found for the coherent intensity I^c at the specular angle [9]. However, no analytical solutions for the diffuse intensity have been developed so far, because unlike scalar waves the mode coupling on the surface leads to it being unfeasible to separate the surface gradient term from the boundary integral [9]. Therefore the final motivation of this thesis concerns the development of an analytical solution with the elastodynamic KA to represent the mean scattering intensity from the knowledge of the surface statistics.

1.2 Outline of the thesis

The main contributions of this thesis are generally divided into three chapters as shown in Fig. 1.4 with a clear logical flow. Each contribution serves as an essential prerequisite for its later contribution. Chapter 3 describes the development of an efficient numerical method implemented in the time domain to solve elastic wave scattering problems, which is then used as a benchmark in Chapter 4 to evaluate the performance of the elastodynamic Kirchhoff approximation in both 2D and 3D. After establishing the range of validity of KA, it is utilized in Chapter 5 to derive theoretical formulae to represent the expected scattering intensity, with application to analyzing the effects of roughness on the mode conversion. Specifically, subsequent to the introductory remarks in this chapter, the thesis is structured in the following manner:

Chapter 2 first reviews the background of randomly rough surfaces and corresponding statistical variables and functions. The purpose of this chapter is to provide the reader with prior knowledge of how the surface roughness is characterized statistically. Typical surface models are introduced including the most commonly used

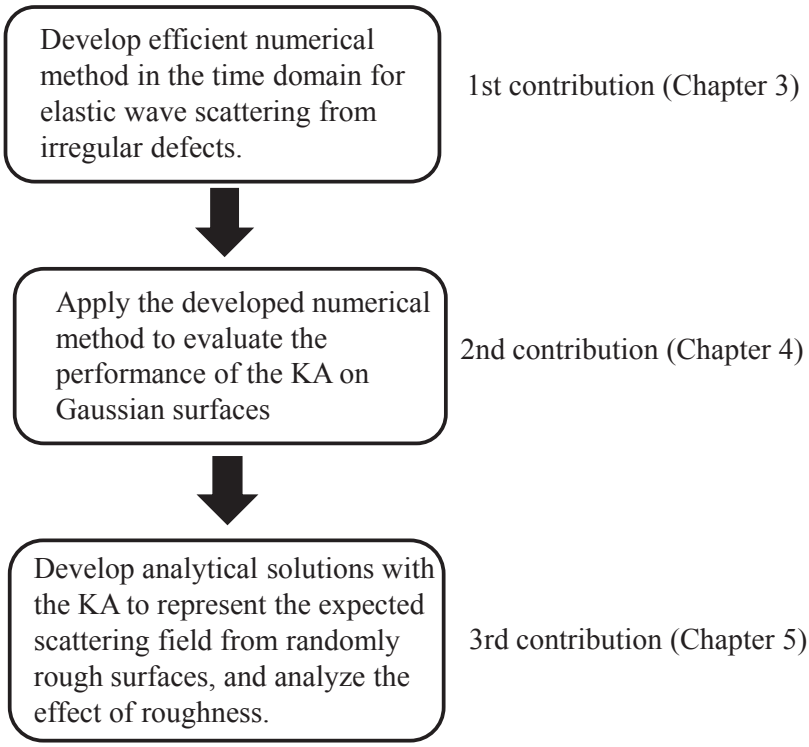

Figure 1.4: A flow chart showing the logical link between the three key contributions of the thesis.

Gaussian surface. A variety of generation methods are briefly illustrated, which can be used for producing required surface height data with different realizations.

Chapter 3 describes the development of an efficient and accurate numerical method to calculate the transient elastic wave scattering signals from irregular defects. A literature review of the main existent numerical methods is given including those implemented in a hybrid manner. Formulae and numerical implementations of a new approach using a local FE representation together with a boundary integral are described, and a numerical study is shown to find the minimum distance between the transducer and the defect beyond which the boundary integral is accurate. The new method is validated by several numerical examples including scatterers with different geometries and boundary conditions in both 2D and 3D. In addition, the new approach is applied to study the scattering from a realistic non-spherical void with irregular surfaces.

In Chapter 4, the numerical method is utilized as a benchmark to investigate the region of validity of the KA for elastic wave scattering from rough surfaces. Monte Carlo simulations are performed with both methods on Gaussian surfaces in 2D and 3D. Through comparison of the mean scattering amplitude, general rules are summarized, which provide empirical criteria to judge when the use of the elastodynamic KA is reasonable given a candidate rough defect. In particular it is found that the criteria in 3D are stricter than those in 2D, regarding the levels of the roughness and the range of the incidence/scattering angles.

Chapter 5 presents an elastodynamic theory for the expected scattering intensity, particularly for the diffuse field. Analytical formulae are derived by incorporation of the surface statistics into the expressions, in order to link the roughness with the scattering properties. During the derivation, slope approximations are utilized using the theory of 'specular points' which enables the analytical manipulation of the ensemble averaging of the intensity. The derived formulae are verified by comparison with sample averaging from numerical Monte Carlo simulations. Furthermore, experiments with phased arrays are performed and the results show good agreements with the theory. The elastodynamic theory is then applied to analyze the effects of roughness and elasticity on the mode conversion, which leads to a considerable

change of the scattering intensity and the angular distribution. Significant amounts of the energy of the incident waves are found to be mode converted especially away from the backscattering direction. The mode conversion effect is more severe as the roughness or the ratio of shear to compressional wave speed increases. In addition, the depolarization that describes the conversion of the in-plane motion into the out-of-plane motion, caused by the appearance of the 2D roughness is theoretically investigated, and it is found that the depolarization factor for the diffuse field does not rely on the actual value of the roughness.

Chapter 6 summarizes the findings in the thesis and proposes future work.

Chapter 2

Rough Surfaces

2.1 Background

In this chapter, the statistical methods used to characterize randomly rough surfaces are provided, including statistical parameters and some of the most widely used surface models. In addition, generation methods to produce surface data are introduced for the computer simulation. This chapter mainly aims at offering the reader essential background knowledge of the rough surface.

It is not easy to predict shapes of rough surfaces because they are formed during a process with 'uncertainty' such as fatigue, corrosion and fracture. As a consequence, the surface height is a random process as a function of space, which can only be described by some statistical approaches [32]. In reality no two surfaces are exactly identical, but a group of different surfaces following the same statistical description can be classified into the same category. Using an appropriate statistical model is important for the study of the scattering behavior. In this way the question of 'how the surface random shape affects the scattered field' is generalized to 'how the statistical parameters (roughness) affect the statistics of the scattered field'. In practice, it allows one to obtain a generic rule with certain confidence on the detectability of candidate rough defects to be anticipated.

Before introducing surface parameters, two assumptions are needed to reduce the range of surfaces under investigation. First of all, all surfaces are assumed to be ergodic [32]. It means that any ensemble averaging can be replaced by a spatial av-

eraging once the surface area is sufficiently large to guarantee enough sample points. Furthermore, stationarity [32] is assumed through most part of the thesis. It indicates that the statistics at one surface point are independent of its position.

Assume that the deviation of the surface from the mean flat plane is a random process $h(x, y)$, which is called the surface height function. The probability density function (pdf) $p(h)$ represents the probability that the surface height lies between h and $h+\Delta h$, where $\Delta h \to 0$. The Gaussian pdf has been the most widely used historically [4, 32], and is also applied here as an example. The mathematical form of the Gaussian pdf is:

$$p(h) = \frac{1}{\sigma\sqrt{2\pi}} \exp(-\frac{h^2}{2\sigma^2}) \tag{2.1}$$

The mean is always assumed to be zero [4], and the root mean square (RMS) height σ according to definition is:

$$\sigma = \sqrt{< h^2 >} = \sqrt{\frac{1}{N}\sum_{i=1}^{N} h_i^2}. \tag{2.2}$$

where <> denotes the ensemble averaging, which is defined as the mean or the expectation of a quantity. The second part of Eq. (2.2) is an empirical formula using the sample averaging. Henceforth, the ensemble averaging is represented numerically as the sample averaging once the number of sampling points N is sufficiently large. The RMS σ determines the vertical range of the height but it cannot represent the lateral variation of the height. A correlation function is thus needed in conjunction with σ to fully represent a surface, and it is defined as:

$$C(\boldsymbol{R}) = \frac{< h(\boldsymbol{r})h(\boldsymbol{r}+\boldsymbol{R}) >}{\sigma^2} \tag{2.3}$$

where $\boldsymbol{r}$ is the position of one surface point, and $\boldsymbol{R}$ is the separation distance between two points. The correlation function is a measure of how the two surface points with a separation of $\boldsymbol{R}$ correlate with each other. It can be seen that the correlation function has a unit value when $|\boldsymbol{R}| = 0$, and decays to zero when $R \to \infty$.

Another way to characterize the surface instead of σ and $C(\boldsymbol{R})$ is to use the power

spectrum, which is defined as the Fourier transform of C($\boldsymbol{R}$):

$$P(\boldsymbol{k}) = \frac{\sigma^2}{(2\pi)^2} \int_{-\infty}^{\infty} C(\boldsymbol{R}) e^{i\boldsymbol{k}\cdot\boldsymbol{R}} d\boldsymbol{R} \tag{2.4}$$

Substituting the correlation function Eq. (2.3) into Eq. (2.4) yields:

$$P(\boldsymbol{k}) = lim_{A_m \to \infty} \frac{1}{A_m (2\pi)^2} \left| \int_{-A_m/2}^{A_m/2} h(\boldsymbol{r}) e^{i\boldsymbol{k}\cdot\boldsymbol{r}} d\boldsymbol{r} \right|^2 \tag{2.5}$$

where A_m is the area of the surface, and $P(\boldsymbol{k})$ refers to the magnitude of the height in the wavenumber domain, which includes both the vertical and the lateral variation of the height. According to Parseval's theorem, the total energy of the power spectrum is equivalent to the variance of the surface height:

$$\int_{-\infty}^{\infty} P(\boldsymbol{k}) d\boldsymbol{k} = \sigma^2 \tag{2.6}$$

Another important parameter is the characteristic function, which is defined as the Fourier transform of the probability density function:

$$\chi(s) = \int_{-\infty}^{\infty} p(h) e^{ish} dh \tag{2.7}$$

The one-dimensional characteristic function is important to determine the coherent scattering intensity from random rough surfaces.

In a similar manner, the two-dimensional characteristic function is given by:

$$\chi_2(s_0, s_1, \boldsymbol{R}) = \int_{-\infty}^{\infty} p_2(h_0, h_1, \boldsymbol{R}) e^{i(s_0 h_0 + s_1 h_1)} dh_0 dh_1 \tag{2.8}$$

where $p_2(h_0, h_1, \boldsymbol{R})$ is the two-point height probability distribution, implying the probability that the height of one surface point is within h_0 and $h_0 + \Delta h$ and the height of the other surface point with a distance of $\boldsymbol{R}$ is within h_1 and $h_1 + \Delta h$. The two-dimensional characteristic function is useful to derive the ensemble averaging of the phase difference of scattered waves from two surface points. Hence it determines the diffuse scattering intensity that will be shown in Chapter 5.

2.2 Surfaces with Gaussian spectra

Historically most studies have been focused on surfaces with Gaussian spectra [1, 2, 25, 28], with the correlation function C($\boldsymbol{R}$) following a Gaussian function:

$$C(\boldsymbol{R}) = \frac{< h(\boldsymbol{r})h(\boldsymbol{r}+\boldsymbol{R}) >}{\sigma^2} = \exp\left[-\left(\frac{x^2}{\lambda_x^2} + \frac{y^2}{\lambda_y^2}\right)\right]. \tag{2.9}$$

In Eq. (2.9), λ_x and λ_y are called the correlation lengths in the x- and y- directions, as the distance over which the correlation function falls by $1/e$. If isotropy is assumed for the surface ($\lambda_x = \lambda_y = \lambda_0$), the correlation function can be simplified as:

$$C(R) = \exp\left(-\frac{R^2}{\lambda_0^2}\right) \tag{2.10}$$

with $R^2 = x^2 + y^2$.
The power spectrum can be calculated according to Eq. (2.4) as:

$$P(k_x, k_y) = \frac{\sigma^2\lambda_x\lambda_y}{4\pi}\exp(-\frac{k_x^2\lambda_x^2}{4})\exp(-\frac{k_y^2\lambda_y^2}{4}) \tag{2.11}$$

The two-point height probability density function is:

$$p_2(h_0, h_1, \boldsymbol{R}) = \frac{1}{2\pi\sigma^2\sqrt{1-C^2(\boldsymbol{R})}}\exp\left[-\frac{h_0^2 + h_1^2 - 2h_0h_1C(\boldsymbol{R})}{2\sigma^2[1-C^2(\boldsymbol{R})]}\right] \tag{2.12}$$

For surfaces with Gaussian spectra, the pdf of the height gradient $p_g(\frac{\partial h}{\partial x}, \frac{\partial h}{\partial y})$ can be expressed analytically as:

$$\begin{aligned} p_g(\frac{\partial h}{\partial x}, \frac{\partial h}{\partial y}) &= \frac{\lambda_x\lambda_y}{4\pi\sigma^2}\exp[-\frac{\lambda_x^2(\frac{\partial h}{\partial x})^2 + \lambda_y^2(\frac{\partial h}{\partial y})^2}{4\sigma^2}] \\ &= \frac{\lambda_x}{2\sqrt{\pi}\sigma}\exp[-\frac{\lambda_x^2(\frac{\partial h}{\partial x})^2}{4\sigma^2}] \cdot \frac{\lambda_y}{2\sqrt{\pi}\sigma}\exp[-\frac{\lambda_y^2(\frac{\partial h}{\partial y})^2}{4\sigma^2}] \\ &= p_g(\frac{\partial h}{\partial x}) \cdot p_g(\frac{\partial h}{\partial y}) \end{aligned} \tag{2.13}$$

The joint probability density function $p_g(\frac{\partial h}{\partial x}, \frac{\partial h}{\partial y})$ equals to the multiplication of the corresponding marginal pdfs in the x- and y- directions. It implies that $\frac{\partial h}{\partial x}$ and $\frac{\partial h}{\partial y}$ are assumed to be two independent variables.

2.3 Other surface models

Surfaces with Gaussian spectra have been the most widely used [1, 2, 25, 28], and some crack profiles are found experimentally to have Gaussian spectra [23]. However, there also exist several other surface profiles which are of interest particularly for elastic waves, with application in NDE and seismology. For example, literature can be found regarding the scattering from the surface with an exponential correlation function [33, 34]:

$$C(\boldsymbol{R}) = \exp\left[-\left(\frac{|x|}{\lambda_x} + \frac{|y|}{\lambda_y}\right)\right]. \tag{2.14}$$

Then the power spectrum can be derived as:

$$P(k_1, k_2) = \frac{\sigma^2}{\lambda_x \lambda_y \pi^2} \frac{1}{(1/\lambda_x^2 + k_x^2)} \frac{1}{(1/\lambda_y^2 + k_2^2)} \tag{2.15}$$

As noticed a power law with an order of two exists in Eq. (2.15).

Figure 2.1(a) shows a comparison of the Gaussian and exponential power spectra with the same RMS and the correlation length. One may notice that the power spectrum of the exponential correlation function demonstrates a relatively long tail in the high frequency region. As a consequence, the exponential power spectrum generates a surface with finer details due to more high frequency components than the Gaussian spectrum. Figure 2.1(b) plots surface profiles with the Gaussian and the exponential power spectra, respectively. As expected, the exponential surface appears to have more short-wavelength roughness compared with the Gaussian surface.

Another commonly seen surfaces have fractal or self-affine properties, which may be generated from fracture or deposition process [35]. Such surfaces remain invariant for any real number q under transformation of the form:

$$(x, y, h) \rightarrow (qx, qy, q^H h) \tag{2.16}$$

Where H is called the roughness or Hurst exponent. In this case the conventional pdf $p(h)$ needs to be replaced by the new pdf $p(\Delta h, R)$, referring to the probability of having a height difference Δh over the distance R. Assuming a Gaussian height

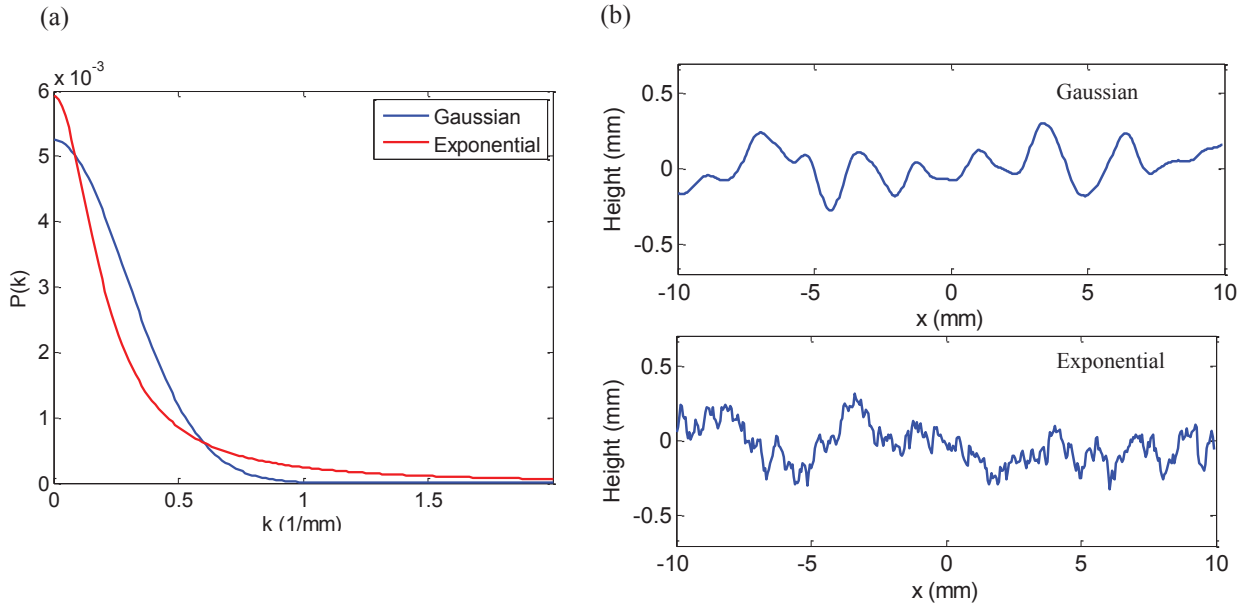

Figure 2.1: Comparison of the Gaussian and the exponential power spectra and the corresponding rough surfaces. (a) power spectra when $\sigma = 0.155$mm and $\lambda_0 = 0.775$mm. (b) Rough surface profiles with Gaussian and exponential power spectra when $\sigma = 0.155$mm and $\lambda_0 = 0.775$mm.

distribution, $\mathrm{p}(\Delta h, R)$ can be expressed as:

$$p(\Delta h, \Delta x) = \frac{1}{\sqrt{2\pi} l (1-H)} \exp[-\frac{1}{2}(\frac{\Delta h}{l(1-H)\Delta x^H})] \tag{2.17}$$

Where l is called the topothesy parameter, implying the length scale. It is beyond the scope of this thesis and for more details about the fractal surface one may refer to [36]. This thesis focuses on surfaces with Gaussian spectra, albeit the methodology used for studying the scattering behavior can be applied for other surface models as well.

2.4 Generation Method

To generate many realizations of surfaces with the same statistical profile, it is necessary to adopt some numerical method. The generated surfaces are often used for Monte Carlo simulations. It should be noted that each generated surface profile, also known as one realization, does not remain identical given the random nature of the surface. However, for given roughness parameters, all realizations should follow

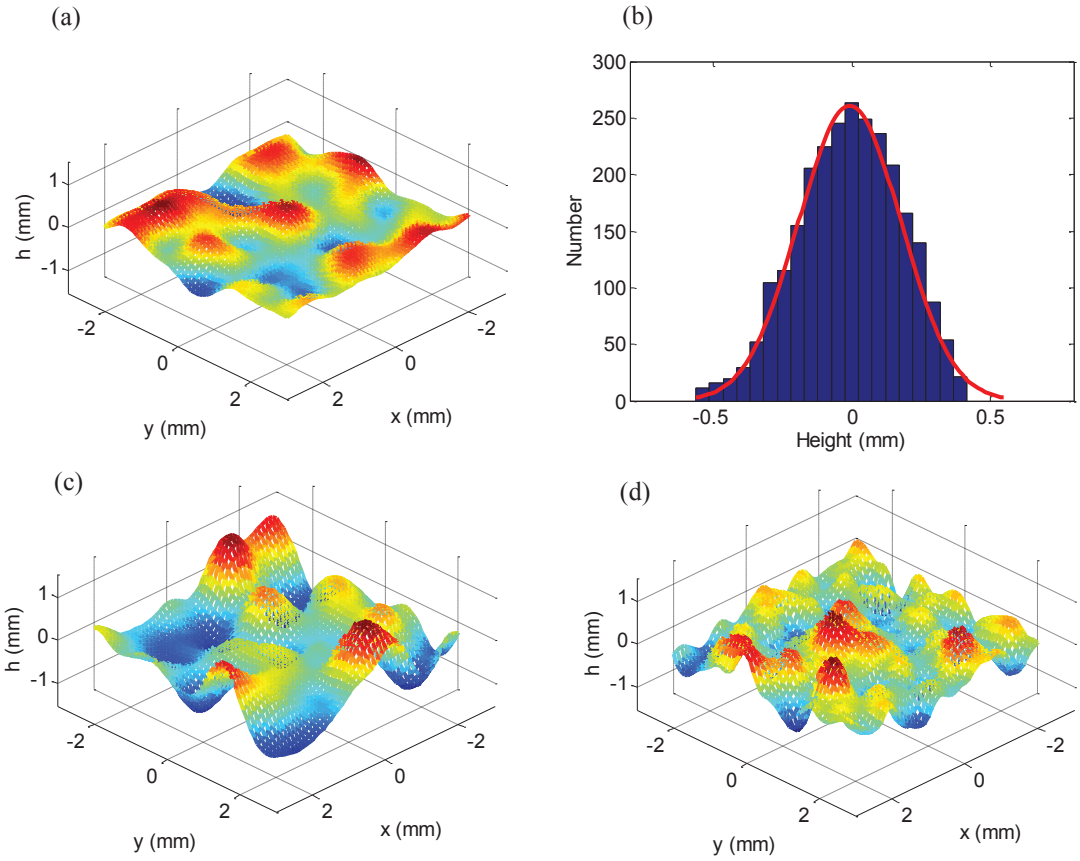

Figure 2.2: 3D isotropic Gaussian rough surface profiles. (a) $\sigma = 0.258$mm, $\lambda_0 = 0.775$mm. (b) Height distribution of the surface shown in (a) and the corresponding Gaussian fit curve. (c) $\sigma = 0.517$mm, $\lambda_0 = 0.775$mm. (d) $\sigma = 0.258$mm, $\lambda_0 = 0.388$mm.

the same statistical model. A summary of commonly used generation methods are introduced here briefly.

2.4.1 Moving average method

The moving average method is easy to apply when the RMS σ and the correlation length λ_0 are both known. This method produces a series of uncorrelated random numbers v, which are convolved with a set of weighting functions w to calculate the required surface height data [1].

For a surface with the Gaussian correlation function, the required form of the weight

w is:

$$\begin{aligned} w_i &= \exp[-2(i\Delta x)^2/\lambda_0^2], && \text{1D surface} \\ w_{ij} &= \exp[-2(i\Delta x)^2/\lambda_x^2 - 2(j\Delta y)^2/\lambda_y^2], && \text{2D surface} \end{aligned} \tag{2.18}$$

The random variable v follows the Gaussian distribution with a zero mean, and the RMS σ_v can be obtained according to the RMS σ of the surface height and the values of each weight:

$$\sigma_v^2 = \sigma^2 / \sum_{j=-M}^{M} w_j^2 \tag{2.19}$$

By convolving w with the random variable v, the surface height h is given by:

$$\begin{aligned} h_i &= \sum_{j=-M}^{M} w_j v_{j+i}, && \text{1D surface} \\ h_{pq} &= \sum_{i=-N}^{N} \sum_{j=-M}^{M} w_{ij} v_{p+i,q+j}, && \text{2D surface} \end{aligned} \tag{2.20}$$

Fig. 2.2(a) and (b) show one realization of a 2D isotropic Gaussian rough surface generated using the moving average method and the corresponding height distribution function. By increasing σ or decreasing λ_0, the original surface changes the shape as shown in Fig. 2.2(c) and (d).

2.4.2 Spectral method

The spectral method can be used to produce surfaces once the power spectrum is known [28]. The idea is to filter the spectrum with some random complex numbers, and then apply a Fourier transform to recover the surface profile. Specifically, according to the definition, the power spectrum for a 1D surface equals to:

$$P(k) = lim_{A_m \to \infty} \frac{1}{2\pi A_m} \left| \int_{-A_m/2}^{A_m/2} h(x) e^{-ikx} dx \right|^2 \tag{2.21}$$

The surface height can be expressed as a summation of the Fourier components:

$$h(x_n) = \frac{1}{A_m} \Sigma_{j=-N/2}^{N/2-1} H(k_j) e^{ik_j x_n} \tag{2.22}$$

where each Fourier coefficient equals to:

$$H(k_j) = [2\pi A_m P(k_j)]^{1/2} \begin{cases} [N(0,1) + iN(0,1)]/\sqrt{2}, & j \neq 0, N/2, \\ N(0,1), & j = 0, N/2, \end{cases} \tag{2.23}$$

In Eq. (2.23), $N(0,1)$ represents independent random variables following a Gaussian distribution with a zero mean and a unit variance.

2.5 Summary

In this chapter, a brief review of the random rough surface is provided. Commonly used statistical parameters and functions are shown to characterize the surface. Furthermore, numerical methods are introduced to generate data of the surface height, given the statistics of a candidate rough surface. The formulae of the statistical parameters will be used to deduce the expected scattering amplitude, and the generation methods will be implemented for Monte Carlo simulations in later chapters.

Chapter 3

Efficient Numerical Method for Elastic Wave Scattering in the Time Domain

3.1 Introduction

In this chapter, an efficient and accurate numerical method is developed and implemented in the time domain, for computing elastic wave scattering from complex scatterers in both near and far fields. First of all a thorough literature review is given on a variety of methods for the scattering problem in an unbounded domain. The new method utilizing the hybrid idea is then described, which efficiently couples the finite element computation in a small local region and the global boundary integral, in order to overcome previous computational challenges especially for 3D scattering problems. Numerical advantages regarding the performance of the method in the near field are also discussed. Several numerical examples are run to test the accuracy of the new method, which will be used in later chapters for simulating wave scattering from randomly rough surfaces.

There is a growing interest in elastic wave scattering from rough surfaces nowadays. For instance, seismologists have investigated the reflected seismic waves from a randomly rough surface for time-lapse monitoring techniques [26, 37] and inversion purposes [10]. In the area of NDE, researchers have studied the scattering behavior from rough defects, as roughness may increase the measurement uncertainty and

possibly alter the inspection results [2, 38]. In order to understand the elastic wave scattering mechanisms for the above applications, different modelling methods can be applied.

Analytical formulae are capable of handling a variety of scattering problems within certain restricted ranges. Separation of variables (SEP) [39] provides exact mathematical formulae to calculate scattered waves but only from regular defects. The Geometrical theory of diffraction (GTD) can be applied for the diffraction problem with a flat crack [40]. The Kirchhoff approximation (KA) based on the assumption of an infinite tangential plane can calculate scattering signals from rough surfaces, but may result in unacceptable errors when the roughness is large or with grazing incidence/scattering angles [28].

Numerical approaches such as finite difference (FD) [41], finite element (FE) [13, 15] and boundary element (BE) methods [17, 42] can be implemented in situations where the approximation-based methods are not reliable, but with a downside in terms of computational cost. In [13], FE is considered to be more accurate and robust than FD given that the automatic meshing can exactly capture the shape of the defect. It may be argued that BE is a more efficient numerical method compared with FE, because it only needs to mesh the boundary of the scatterer. However, BE is not well suited for more complicated problems, such as scattering from inclusions or scattering in a heterogeneous material, while FE on the other hand can cover most elastic wave problems once the convergence is achieved. In addition there is a demand from the NDE industry for the use of qualified and standard FE packages. Commercial FE software such as Abaqus (Dassault Systemes Simulia Corp., Providence, RI) and Ansys (Ansys Inc., PA) have been widely applied in industry and are standard numerical tools. Also recently, researchers at Imperial College have developed a GPU based time-domain FE solver Pogo [43] to significantly accelerate FE simulations.

However, high computation cost is known as a big challenge for FE especially for unbounded domain problems. A powerful solution is to use a hybrid FE-BI method [20–22, 44, 45] to reduce the computation domain for the FE. Note that the FE-BI method is different from the FE-BE approach, for example, as used in earthquake

engineering [18, 46]. In these works, the FE and BE are formulated in sub-domains and are coupled to form a complete linear system of equations, which are solved to obtain the dynamic motion. In a different manner, the FE-BI approach first computes the local scattering in a small FE domain with the aid of the absorbing region [47–49], and then calculates the scattered waves via a boundary integral in a sequential order. Hence the complicated mathematical coupling between the FE and the BE is substantially simplified.

Depending on the application purposes, the FE-BI method in general can be implemented either in the frequency domain or in the time domain. The frequency domain method has been extensively studied and implemented for acoustic wave scattering problems (see, for example, the book by Ihlenburg [44]), and somewhat less work has been done on elastic wave scattering in solids. An elastodynamic finite element local scattering model has been developed to compute the scattering matrix, particularly on the array application in the far field [20, 21]. However, much less work has been done on the time-domain coupled FE-BI. A time-domain solution provides simulated waveforms convenient for data processing in many applications, such as ultrasonic imaging [38] and seismic full wave form inversion [50]. Using frequency domain algorithms the waveforms can also be simulated, but a number of FE simulations need to be run to obtain sufficient frequency components to recover the scattering signal.

A hybrid platform [45] has been implemented to compute the transient scattering signal using Auld's reciprocity principle. However, it needs a specific code to program since the FE calculation is based on a fictitious domain method with a family of mixed finite elements [49]. Recently, a generic hybrid method has been developed with implementation for standard commercial FE explicit solvers [22] . This approach provides an analytical hybrid scheme to link transducer and defect responses computed from a numerical method.

The standard hybrid idea for the use of NDE as described in [22] is shown in Fig. 3.1. The three basic steps of the hybrid method are introduced: In the first step, the transducer response is calculated using the time-domain FE solver inside the source box, and the radiating waves from the transducer are collected by a monitoring box.

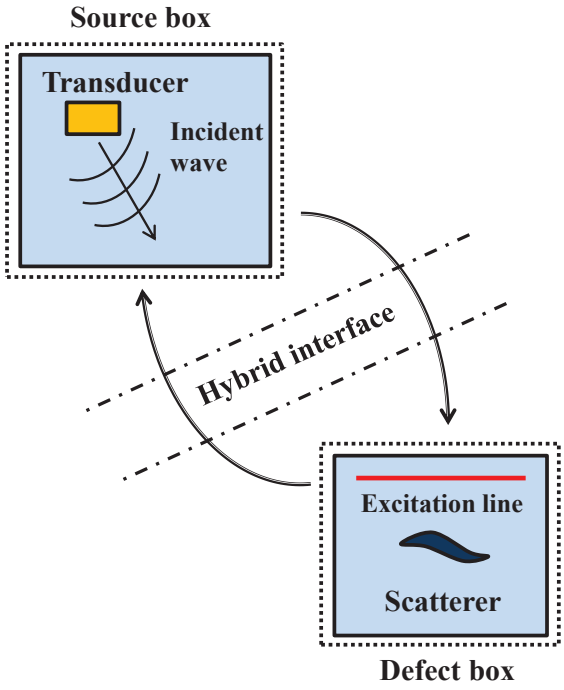

Figure 3.1: Illustration of the prototypical hybrid concept.

A hybrid scheme based on the wave potential is applied to calculate the incident wave propagating to the defect box. In the second step, the interaction between the incident wave and the scatterer is computed again by the time-domain FE inside the defect box. The excitation of the FE model is realized by applying forces to an excitation line (2D) or an excitation plane (3D) several elements away from the defect. In the third step, the scattering field is collected by a monitoring box around the scatterer, and the hybrid scheme is used to calculate the receiving signals at the transducer.

A more robust and efficient time-domain approach will be shown in the next section, which is an extension of the previous hybrid method in the following aspects. First of all, the excitation and the monitoring nodes for the FE model can be on the scatterer surface. Hence the size of the FE model can be further reduced, and the computational effort for the boundary integral is also minimized. Secondly, the boundary integral is formulated with displacement and traction instead of the wave potential used in the previous hybrid method, and it will be shown to be accurate in both near and far fields. In addition, the boundary integral is represented as a superposition of retarded time traces to avoid the loop using FFT and IFFT. Finally,

the new approach is flexible to model more complex inspection scenarios, including scattering from rough surfaces in a half space, and from scatterers with different boundary conditions.

3.2 Methodology

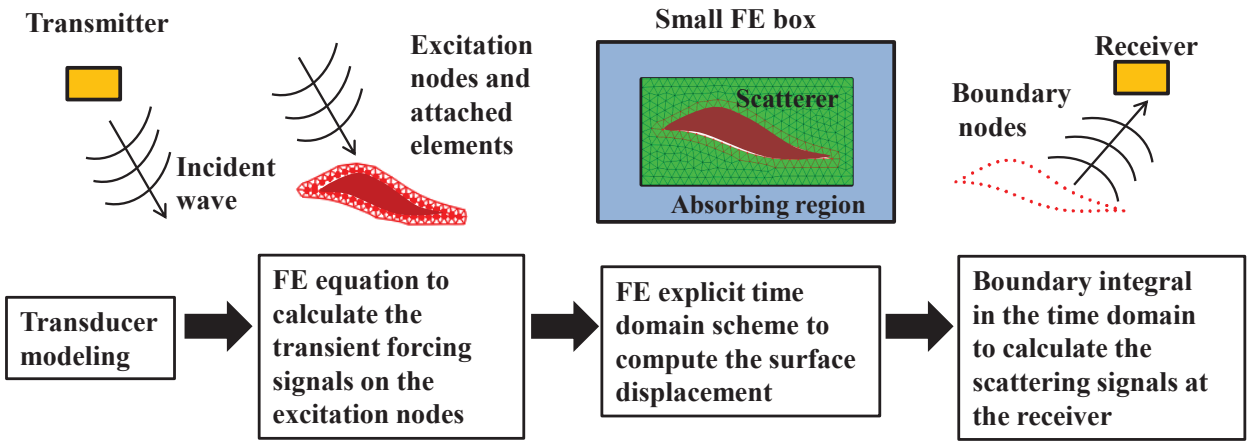

Figure 3.2: A flow chart of the proposed method.

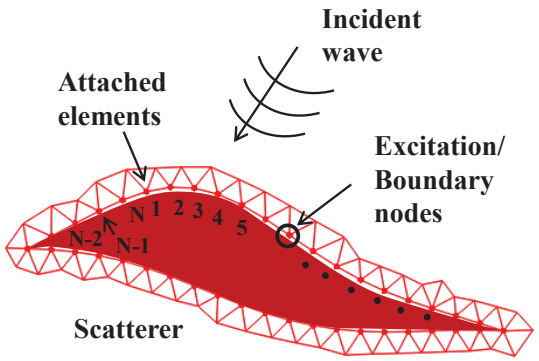

Figure 3.3: Excitation nodes and attached elements on a scatterer.

Following the basic steps of the hybrid concept described in Fig. 3.1, the new modelling procedure in this chapter can be shown in Fig. 3.2 as a flow chart. In the first step, the transducer is modelled to obtain the incident wave displacement field, for example using the Rayleigh integral [51]. A FE formulation is then used to calculate

the required forcing signals applied on the excitation nodes, which can be located at the scatterer surface. Only elements attached at the excitation nodes are required for the FE equation. By using the forces obtained from the previous step as an input, the standard 2nd-order FE explicit scheme is implemented to compute the scattering displacement inside a small box. An absorbing region with a thickness of around one wavelength is added to eliminate unwanted reflections from the boundary. In the last step, the displacement signals on the scatterer surface are recorded, and substituted into the boundary integral to calculate the scattering signals at the receiver.

3.3 Time-domain finite element calculations

3.3.1 Finite element formulation

The 2nd-order elastodynamic FE equation within one element is [14]:

$$\mathbf{M}^e\ddot{\mathbf{u}}^e + \mathbf{C}^e\dot{\mathbf{u}}^e + \mathbf{K}^e\mathbf{u}^e = \mathbf{bc}^e + \mathbf{f}^e \tag{3.1}$$

Where $\mathbf{u}^e$ is the displacement vector, $\mathbf{M}^e$ is the mass matrix, $\mathbf{K}^e$ is the stiffness matrix and $\mathbf{C}^e$ is the damping matrix. $\mathbf{bc}^e$ is the nodal force caused by the boundary traction and $\mathbf{f}^e$ is the nodal force caused by the applied body force.

In NDE, the scatterer is normally a crack with a stress-free boundary condition, and hence the boundary term $\mathbf{bc}$ is zero. By adapting Eq. (3.1) and assembling the required matrices, the following two equations can be obtained:

$$\mathbf{f}_{att}(t) = \mathbf{M}_{att}\ddot{\mathbf{u}}_{in}(t) + \mathbf{K}_{att}\mathbf{u}_{in}(t) \tag{3.2}$$

$$\mathbf{M}_{all}\ddot{\mathbf{u}}(t) + \mathbf{C}_{all}\dot{\mathbf{u}}(t) + \mathbf{K}_{all}\mathbf{u}(t) = \mathbf{f}_{ex}(t) \tag{3.3}$$

In Eq. (3.2), $\mathbf{M}_{att}$ and $\mathbf{K}_{att}$ are the local mass and stiffness matrices assembled only from elements attached at the excitation nodes as shown in Fig. 3.3. $\mathbf{M}_{all}$, $\mathbf{K}_{all}$ and $\mathbf{C}_{all}$ are corresponding matrices for the whole FE box, including the absorbing region. $\mathbf{f}_{att}(t)$ are forces at all nodes associated with the elements attached at the boundary of the defect, and $\mathbf{f}_{ex}(t)$ are forces at excitation/boundary nodes.

By substituting the incident displacement $\mathbf{u}_{in}(t)$ at the nodes of the attached elements into Eq. (3.2), one can calculate the forces at the nodes of the attached elements $\mathbf{f}_{att}(t)$ using the central difference in the time domain:

$$\mathbf{f}_{att}(t) = \mathbf{M}_{att}\frac{\mathbf{u}_{in}(t+\delta t) - 2\mathbf{u}_{in}(t) + \mathbf{u}_{in}(t-\delta t)}{\delta t^2} + \mathbf{K}_{att}\mathbf{u}_{in}(t) \tag{3.4}$$

$\mathbf{u}_{in}(t-\delta t)$, $\mathbf{u}_{in}(t)$ and $\mathbf{u}_{in}(t+\delta t)$ are the incident wave displacement vectors at the previous, current and next time steps, respectively. The values of the stiffness and mass matrices can be easily obtained from commercial FE software packages, such as Abaqus and Pogo. Hence it is straightforward to program Eq. (3.4) and calculate $\mathbf{f}_{att}(t)$ accroding to $\mathbf{u}_{in}(t)$. The excitation forces $\mathbf{f}_{ex}(t)$ at the nodes on the crack surface can then be extracted from $\mathbf{f}_{att}(t)$.

If the boundary condition is not stress-free, $\mathbf{f}_{ex}(t)$ needs to be subtracted by an additional boundary term $\mathbf{bc}_{ex}(t)$:

$$\mathbf{bc}_{ex}(t) = \int_{\Gamma} \mathbf{p}_{ex}(t)\mathbf{s}d\Gamma = \int_{\Gamma}[\ \mathbf{EBu}_{in}(t)\mathbf{n}\ ]\mathbf{s}d\Gamma \tag{3.5}$$

in which $\mathbf{B}$ is the strain-displacement matrix, $\mathbf{E}$ is the matrix containing the elastic constants [14], ,$\mathbf{n}$ is the normal vector at the boundary, $\mathbf{s}$ is the shape function and Γ is the boundary surface for integration.

In the second step, $\mathbf{f}_{ex}(t)$ obtained from Eq. (3.2) are taken into Eq. (3.3) as an input to calculate the displacement field $\mathbf{u}(t+\delta t)$ [43] in the local FE box:

$$\mathbf{u}(t+\delta t) = (\frac{\mathbf{M}_{all}}{\delta t^2}+\frac{\mathbf{C}_{all}}{2\delta t})^{(-1)}[\mathbf{f}_{ex}(t)+(\frac{\mathbf{C}_{all}}{2\delta t}-\frac{\mathbf{M}_{all}}{\delta t^2}\mathbf{u}(t-\delta t)+(\frac{2\mathbf{M}_{all}}{\delta t^2}-\mathbf{K}_{all})\mathbf{u}(t)] \tag{3.6}$$

This equation is a standard 2nd-order explicit scheme for elastic wave problems as implemented in available software packages. In this thesis, the explicit solver of Abaqus or Pogo is executed to perform Eq. (3.6). The acceptable thickness of the absorbing layers is approximately 1λ [48]. Assuming that the maximum dimension of the scatterer is L_s, then in general the maximum dimension of the FE box is just $L_s + 2\lambda$. Such a small computational region makes the implementation of FE in 3D possible. In summary, the FE equations are used twice with different formulations. Specifically, the force $\mathbf{f}_{ex}$ is first calculated according to the known incident wave

displacement using Eq. (3.2), and these forces are then used in Eq. (3.3) to compute the displacement field $\mathbf{u}$ at the surface of the scatterer.

3.3.2 Absorbing region

To model the wave propagation in an unbounded domain using a volume discretized method, it is necessary to truncate the domain and therefore some kind of non-reflecting exterior is needed to prevent artificial reflections from the outer boundary. The most widely used approach is to use an absorbing region, and probably the most efficient of these is the Perfect Matched Layer (PML), which requires only one thin layer to fool the solution into 'thinking' that it extends forever with no boundary. Many studies have implemented PML with acoustic and electromagnetic wave equations [44], and split/unsplit elastodynamic equations [52]. However, so far PML has not successfully been incorporated into the 2nd-order FE explicit scheme for elastic waves.

An alternative form of absorbing region that works with explicit time domain, is to introduce layers that have increasing damping values, in order to gradually attenuate the energy of the waves impinging into the layers. This idea (ALID) has been applied in [47] and the minimum thickness of the absorbing region is shown to be approximately 3λ. This technique is further improved by Pettit [48] to decrease the minimum thickness to around 1.5λ using a Stiffness Reduction Matrix (SRM) technique. The details of the SRM can be found in [48] and the basic mechanism is briefly given here.

In the frequency domain, by assuming a harmonic solution of Eq. (3.3) the 2nd-order FE equation can be written as:

$$-\mathbf{M}\omega^2\mathbf{u} - \mathbf{C}i\omega\mathbf{u} + \mathbf{K}\mathbf{u} = \mathbf{f} \tag{3.7}$$

where $\mathbf{C} = C_M\mathbf{M} + C_K\mathbf{K}$, decoupled into two components for the mass and the stiffness matrices. Substituting $\mathbf{C}$ into Eq. (3.7) leads to complex values of the

density ρ and the Young's modulus E:

$$\begin{aligned} \rho &\rightarrow \rho(1 + i\frac{C_M}{\omega}) \\ E &\rightarrow E(1 - i\omega C_K) \end{aligned} \tag{3.8}$$

Normally C_K is set to be zero to avoid an issue regarding the numerical stability [47]. Hence the complex wave number k in the absorbing region can be expressed as:

$$k(k_{real}, k_{imag}) \propto \sqrt{\frac{\rho(1 + \frac{iC_M}{\omega})}{E}} \tag{3.9}$$

The imaginary part of the wavenumber k plays a key role to decay the wave propagating inside the absorbing region. The basic idea of SRM is to gradually increase k_{imag}, by controlling the values of the damping term C_M and the Young's modulus E in the following manner:

$$\begin{aligned} C_M(x) &= C_{Mmax} X(x)^p \\ E(x) &= E_0 e^{-\alpha(x) k_{inc} x} \end{aligned} \tag{3.10}$$

Where the value of $\alpha(x)$ is defined as:

$$\alpha(x) = \alpha_{max} X(x)^p \tag{3.11}$$

Here C_{Mmax} and α_{max} are both positive values, and $X(x)$ ranges from zero at the starting layer to one at the end layer of the absorbing region, where x refers to the spatial coordinate corresponding to each absorbing layer. SRM is shown to be more efficient than ALID [48] and therefore is implemented in all simulations in this thesis.

3.3.3 Meshing algorithm

The accuracy and the efficiency of the FE computation depend on how the domain is meshed. For decades structured meshing using square (2D) or cubic (3D) elements is considered to be the best solution to model wave propagation, since it minimizes the scattering by the grid [16]. Also it is proved to be efficient when modelling simple scattering problems when the crack geometry is regular [16]. However, to model

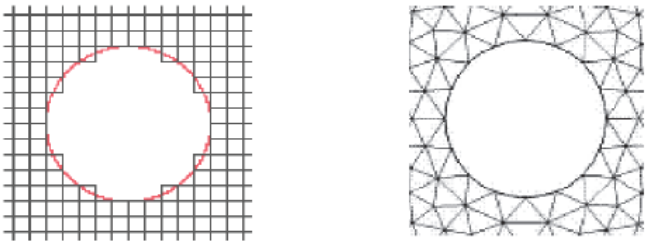

Figure 3.4: Comparison between the regular meshing and the free meshing algorithms (Pictures from [3]). (a) Regular mesh around a circular hole. (b) Free mesh around a circular hole.

defects with more complicated geometries the structured meshing will produce the 'staircase' profile as shown in Fig. (3.4)(a), which is only an approximation of the true shape. As the roughness of the defect becomes larger the distortion caused by the approximation becomes more severe. The results from such a meshing profile are unreliable unless a very small element size is used.

In contrast, automatic or free meshing algorithms using the triangular (2D) or tetrahedral (3D) element gives the possibility to accurately capture the shape of the irregular defect. The geometry of the corresponding element and the automatic meshing mechanism provide sufficient flexibility to model defects with arbitrary shapes, as shown in Fig. 3.4(b) compared with (a). For this reason the free meshing method has been widely applied to model the scattering from rough surfaces for different waves [7, 53]. However, free meshing tends to randomize the distribution and the shape of each element, and thus may introduce more severe mesh-scattering and dispersion [16]. In addition, unexpectedly distorted elements with very short lengths might appear. According to [16] the established convergence criteria require the element size to be smaller than the shortest wavelength divided by 20, and the time step to be smaller than the smallest element length divided by the wave speed. To ensure convergence and stability, a very short element length requires a small time step, which as a result would increase the computation time.

An alternative way is to combine the two meshing algorithms. Specifically, only the domain closely attached with the defect is free meshed and the remaining region

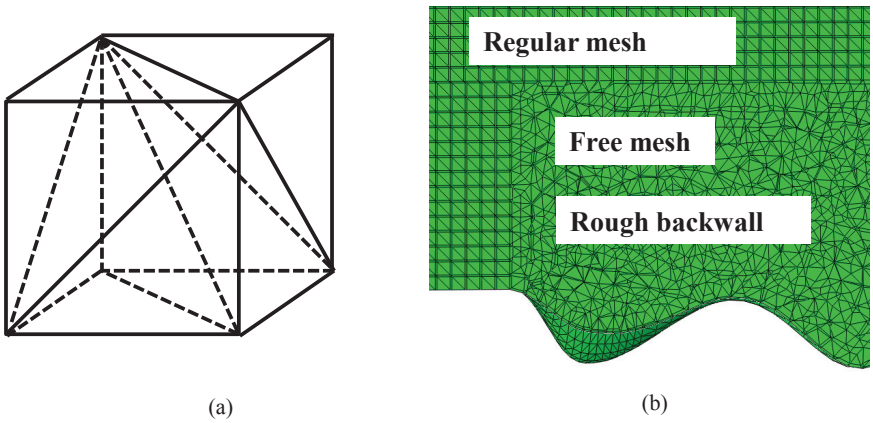

Figure 3.5: Mixed meshing profile in 3D. (a) One cubic cell composed of six tetrahedral elements. (b) Local view of the 3D mixed meshing of a rough surface.

is regularly meshed. To avoid the unwanted reflection from the interface, only one element type is used for the whole FE domain (e. g. triangular element in 2D and tetrahedral element in 3D). In 2D, the idea can be easily realized using the Abaqus build-in function to link the two meshing methods. However, such a function for 3D meshing does not exist in Abaqus. Hence the mixed meshing in 3D is programmed with a self-developed code using Matlab (Mathworks, Natick, MA, USA). Specifically, the very local free meshing profile is used as an input to the Matlab code, to regularly mesh the remaining region of the 3D model. The regular meshed region is filled with many hexahedral cells, and each cell is composed of six linear tetrahedral elements as shown in Fig. 3.5(a). Fig. 3.5(b) shows a local view of the mesh profile of one 3D FE model with a rough surface. It should be noted that at the interface between the free meshing and the regular meshing regions, the two neighboring elements need to have the same hypotenuse to prevent any spurious reflections. In this manner, the mesh minimizes the drawbacks caused by the free meshing algorithm while still capturing the exact shape of the complex rough defect.

The mixed meshing method can be very useful for the conventional hybrid method [22] using rectangular/cubic monitoring boxes, since it is much easier to accurately locate monitoring boxes from the regular grid, than from the randomly distributed nodes in a practical sense. Furthermore, the mixed meshing might be potentially applied for more sophisticated models, for instance the scattering from a rough

defect inside granular materials, and the scattering of guided waves from a rough corrosion on the pipe wall.

3.4 Boundary integral formulae

3.4.1 Time-domain representation

Once the surface displacements are computed by the FE model, they will be used in the boundary integral to calculate the scattered waves according to the Huygens' principle. Specifically, it will be useful to obtain simple expressions for the numerical implementation of the time-domain boundary integral. The general boundary integral formulae in the time domain can be found in the book by Achenbach [40]:

$$\begin{aligned} u_k^{sc}(\boldsymbol{R},t) &= \int_0^t \int_S [\sigma_{ij;k}^G(|\boldsymbol{R}-\boldsymbol{r}|,t-\tau)u_i(\boldsymbol{r},\tau)n_j(\boldsymbol{r}) \\ &- \sigma_{ij}(\boldsymbol{r},\tau)u_{i;k}^G(|\boldsymbol{R}-\boldsymbol{r}|,t-\tau)n_j(\boldsymbol{r})]dS(\boldsymbol{r})d\tau \end{aligned} \tag{3.12}$$

where $u_i(\boldsymbol{r},\tau)$ and $\sigma_{ij}(\boldsymbol{r},\tau)$ represent the displacement and stresses at a point $\boldsymbol{r}$ at a time τ on the surface of the defect. $\boldsymbol{R}$ is the vector indicating the position of the far field observation point, and n_j is the unit normal vector pointing outside the surface. $u_{i;k}^G(|\boldsymbol{R}-\boldsymbol{r}|,t-\tau)$ and $\sigma_{ij;k}^G(|\boldsymbol{R}-\boldsymbol{r}|,t-\tau)$ are the time dependent elastodynamic Green's functions in the unbounded domain. The vector notations related with the boundary integral are depicted in Fig. 3.6.

In order to avoid the numerical singularity caused by the derivative of a delta function inside $\sigma_{ij;k}(\boldsymbol{r},\tau)$ [18], one may first seek a solution in the frequency domain and then transform the expression back to the time domain. In the frequency domain, the general boundary integral is:

$$\begin{aligned} u_k^{sc}(\boldsymbol{R},\omega) &= \int_S [\sigma_{ij;k}^G(|\boldsymbol{R}-\boldsymbol{r}|,\omega)u_i(\boldsymbol{r},\omega)n_j(\boldsymbol{r}) \\ &- \sigma_{ij}(\boldsymbol{r},\omega)u_{i;k}^G(|\boldsymbol{R}-\boldsymbol{r}|,\omega)n_j(\boldsymbol{r})]dS(\boldsymbol{r}) \end{aligned} \tag{3.13}$$

Where the expressions of the Green's function $\sigma_{ij;k}^G(|\boldsymbol{R}-\boldsymbol{r}|,\omega)$ and $u_{i;k}^G(|\boldsymbol{R}-\boldsymbol{r}|,\omega)$ can be found in [40].

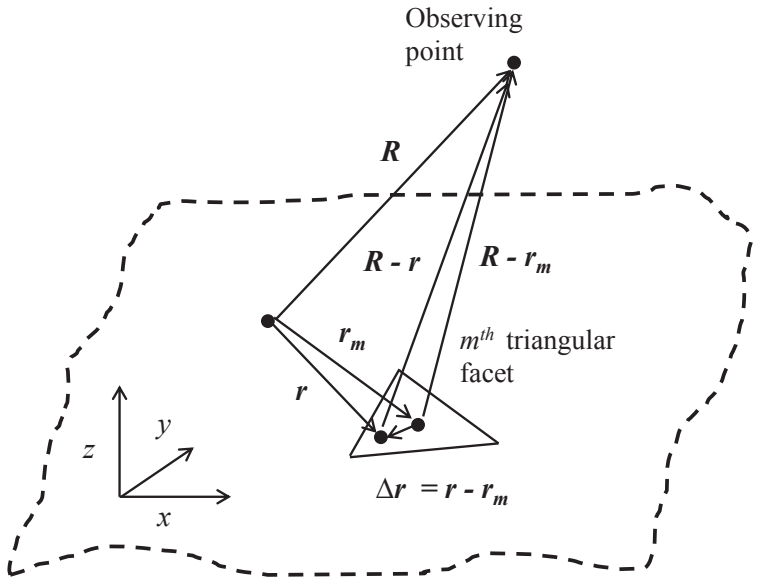

Figure 3.6: Notations of the vectors for the boundary integral. The triangular facet is part of the scatterer (defect); the observing point is the location where the scattering field is calculated.

To analytically manipulate the stress Green's function [2], the far field condition that $k_\alpha|\boldsymbol{R}-\boldsymbol{r}| \gg 1$ $(\alpha = p, s)$ is assumed, and terms involving $1/|\boldsymbol{R}-\boldsymbol{r}|^2$ are neglected. Hence Eq. (3.13) can be simplified as:

$$\begin{aligned} \boldsymbol{u}^{sc}(\boldsymbol{R},\omega) &= \sum_{\alpha=p,s} \frac{-1}{\rho c_\alpha^2} \int_S \frac{e^{(ik_\alpha D)}}{4\pi D} \boldsymbol{T}_\alpha(\boldsymbol{r},\hat{\boldsymbol{D}},\omega) dS(\boldsymbol{r}) \\ &- ik_\alpha \int_S \frac{e^{(ik_\alpha D)}}{4\pi D} \boldsymbol{U}_\alpha(\boldsymbol{r},\hat{\boldsymbol{D}},\omega) dS(\boldsymbol{r}) \end{aligned} \tag{3.14}$$

where

$$\begin{aligned} \boldsymbol{T}_p(\boldsymbol{r},\hat{\boldsymbol{D}},\omega) &= (\hat{\boldsymbol{D}}\cdot\boldsymbol{t})\hat{\boldsymbol{D}} \\ \boldsymbol{T}_s(\boldsymbol{r},\hat{\boldsymbol{D}},\omega) &= \boldsymbol{t} - (\hat{\boldsymbol{D}}\cdot\boldsymbol{t})\hat{\boldsymbol{D}} \\ \boldsymbol{U}_p(\boldsymbol{r},\hat{\boldsymbol{D}},\omega) &= [(\boldsymbol{u}\cdot\boldsymbol{n})(1-2\gamma^2) + 2\gamma^2(\boldsymbol{u}\cdot\hat{\boldsymbol{D}})(\boldsymbol{n}\cdot\hat{\boldsymbol{D}})]\hat{\boldsymbol{D}} \\ \boldsymbol{U}_s(\boldsymbol{r},\hat{\boldsymbol{D}},\omega) &= (\boldsymbol{n}\cdot\hat{\boldsymbol{D}})\boldsymbol{u} + (\boldsymbol{u}\cdot\hat{\boldsymbol{D}})\boldsymbol{n} - 2(\boldsymbol{u}\cdot\hat{\boldsymbol{D}})(\boldsymbol{n}\cdot\hat{\boldsymbol{D}})\hat{\boldsymbol{D}} \end{aligned} \tag{3.15}$$

and $\boldsymbol{D} = \boldsymbol{R} - \boldsymbol{r}$, representing the vector from one point on the crack surface to the far field observation point. $\hat{\boldsymbol{D}}$ denotes the unit vector of $\boldsymbol{D}$, and γ is the shear-to-compressional wave speed ratio (e. g. $\gamma = c_s/c_p$). $\boldsymbol{T}_p(\boldsymbol{r},\hat{\boldsymbol{D}},\omega)$ and $\boldsymbol{T}_s(\boldsymbol{r},\hat{\boldsymbol{D}},\omega)$ are decoupled compressional and shear components of the boundary traction. $\boldsymbol{U}_p(\boldsymbol{r},\hat{\boldsymbol{D}},\omega)$ and $\boldsymbol{U}_s(\boldsymbol{r},\hat{\boldsymbol{D}},\omega)$ are decoupled compressional and shear components of the bound-

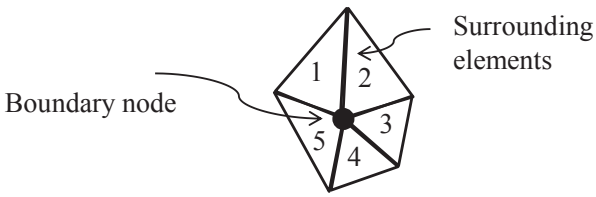

Figure 3.7: Recovery of the stress at the boundary node by averaging the stresses of surrounding elements.

ary displacement.

Taking the inverse Fourier transform of Eq. (3.14) , a boundary integral in the time domain can be expressed as:

$$\boldsymbol{u}^{sc}(\boldsymbol{R},t) = \sum_{\alpha=p,s} \frac{-1}{\rho c_\alpha^2} \int_S \frac{\boldsymbol{T}_\alpha(t-D/c_\alpha)}{4\pi D} dS(\boldsymbol{r}) + \frac{1}{c_\alpha} \int_S \frac{\boldsymbol{V}_\alpha(t-D/c_\alpha)}{4\pi D} dS(\boldsymbol{r}) \quad (3.16)$$

$\boldsymbol{T}_\alpha(t-D/c_\alpha)$ and $\boldsymbol{V}_\alpha(t-D/c_\alpha)$ represent travelling waves which are called surface retarded tractions and velocities, because these signals are delayed in the duration of time from one surface point of the crack towards the far field observing point.

In reality, the displacement $\boldsymbol{U}$ is the master variable which can be computed directly from the FE results as shown in Eq. (3.6). The velocity $\boldsymbol{V}(t-D/c_\alpha)$ is hence calculated as the derivative of $\boldsymbol{U}(t-D/c_\alpha)$. The traction $\boldsymbol{T}(t-D/c_\alpha)$ on the other hand needs to be estimated by the following steps:
(1) Locate the elements which share the same boundary node.
(2) Recover the stresses at the boundary elements using $\Sigma = \mathbf{EBu}(t)$.
(3) Take the average value of the recovered stresses of these elements to estimate the stress at the boundary node, and then calculate the corresponding traction.

Step (3) is critical when a linear triangular/tetrahedral element is implemented to mesh irregular geometries. This is because the stress value is a constant inside such an element, and the averaging procedure can improve the accuracy of the recovered stress at the node. The averaging process is illustrated in Fig. 3.7 for a typical

boundary node and the attached elements. The values of stresses from surrounding elements numbered 1 to 5 are used to calculate the mean value, as an approximation of the stress at the node itself.

The boundary of the defect can be discretized into small triangular facets in 3D as shown in Fig. 3.6 to perform the calculation numerically:

$$\begin{aligned} \boldsymbol{u}^{sc}(\boldsymbol{R},t) &= \sum_{\alpha=p,s}[\frac{-1}{\rho c_\alpha^2}\sum_{m=1}^{M}\frac{1}{4\pi D_m}\int_{S_m}\boldsymbol{T}_\alpha(t-D/c_\alpha)dS_m(\boldsymbol{r}) \\ &+ \frac{1}{c_\alpha}\sum_{m=1}^{M}\frac{1}{4\pi D_m}\int_{S_m}\boldsymbol{V}_\alpha(t-D/c_\alpha)dS_m(\boldsymbol{r})] \end{aligned} \tag{3.17}$$

Where $D_m = R$ - r_m, and r_m is the centre of the mth facet.
Since $|\boldsymbol{R}| \gg |\Delta\boldsymbol{r}|$, the vector between the observing point and the point at the crack surface can be approximated as:

$$D = |\boldsymbol{R}-\boldsymbol{r}| = |\boldsymbol{R}-\boldsymbol{r}_m-\Delta\boldsymbol{r}| \approx |\boldsymbol{R}-\boldsymbol{r}_m| - \frac{\Delta\boldsymbol{r}\cdot(\boldsymbol{R}-\boldsymbol{r}_m)}{|\boldsymbol{R}-\boldsymbol{r}_m|} = D_m - \Delta\boldsymbol{r}\cdot\hat{\boldsymbol{D}}_m \tag{3.18}$$

Note that Eq. (3.18) is not expanded in the usual way as a first order far field approximation (e. g. $D \approx R - \hat{\boldsymbol{R}}\cdot\boldsymbol{r}$), Hence the conventional restriction that the integration is accurate only beyond the far field distance can be much more relaxed. More details are discussed in the next section showing that the boundary integral is accurate as long as the distance is larger than around 2 wavelength, which is well within the near field.

Next a general form $\boldsymbol{F}(t-D/c_\alpha)$ is used to represent either $\boldsymbol{T}(t-D/c_\alpha)$ or $\boldsymbol{V}(t-D/c_\alpha)$. By replacing D with the approximation from Eq. (3.18) , $\boldsymbol{F}(t-D/c_\alpha)$ can be expanded using a Taylor series:

$$\boldsymbol{F}(t-D/c_\alpha) \approx \boldsymbol{F}(t-D_m/c_\alpha) + \frac{\Delta\boldsymbol{r}\cdot\hat{\boldsymbol{D}}_m}{c_\alpha}\boldsymbol{F}'(t-D_m/c_\alpha) + O(\Delta\boldsymbol{r}^2) \tag{3.19}$$

The integration of $\boldsymbol{F}(t - D/c_\alpha)$ across one facet is therefore:

$$\begin{aligned}\int_{S_m} \boldsymbol{F}(t - D/c_\alpha) dS_m(\boldsymbol{r}) &\approx \int_{S_m} \boldsymbol{F}(t - D_m/c_\alpha) dS_m(\boldsymbol{r}) \\ &+ \int_{S_m} \frac{\Delta \boldsymbol{r} \cdot \hat{\boldsymbol{D}}_m}{c_\alpha} \boldsymbol{F}'(t - D_m/c_\alpha) dS_m(\boldsymbol{r}) \\ &\approx I_m \boldsymbol{F}(t - D_m/c_\alpha) \\ &+ \boldsymbol{F}'(t - D_m/c_\alpha) \int_{S_m} \frac{\Delta \boldsymbol{r} \cdot \hat{\boldsymbol{D}}_m}{c_\alpha} dS_m(\boldsymbol{r})\end{aligned} \tag{3.20}$$

where I_m refers to the area of the mth facet.

Apparently in Eq. (3.20) the first term assumes that the boundary values are constant across this facet, which can be approximated as that from the centre point. Since in the numerical implementation the scattered wave at the centre is calculated as an average of those at the facet nodes, this first term is equivalent to applying a trapezoidal rule to the integration. Higher order Taylor expansion terms which refer to the derivatives of the retarded time traces account for the time variation across the facet. However, it will be shown through several numerical examples that the integration simply keeping the first term is sufficiently accurate with the mesh density that has been tested.

In 2D the boundary integration formula has a different form from that of 3D and a scaling factor ($\sqrt{\frac{2i\pi}{k_\alpha}}$) needs to be multiplied in the frequency domain:

$$\begin{aligned}\boldsymbol{u}^{sc}(\boldsymbol{R}, \omega) &= \sum_{\alpha=p,s} \sqrt{\frac{2i\pi}{k_\alpha}} [\frac{-1}{\rho c_\alpha^2} \int_S \frac{e^{(ik_\alpha D)}}{4\pi\sqrt{D}} \boldsymbol{T}_\alpha(\boldsymbol{r}, \hat{\boldsymbol{D}}, \omega) dS(\boldsymbol{r}) \\ &- ik_\alpha \int_S \frac{e^{(ik_\alpha D)}}{4\pi\sqrt{D}} \boldsymbol{U}_\alpha(\boldsymbol{r}, \hat{\boldsymbol{D}}, \omega) dS(\boldsymbol{r})]\end{aligned} \tag{3.21}$$

Transforming the above equation to the time domain yields a convolution between the scaling factor and the boundary formula after the inverse FFT.

3.4.2 Integration in the frequency domain

As shown in Eq. (3.20), in the time domain the integration at one facet can only be calculated numerically. In contrast, an exact expression of the integral can be

obtained in the frequency domain [54]. By discretizing the surface, Eq. (3.14) can be expressed as:

$$\begin{aligned} \boldsymbol{u}^{sc}(\boldsymbol{R}) &= \sum_{\alpha=p,s} \frac{-1}{\rho c_\alpha^2} \sum_{m=1}^{M} \int_{S_m} \frac{e^{ik_\alpha D}}{4\pi D} \boldsymbol{T}_\alpha(\boldsymbol{r}, \boldsymbol{D}, \omega) dS_m(\boldsymbol{r}) \\ &- ik_\alpha \sum_{m=1}^{M} \int_{S_m} \frac{e^{ik_\alpha D}}{4\pi D} \boldsymbol{U}_\alpha(\boldsymbol{r}, \boldsymbol{D}, \omega) dS_m(\boldsymbol{r}) \end{aligned} \tag{3.22}$$

Using the approximation in Eq. (3.18), the boundary integral can be written as:

$$\begin{aligned} \boldsymbol{u}^{sc}(\boldsymbol{R}) &= \sum_{\alpha=p,s} \frac{-1}{\rho c_\alpha^2} \sum_{m=1}^{M} \frac{e^{ik_\alpha D_m}}{4\pi D_m} \boldsymbol{T}_\alpha(\boldsymbol{r}_m, \boldsymbol{D}_m) \int_{S_m} e^{-ik_\alpha \hat{\boldsymbol{D}}_m \cdot \boldsymbol{\Delta r}} dS_m(\boldsymbol{\Delta r}) \\ &- ik_\alpha \sum_{m=1}^{M} \frac{e^{ik_\alpha D_m}}{4\pi D_m} \boldsymbol{U}_\alpha(\boldsymbol{r}_m, \boldsymbol{D}_m) \int_{S_m} e^{-ik_\alpha \hat{\boldsymbol{D}}_m \cdot \boldsymbol{\Delta r}} dS_m(\boldsymbol{\Delta r}) \end{aligned} \tag{3.23}$$

The integral of the exponential term in Eq. (3.23) represents the phase variation, which can be expressed analytically for a triangular facet:

$$\begin{aligned} \int_{S_m} e^{-ik_\alpha \hat{D}_m \cdot \boldsymbol{\Delta r}} dS_m(\boldsymbol{\Delta r}) &= \frac{1}{(\hat{\boldsymbol{n}} \cdot \hat{\boldsymbol{z}})} \frac{-1}{ik_\alpha(\hat{D}_{my} + B\hat{D}_{mz})} \\ &\times [l_x \mathrm{sinc}[k_\alpha(\hat{D}_{mx} - \hat{D}_{my} + (A-B)\hat{D}_{mz}) \frac{l_x}{2}] \\ &- e^{ik_\alpha(\hat{D}_{my} + B\hat{D}_{mz}) \frac{l_y}{2}} l_y \mathrm{sinc}[k_\alpha(\hat{D}_{mx} + A\hat{D}_{mz}) \frac{l_x}{2}]] \end{aligned} \tag{3.24}$$

Where $\hat{\boldsymbol{n}}$ is the normal vector of the mth facet, $\hat{\boldsymbol{z}}$ is the unit vector of the z-axis, and $A = \frac{\partial z}{\partial x}$, $B = \frac{\partial z}{\partial y}$, are the Cartesian coordinates of the gradient of the triangular facet at its midpoint. The dimensions of the trian gular facet in the x- and y- directions are l_x and l_y, respectively.

In 2D, a similar equation can be obtained by multiplying a scaling factor before Eq. (3.23) , and replacing the spatial decay D_m by $\sqrt{D_m}$:

$$\begin{aligned} \boldsymbol{u}^{sc}(\boldsymbol{R}) &= \sqrt{\frac{2i\pi}{k_\alpha}} [\sum_{\alpha=p,s} \frac{-1}{\rho c_\alpha^2} \sum_{m=1}^{M} \frac{e^{ik_\alpha D_m}}{4\pi\sqrt{D_m}} \boldsymbol{T}_\alpha(\boldsymbol{r}_m, \boldsymbol{D}_m) \int_{S_m} e^{-ik_\alpha \hat{\boldsymbol{D}}_m \cdot \boldsymbol{\Delta r}} dS_m(\boldsymbol{\Delta r}) \\ &- ik_\alpha \sum_{m=1}^{M} \frac{e^{ik_\alpha D_m}}{4\pi\sqrt{D_m}} \boldsymbol{U}_\alpha(\boldsymbol{r}_m, \boldsymbol{D}_m) \int_{S_m} e^{-ik_\alpha \hat{\boldsymbol{D}}_m \cdot \boldsymbol{\Delta r}} dS_m(\boldsymbol{\Delta r})] \end{aligned} \tag{3.25}$$

where the integral of the phase term can be expressed explicitly as:

$$\int_{S_m} e^{-ik_\alpha \hat{\boldsymbol{D}}_{\boldsymbol{m}}\cdot\boldsymbol{\Delta r}} dS_m(\boldsymbol{r}) = \sqrt{1+(\frac{\partial z}{\partial x})^2}\, l_x \mathrm{sinc}\left[\frac{(k_\alpha \hat{D}_{mx} + k_\alpha \hat{D}_{mz}\frac{\partial z}{\partial x})l_x}{2}\right] \tag{3.26}$$

By using Eq. (3.23) to Eq. (3.26) , in conjunction with the FFT and its inverse, the scattering signals can be obtained.

3.5 Performance in the near field

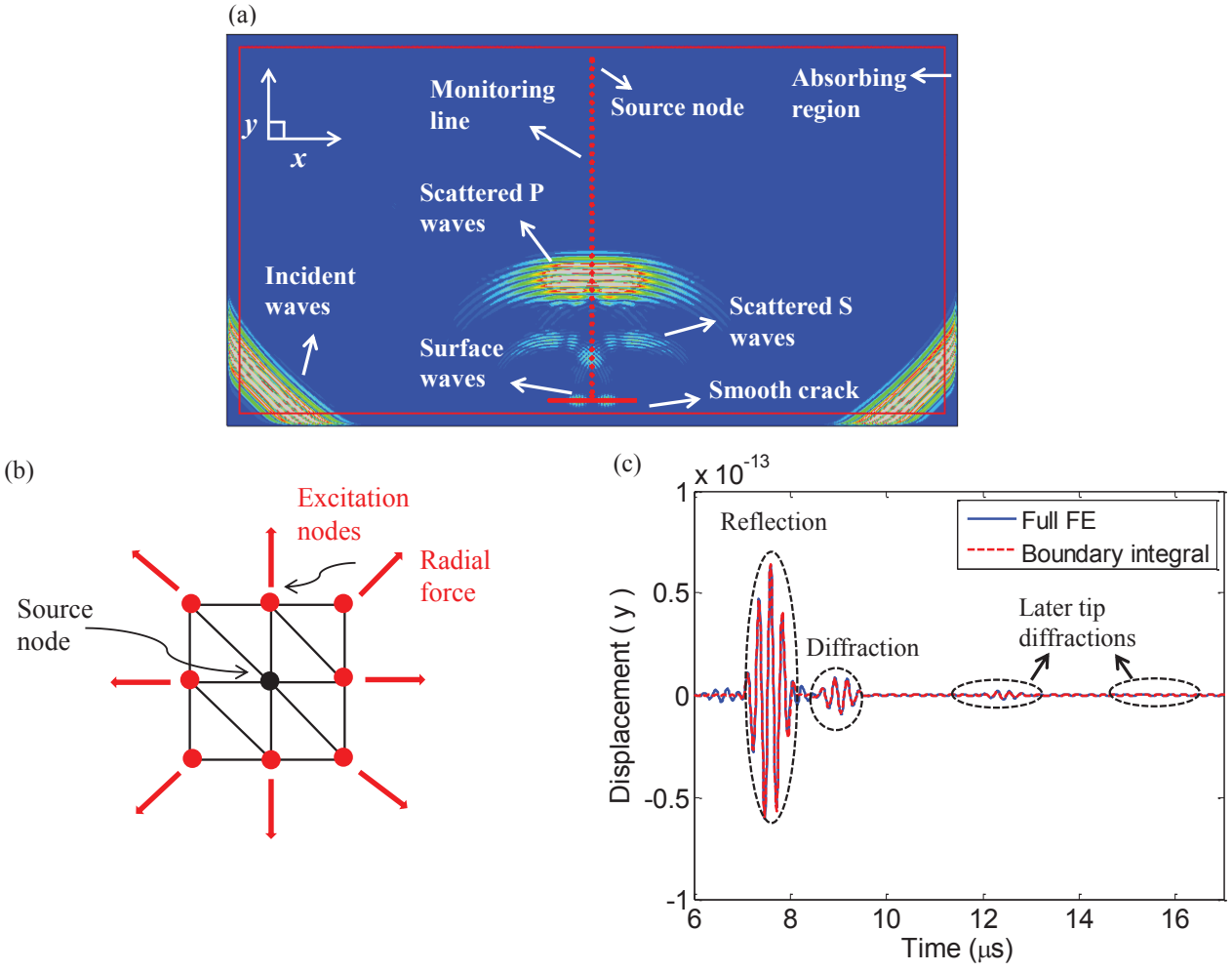

Figure 3.8: Comparison of the near to far field scattering for a smooth crack using the full FE model and the boundary integral method. (a) Snapshot of the animation for the FE model. (b) Illustration of forcing eight nodes to produce a circular wave in 2D. (c) Comparison of the scattering signal (u_y) at the monitoring node 3mm away from the crack using the FE model and the boundary integral.

A far field assumption is applied to simplify the stress Green's function as shown in

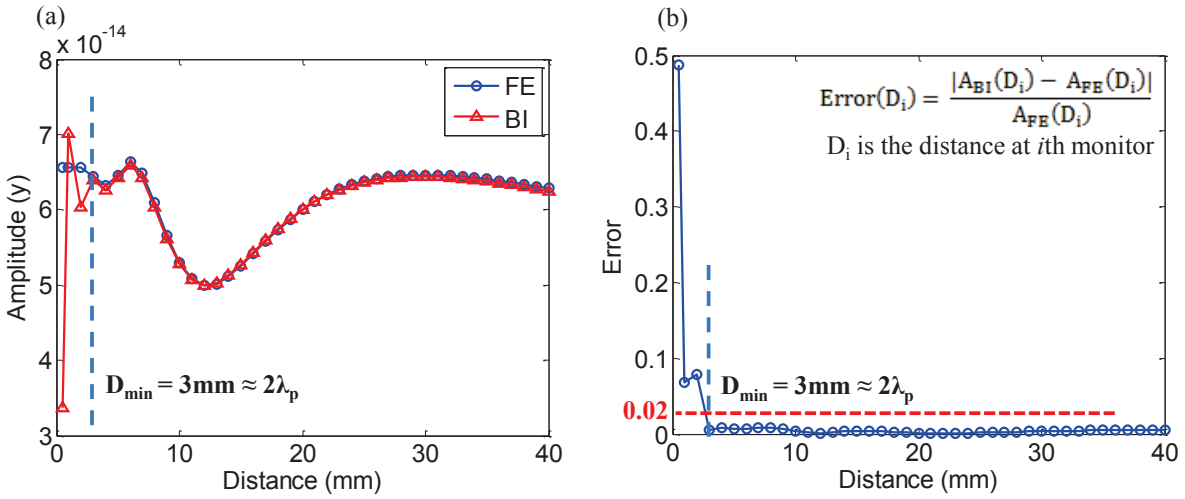

Figure 3.9: Comparison of the near to far field scattering amplitude (u_y) for a smooth crack using the full FE model and the boundary integral. (a)Scattering amplitude (peak of the envelope) as a function of the distance . (b) Relative error of the amplitude between the boundary integral and the full FE model.

Eq. (3.14) for the boundary integral. Therefore a minimum distance from the centre of the scatterer to the observing point exists, below which the boundary integral is not accurate. On the other hand, the term $|\boldsymbol{R}-\boldsymbol{r}|$ is approximated using Eq. (3.18), by assuming that $|\boldsymbol{R}| \gg |\Delta\boldsymbol{r}|$, instead of the conventional 1st-order expansion $D = |\boldsymbol{R}-\boldsymbol{r}| \approx R - \hat{\boldsymbol{R}}\cdot\boldsymbol{r}$ with the assumption that $|\boldsymbol{R}| \gg |\boldsymbol{r}|$. Since $|\boldsymbol{r}| \gg |\boldsymbol{\Delta r}|$, it is expected that the proposed boundary integral should be much more accurate than that using the conventional 1st-order expansion in the near field.

To find the minimum distance D_{min}, the scattering of an incident P wave from a smooth crack is modelled using the FE model as shown in Fig. 3.8(a). The FE model has a dimension of 86×46mm^2, including the absorbing region with a thickness of 1.5mm. Aluminium (Young's modulus, 70GPa; density, 2700kg/m^3; and Poisson ratio, 0.33) is chosen as the material for the 2D plane-strain model. The mixed meshing algorithm introduced in Section 3.3.3 is applied to mesh the whole FE domain with triangular elements (CPE3 in Abaqus). A point source is modelled by selecting neighboring eight nodes, excited with radial forces [16] as shown in Fig. 3.8(b). A five-cycle tone burst with a centre frequency of 4MHz is fed into each excitation node to produce the incident P wave. The length of the crack is 10mm ($\approx 6.5\lambda_p$), and the monitoring points are located from 0.5mm to 40mm to record the scattered P and S waves. The boundary displacements of the crack are also

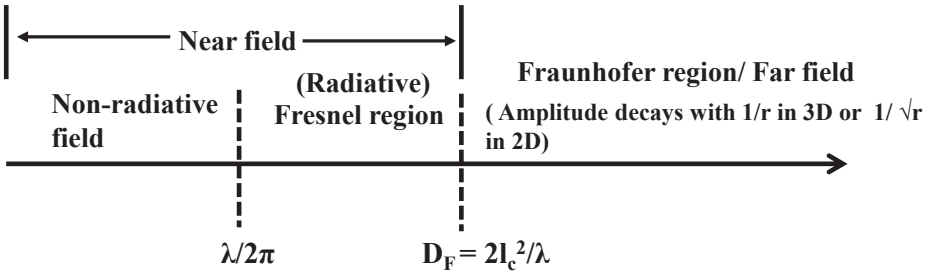

Figure 3.10: Categorization of the near and far field and the boundary between the two.

recorded, which are used for the boundary integral in Eq. (3.16) to calculate the scattered waves at those monitoring nodes. In order to obtain the purely scattered waves, an additional model without the crack is run and the monitored incident waves are subtracted from the total field. A comparison is then made between the results from the full FE model and those computed from the boundary integral.

Fig. 3.8(c) shows the scattering signals from FE and the boundary integral when the distance D equals to 3mm, which is around $2\lambda_p$. A good match of the waveforms can be found between the FE and the boundary integral, including different wave packets. The first arrival with the largest amplitude is the direct reflection from the crack, superposed by both P and S waves. One main later arrival around 8.3μs can be seen which are contributed from the tip diffraction. Some small later arrivals are due to the tip diffractions converted from the surface waves travelling and bouncing between the two tips.

The peaks of the recorded signal envelopes at all monitoring nodes are plotted as a function of the distance D in Fig. 3.9(a). The relative error between the FE and the boundary integral is also shown in Fig. 3.9(b). A very good agreement is seen when $D \geq 3\text{mm}$ ($\approx 2\lambda_p$), by setting the tolerance of the error to be 2%. Therefore for the crack length ($6.5\lambda_p$) tested here, the critical near field distance D_{min} for the boundary integral is approximately $2\lambda_p$. The value of D_{min} may vary according to the length of the crack, but well within the Fresnel region, or the near field.

The boundary between the near and the far field is vague, as there are no precise cutoffs between the two. However, according to the Fraunhofer and the Fresnel

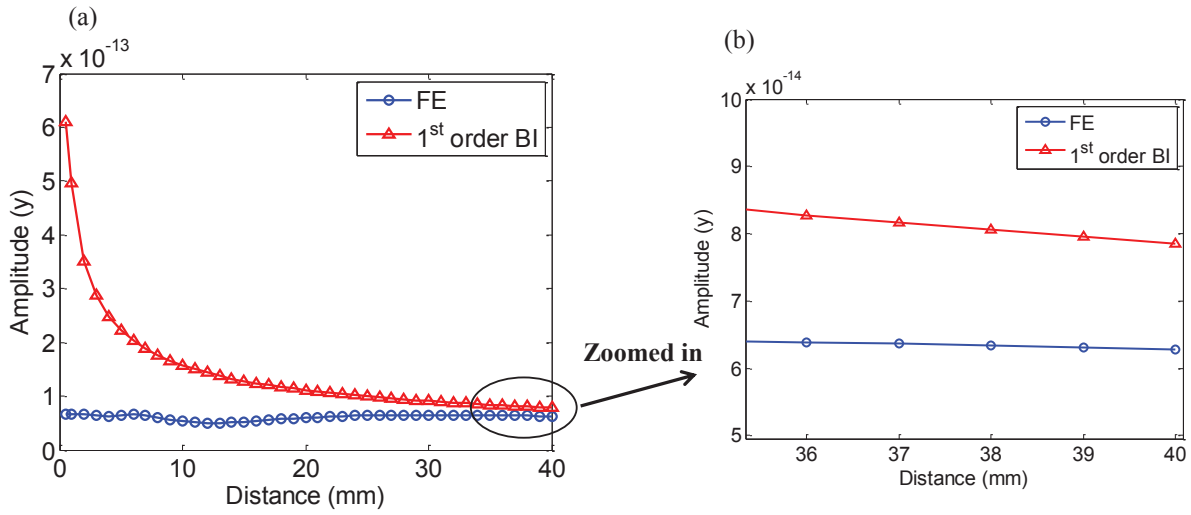

Figure 3.11: Comparison of the scattering amplitude (u_y) for a smooth crack using the full FE model and the boundary integral with the first order far field expansion. (a)Scattering amplitude (peak of the envelope) as a function of the distance . (b) Zoomed in plot of (a)

diffraction, an approximate rule can be used shown in Fig. 3.10 from the theory of antenna [55]. The critical distance to separate the near and the far field is defined as:

$$D_F = 2l_c^2/\lambda \tag{3.27}$$

Where l_c is the length of the crack, and λ is the wavelength. Eq. (3.27) is considered as a very stringent rule to guarantee the far field. However, in practice the rule can be somewhat relaxed depending on the source field, the geometry of the crack and the requirement of the accuracy. Inside the near field region, the radiative near-field is called the Fresnel region, while the other is the non-radiative region. The boundary between the radiative and the non-radiative field is set to be roughly $\lambda/2\pi$ from the crack surface. Note that the categorization in Fig. 3.8 is based on the assumption that the defect size is larger than the wavelength (for example, $l_c \approx 6.5\lambda_p$ in this case). For very short defects ($l_c \leq \lambda_p/2$) or defects of the same length with the wavelength, the actual expression for D_F may vary [55]. From Fig. 3.9 it is found that the boundary integral is accurate to cover most of the Fresnel region, apart from the far field.

In order to illustrate the advantage of the boundary integral over the conventional

approach, Fig. 3.11 shows the peaks of the scattering signals calculated when the distance D is expanded as $R - \hat{\boldsymbol{R}} \cdot \boldsymbol{r}$. As can be seen, the corresponding curve decays inversely proportional to the $\sqrt{r}$ in 2D, but it does not match the result from the FE model. The two curves converge quickly as the distance increases, although there is still a large error around 20% when the distance is 40mm, as shown in the zoomed-in plot in Fig. 3.11(b).

3.6 Numerical examples

In this section, four numerical examples are shown using the FE-BI method described in the preceding section and summarized in Fig. 3.2. A five-cycle tone burst with a centre frequency of 4MHz is used as the incident P wave, which is assumed to be a plane wave or a Gaussian tapered plane wave in the following simulations. Note that the proposed method can also model the scattering with a more general incident wave field produced from a real transducer.

3.6.1 Side Drilled Hole (SDH)

In 2D the plane wave scattering from a side-drilled hole (SDH) with a diameter of 4mm ($\approx 2.6\lambda_p$) is simulated, as shown in Fig. 3.12(a) for a full FE model. The corresponding full FE region has a dimension of 51×51mm^2 ($\approx 33\lambda_p \times 33\lambda_p$). The SRM absorbing region is adopted here and the thickness of the absorbing region is about 1.5mm ($\approx 1\lambda_p$). Linear triangular elements (equivalent to CPE3 in Abaqus) are applied to mesh the domain. The element size is $\lambda_p/60$, which is sufficient for the convergence of both scattered P and S waves [16]. An excitation line is placed 20mm ($\approx 13\lambda_p$) above the SDH to produce a plane P wave propagating along the negative y-direction, and the scattering signals are recorded by a monitoring circle 20mm away from the SDH. The full FE model is solved using the Abaqus explicit solver.

In contrast, the size of the FE box (8×8mm$^2 \approx 5\lambda_p \times 5\lambda_p$) used in the FE-BI method is much smaller, by comparing Fig. 3.12(a) and (b), and the excitation nodes are located at the SDH surface in the FE box denoted by red dots. The forcing applied at the defect surface is obtained from Eq. (3.4). After running the FE explicit

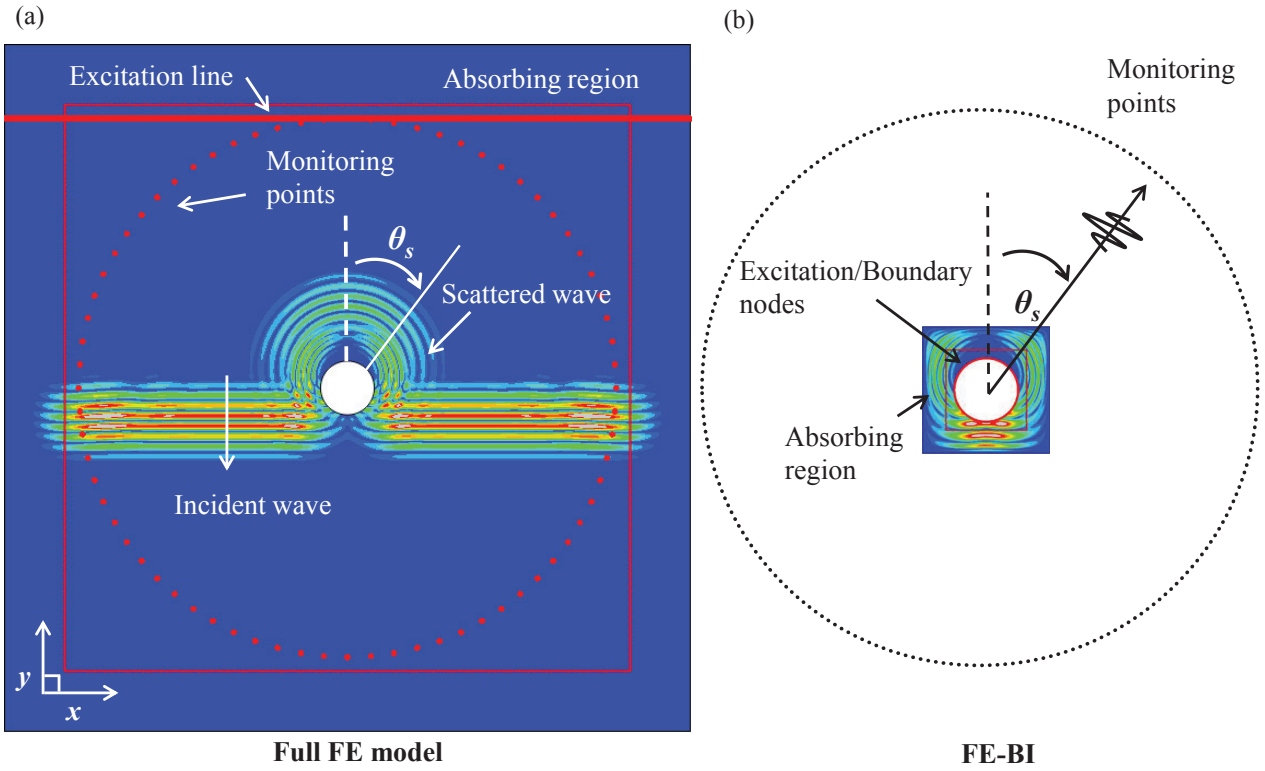

Figure 3.12: Snapshots of the plane wave scattering from a SDH. (a) Full FE model. (b) FE-BI box.

scheme in the box using Abaqus, the boundary displacements are used to calculate the scattering signals via the boundary integral Eq. (3.16), at the monitoring circle. Note that since the stress-free condition is applied here, the quantity of the boundary velocity in Eq. (3.16) must be the total field (i. e. incident field plus scattering field).

Good agreements of the results from the full FE model and the FE-BI method can be seen in Fig. 3.13(a) and (c), for the scattered P and S waves at a near grazing angle ($\theta_s = 80^o$). The scattering amplitude, which here is defined as the ratio of the peaks between the scattering and the incident signals, with θ_s ranging from 0 to 360 ^{o} is shown in Fig. 3.13(b) and (d), respectively. The mean absolute error (MAE) from all scattering angles is used to measure the numerical error and it can be expressed as:

$$\mathrm{MAE} = \frac{1}{\mathrm{M}} \sum_{\mathrm{n}=1}^{\mathrm{M}} |\mathrm{A}(\theta_{\mathrm{s}}^{\mathrm{n}}) - \mathrm{A}_{\mathrm{ref}}(\theta_{\mathrm{s}}^{\mathrm{n}})| / |\mathrm{A}_{\mathrm{ref}}(\theta_{\mathrm{s}}^{\mathrm{n}})| \tag{3.28}$$

Where M is the number of the scattering angles, $\mathrm{A}(\theta_s^n)$ and $\mathrm{A}_{ref}(\theta_s^n)$ are the scatter-

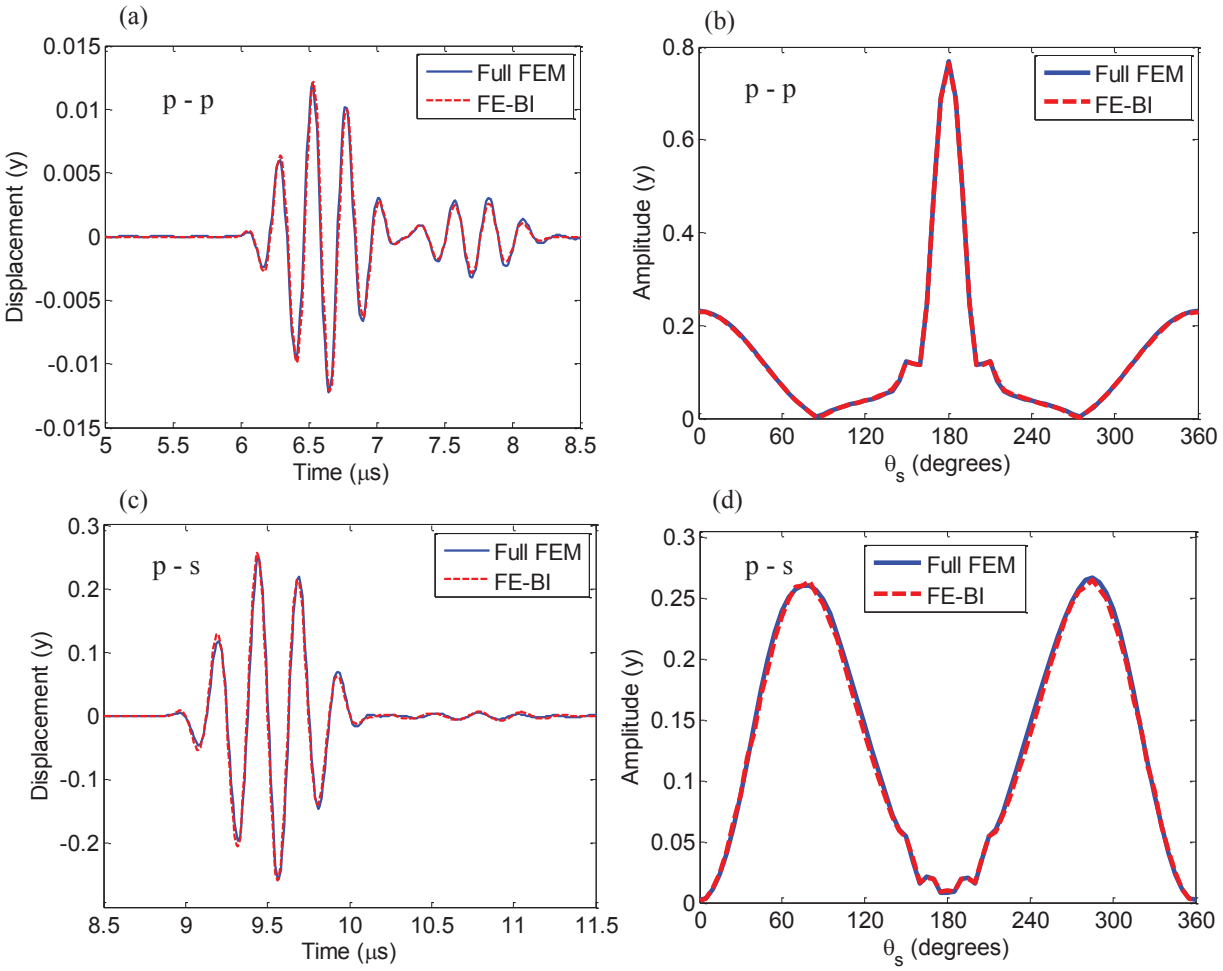

Figure 3.13: Comparison of the scattering signals (u_y) from a SDH using the full FE model and the FE-BI method. (a) Scattering P-P signals when $\theta_s = 80^o$. (b) P-P Scattering amplitude ($\theta_s = 0$ to 360^o). (c) Scattering P-S signals when $\theta_s = 80^o$. (d) P-S Scattering amplitude ($\theta_s = 0$ to 360^o).

ing amplitude calculated using the FE-BI method and the full FE model. For the SDH case, the MAE of the scattering coefficient between the FE box and the full FE model are calculated as 1.5% and 3.2% for P and S waves, respectively.

The element size used in the full FE model is $\lambda_p/60$, which is sufficiently small as it well satisfies the established convergence criteria [16]. On the contrary, in the FE-BI box the element size is $\lambda_p/30$, much larger than that used in the full FE simulation. It implies a somewhat more relaxed convergence requirement using the FE-BI method than the full FE model. The reason is that the local FE simulation mitigates the error caused by the mesh dispersion, when modelling the wave propagating from the source to the defect and vice versa. Giving the full FE model the same element size

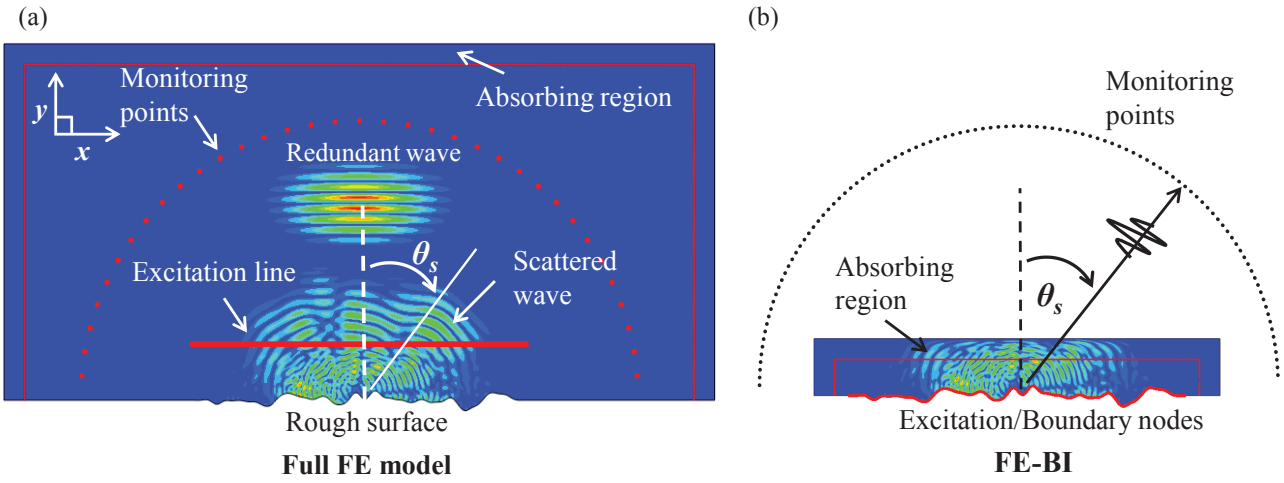

Figure 3.14: Snapshots of the scattered waves from a rough surface ($\sigma = \lambda_p/4$, $\lambda_0 = \lambda_p/2$). (a) Full FE model. (b) FE-BI box.

of $\lambda_p/30$ would cause noticeable errors for the scattered S waves due to the mesh dispersion. The number of nodes in the local FE box is around 25 thousand, which is significantly smaller than that for the full FE model (4.1 million), a reduction of approximately 170 times. In addition, the total time for running the full FE model is around 32 minutes, while for the small FE box it only takes 20 seconds. A huge improvement of the computational efficiency is therefore achieved.

3.6.2 Rough surface

The second example is the scattering of a plane P wave from a rough surface as shown in Fig. 3.14. To approximate the plane wave scattering from an infinitely long surface a Gaussian tapered plane wave as used in [56] is adopted here. A spatial Gaussian window is added to the ideal plane wave so that the amplitude of the incident wave impinging on the rough surface gradually reduces to zero at the ends, in order to avoid the edge effects when performing the boundary integral along the surface with a finite length. The total length of the surface is 24mm ($\approx 15\lambda_p$), based on which the half beam width is approximately 4mm ($\approx 2.6\lambda_p$). One realization of the Gaussian surface with RMS $= \lambda_p/4$ and correlation length $\lambda_0 = \lambda_p/2$ is generated using the spectral method [28]. The dimension of the full FE model shown in Fig. 3.14(a) is $51\times25.5\text{mm}^2$ ($\approx 33\lambda_p\times16\lambda_p$). An excitation line with the same length of the surface is placed 4mm ($\approx 2.6\lambda_p$) above the rough surface. The scattered waves are recorded by a semi-circle of the nodes 20mm away from the centre of the surface.

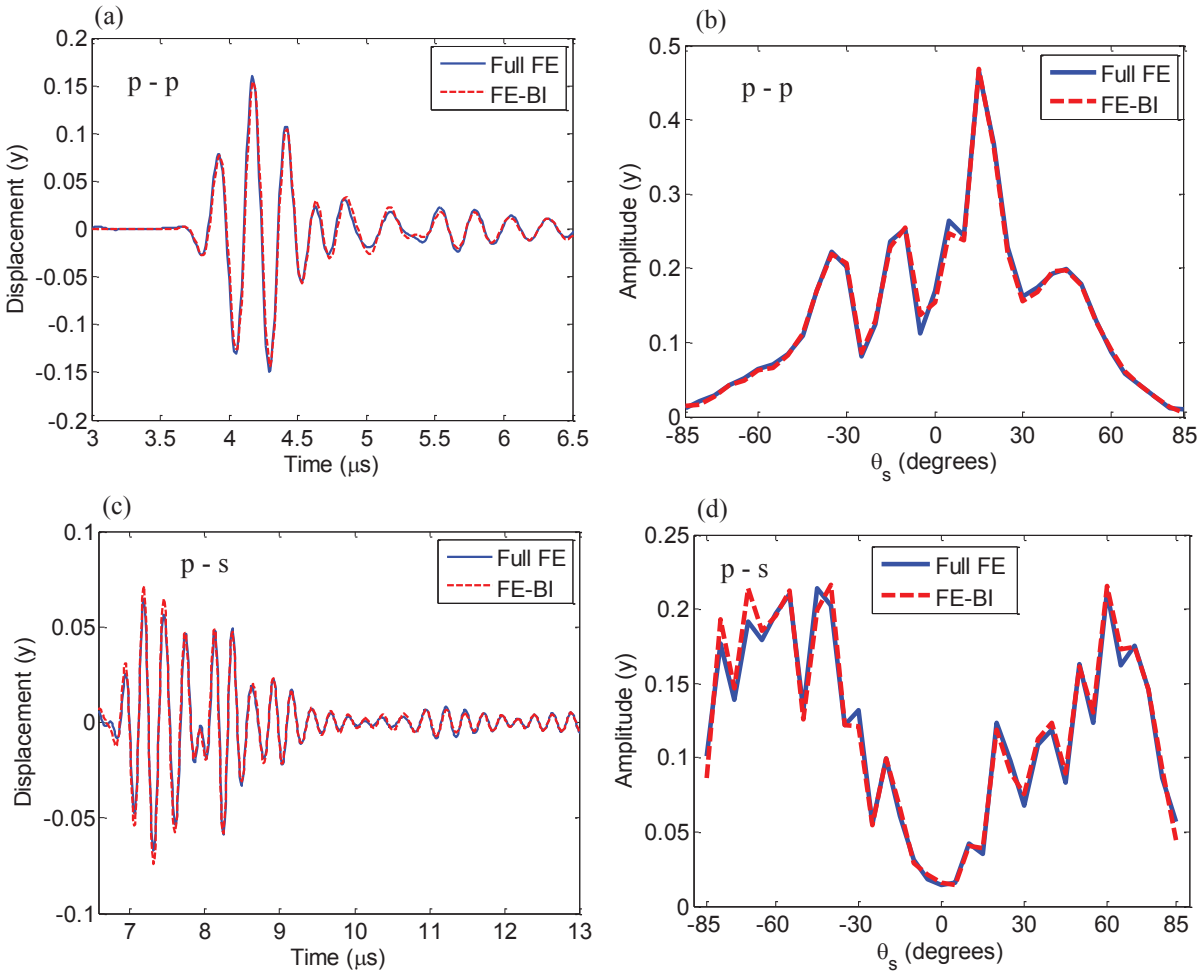

Figure 3.15: Comparison of the scattering signals (u_y) from a rough surface using the full FE model and the FE-BI method. (a) Scattering P-P signals when $\theta_s = 30^o$. (b) P-P Scattering amplitude (θ_s = -90 to 90^o). (c) Scattering P-S signals when $\theta_s = 30^o$. (d) P-S Scattering amplitude (θ_s = -90 to 90^o).

Some redundant waves are noticed propagating to the positive y-direction. These waves are generated by the excitation line due to the vibration of the source nodes in a free space.

For comparison with the full FE model, Fig. 3.14(b) shows the corresponding FE-BI method which is $29\times4\text{mm}^2$ ($\approx18.7\lambda_p\times2.6\lambda_p$). The excitation is realized by the nodes on the rough surface with forces calculated from Eq. (3.4) . Computed surface displacements are then substituted into the boundary integral Eq. (3.16) to obtain the scattering signals at the same monitoring points in the full FE model. For the rough surface, the scattered waveforms become much more complicated especially for the mode converted S waves, due to the increased diffuse field as shown in Fig.

3.15(c). However, good agreement of the P and S waveforms calculated from the full FE model and the FE-BI method are still found. In addition, the FE-BI method also accurately predicts the scattering amplitude across all the scattering angles, and the values of the MAE are 3.8% and 5.1% for P and S waves, respectively. The number of elements for the full FE model and the local FE box in Fig. 3.15(a) and (b) are 2.1 million and 47 thousand, and the computational effort is greatly reduced by the new method.

3.6.3 Spherical void and inclusion

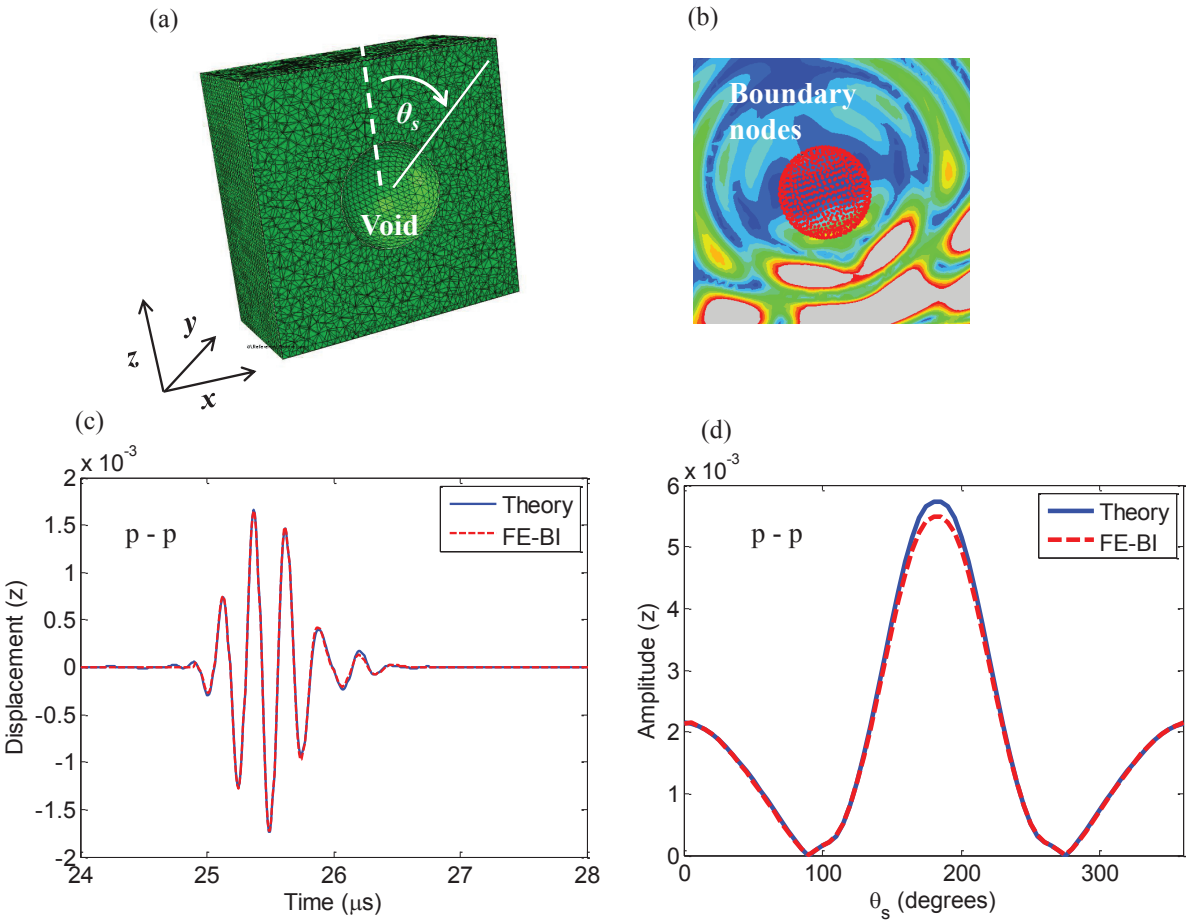

Figure 3.16: 3D simulation with a spherical void. (a) Meshing profile around the void. (b) Snapshot of the scattered waves around the void. (c) Scattering signals (u_z) when θ_s = 30^o using the theoretical solution and the FE-BI method. (d) Scattering amplitude (u_z) when θ_s = 0 to 360^o using the theoretical solution and the FE-BI method.

In 3D the plane wave scattering from a spherical void and an inclusion with the same shape are simulated. The computed results from the FE-BI method are then

compared with those calculated from the theoretical formulae [39] using separation of variables. It is currently very difficult to simulate a full 3D FE model due to the limit of computational power.

The dimensions of the 3D FE box are $6.2\times6.2\times7.2\text{mm}^3$ ($\approx 4\lambda_p\times4.7\lambda_p\times4\lambda_p$) as shown in Fig. 3.16, with the absorbing region being 1.5mm ($\approx 1\lambda_p$) thick. The spherical void with a diameter of 1.2mm ($\approx 0.77\lambda_p$) is created by subtracting a 3D solid sphere from the FE box. Linear tetrahedral elements (equivalent to C3D4 in Abaqus) with a size of around 0.075 mm ($\lambda_p/20$) is used to mesh the FE box with the free meshing algorithm. The total number of nodes is approximately 65 thousand.

Assuming a plane wave propagating in the negative z-direction, the excitation forces on the defect surface can be calculated using Eq. (3.4) . After executing the FE explicit scheme using Abaqus, the calculated surface displacements are substituted into Eq. (3.16) to calculate the scattering signals from 0 to 360^o. The distance between the observing points and the centre of the defect is approximately $100\lambda_p$. Fig. 3.16(a) shows the meshing profile around the void, and the animation of the scattering field is shown in Fig. 3.16(b) .

Fig. 3.16(c) shows good agreement of the scattering P wave signals when $\theta_s = 30^o$, using the FE-BI approach and the theoretical solution [39]. From Fig. 3.16(d), the MAE of the scattering amplitude between the two approaches is 2.1%. A small deviation of 4.2% can be seen when θ_s is around 180^o, corresponding to the transmission direction.

The same geometry and bulk material (Aluminium) are used for the simulation of the scattering from a spherical inclusion, filled with Alumina (Young's modulus, 390 GPa; density, 3950 kg/m^3; and Poisson ratio, 0.22). The impedance ratio for the compressional wave between the bulk medium and the inclusion is hence 0.40. In practice, the spherical inclusion and the cubic box without the sphere are meshed separately, and then joined to form the whole mesh shown in Fig. 3.17(a). Note that the two separate volumetric meshes should produce the same boundary mesh at the interface to make the volumetric mesh compatible.

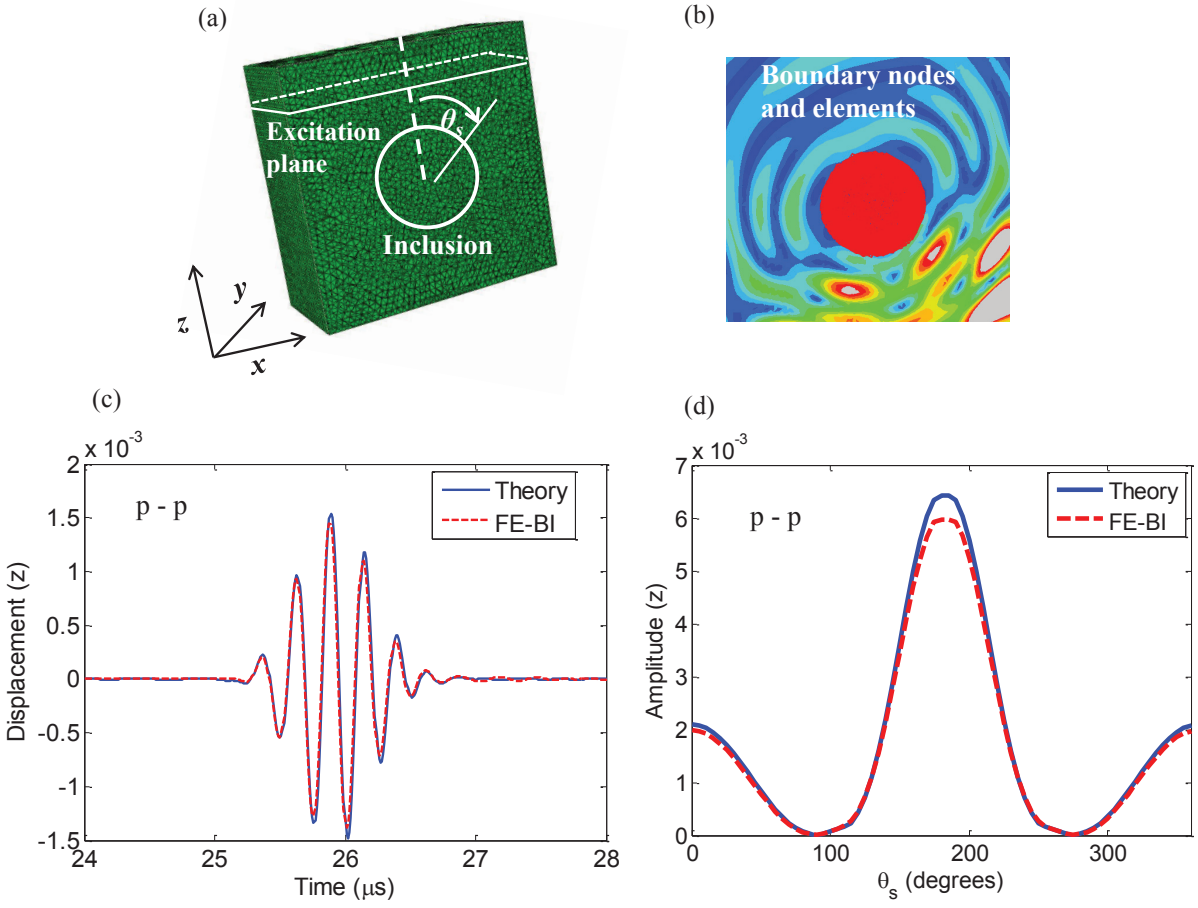

Figure 3.17: 3D simulation with a spherical inclusion. (a) Meshing profile around the inclusion. (b) Snapshot of the scattering field around the inclusion. (c) Scattering signal when $\theta_s = 30^o$ using the theoretical solution and the FE-BI method. (d) Scattering amplitude when $\theta_s = 0$ to 360^o using the theoretical solution and the FE-BI method.

The direct surface excitation of the inclusion is not used here because it is found to produce redundant waves similar to those shown in Fig. 3.14. For instance, exciting the lower half spherical surface would inevitably generate waves travelling in the positive z- direction, due to the vibration of the source nodes in the free space. These waves are unwanted and non-physical, which would pollute the scattering field. Hence an excitation plane 1mm above the inclusion is applied instead. In this manner, the redundant waves then only exist above the excitation plane, which travel directly to the absorbing region and would not affect the region of interest (e. g. the surface of the inclusion).

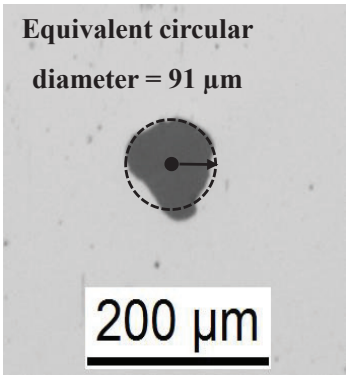

Figure 3.18: One raw image from the microscopic data showing a middle section of the void.

Fig. 3.17(b) shows the scattering field from the inclusion, and the surface nodes to record boundary displacements. Elements associated with these nodes are also selected to post-process the stresses, and an average is performed to estimate the stresses at the surface of the inclusion. By substituting the boundary velocities and tractions into the integral, the scattering signals at the observing points can be calculated. Good agreement between the theory and the simulation can be found in Fig. 3.17(c) and (d). A small error of the amplitude at the transmission direction ($\theta_s = 0^o$) might be caused by the fact that the linear tetrahedral element is not sufficiently accurate to estimate the boundary stress. A common way to improve the accuracy is to increase the mesh density, especially around the surface of the inclusion. Several alternative ways may be useful to recover the stresses more accurately based on the current mesh density [57]. For example, the nodal point forces (NPF) method as developed in [58] can potentially be implemented here.

3.7 Application to 3D realistic irregular void

Unlike the ideal spherical voids or inclusions, volumetric voids with rough surfaces are more commonly seen in practice. The author has been cooperating with researchers from Svenska Kullagerfabriken AB (SKF) for modelling the elastic wave scattering from realistic non-spherical voids [59]. Only numerical methods can be applied to solve the scattering problem, for instance, using the coupled FE-BI method.

Note that fundamental differences exist regarding the physical scattering from rough

voids and rough cracks mainly in two aspects. First of all, tip diffraction plays a less important role for the volumetric void. However, the surface irregularity (roughness), orientation, and the volume of the void have significant effects on the scattering behavior. For instance, it is obvious that the scattered waves from a sphere and an ellipse are different. Hence to study the scattering from a non-spherical void, one needs to consider more variables than scattering from a rough crack. Only a few related works can be found in astronomy and planetary science to investigate the light scattering from non-spherical particles [60]. In this section, elastic waves are considered and the study is based on a real sample of a non-spherical void obtained from microscopic images.

3.7.1 Reconstruction of the 3D defect from 2D images

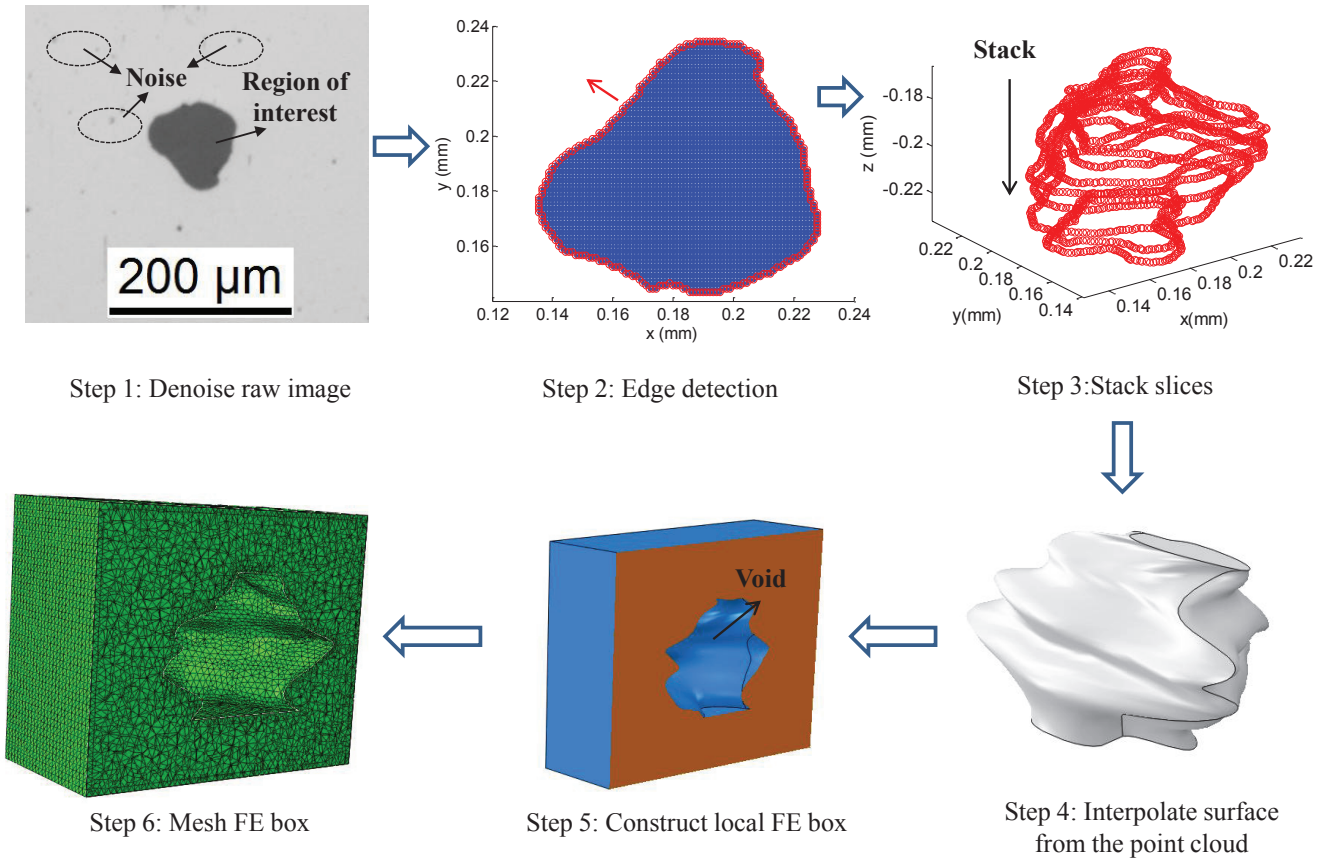

Figure 3.19: Procedure to construct the 3D FE mesh for the void from a set of 2D microscopic images (six steps).

In practice, it is not possible to obtain the 3D shape of the void directly since the microscopy scans the void at different positions. The raw data from SKF are multiple

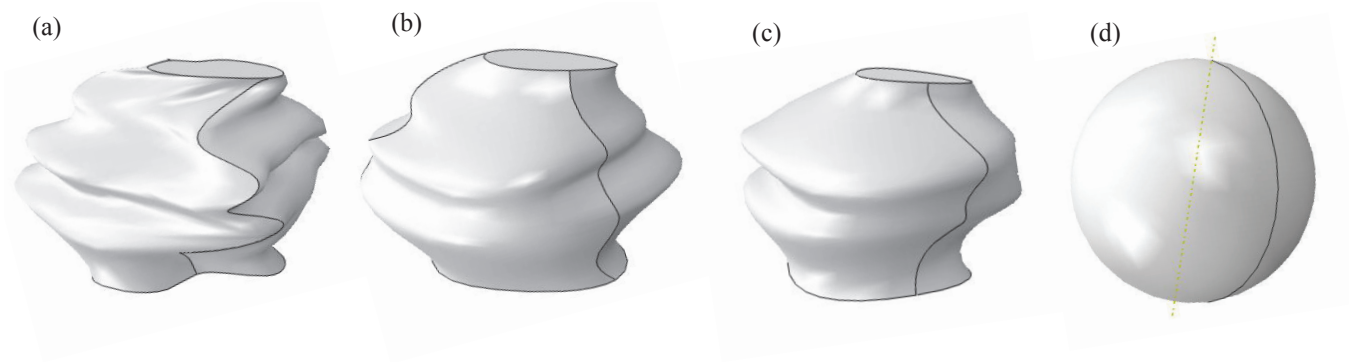

Figure 3.20: Reconstructed 3D voids. (a) V1. (b) V2. (c) V3. (d) Sphere.

2D images showing the horizontal slices in the x-y plane of the void, corresponding to different depths along the z-axis. In total eleven images are obtained and one typical raw image is shown in Fig. 3.18, in which the dark region in the centre refers to the actual slice of the void (data provided by SKF). A best fit of the irregular 2D shape with a circle is adopted to approximate the equivalent diameter and its centre location, as marked in Fig. 3.18.

To reconstruct the shape of the void it is necessary to stack all images following the depth. The reconstruction procedure is divided into six steps as illustrated in Fig. 3.19. First of all, the dark centre region is carefully selected and sparse 'noisy' spots are eliminated. The edge of the defect in each slice is detected by finding the peak of the gradient of the image pixels in the second step. Edges of all slices are then stacked following the depth, producing a point cloud of the surface of the void. In the fourth step, the point cloud is imported into the software Rhinoceros 3D (Robert McNeel Associate, Seattle, WA), and interpolation algorithms are applied to produce the CAD of the surface. The created CAD file is then imported into Abaqus to obtain the meshing profile of the FE box shown in the last two steps.

3.7.2 Effects of the irregularity

As mentioned the scattering field relies on the shape, the orientation, the surface irregularity and the volume of the void. In this section, the effects of the surface irregularity on the scattering field are investigated quantitatively.

Fig. 3.20(a) shows the reconstructed shape of the irregular void. By reducing the

$Searching\, region\, of\, \boldsymbol{P_c}\, and\, r_c$	
$range\, of\, \boldsymbol{P_c}(x_c, y_c, z_c)$	$[0.16, 0.16, -0.199]mm \sim [0.21, 0.21, -0.199]mm$
$range\, of\, r_c$	$0.019mm \sim 0.046mm$

Table 3.1: Searching region of $\boldsymbol{P_c}$ and r_c

number of the interpolation points using the built-in functions of Rhinoceros, the shape effectively becomes smoother as can be seen from Fig. 3.20(a) to (c). For comparison, a spherical void is also plotted in Fig. 3.20(d) by best-fitting the original point cloud. To determine the centre and the diameter of the best-fitted sphere, a searching algorithm is implemented in the sense of least squares:

$$\begin{cases} \hat{\boldsymbol{P}}_i = \frac{\boldsymbol{P_{vi}} - \boldsymbol{P_c}}{||\boldsymbol{P_{vi}} - \boldsymbol{P_c}||} \\ \hat{\boldsymbol{P}}_{\boldsymbol{si}} = \hat{\boldsymbol{P}}_i \cdot r_s + \boldsymbol{P_c} \\ \text{argmin} \sum_{\text{i}} ||\text{P}_{\text{si}} - \text{P}_{\text{vi}}||, (\text{P}_{\boldsymbol{c}} \in \text{R}^3, \text{r}_{\text{c}} \in \text{R}) \end{cases} \tag{3.29}$$

Where $\boldsymbol{P_c} = [x_c, y_c, z_c]$ is the coordinate of the centre of the sphere, r_c is the radius of the sphere, $\boldsymbol{P_{vi}}$ denotes the coordinate of the ith surface point from the raw data, and $\boldsymbol{P_{si}}$ is the coordinate of the ith point of the spherical void. The value of z_c can be determined directly as a average of the maximum and the minimum depth of the slice, hence the only unknown parameters are x_c, y_c and r_c. A searching region of $\boldsymbol{P_c}$ and r_c are predefined shown in Table 3.1. The lower and the upper bounds are set by observing the region of the defect. The best parameters are estimated by finding $\boldsymbol{P_c}$ and r_c, which give the minimum error in Eq. 3.29. Based on the data of the point cloud from the realistic void, the best-fitted sphere has parameters of $\boldsymbol{P_c}$ = [0.19, 0.18, -0.199]mm, and r_c = 0.04mm.

The FE-BI approach is implemented to calculate the scattered waves from the four voids in Fig. 3.20. The material for the bulk medium is steel (Young's modulus, 210GPa; density, 7800 kg/m3; and Poisson ratio, 0.29). A three-cycle tone burst with a centre frequency of 98MHz is used here for simulation, and the compressional and the shear wavelength in this case are 0.06mm and 0.03mm respectively. Hence the diameter of the best-fitted sphere is approximately $1.33\lambda_p$. The thickness of the absorbing region is 0.09mm ($\approx 1.5\lambda_p$), and the total size of the local FE box is

approximately $0.45\times0.45\times0.33\text{mm}^3$ ($\approx 7.5\lambda_p \times 7.5\lambda_p \times 5.5\lambda_p$). After computing the boundary displacement on the surface of the void using the FE model, the boundary integral is implemented to calculate the scattering signals at a distance of $100\lambda_p$ away. The scattering amplitude with θ_s ranging from 0 to 360^o in the x-z plane is obtained by picking the peaks of the scattering signals (u_z). Only the P-P case is considered here but the methodology can be equally applied to S waves with a more dense meshing profile. The number of nodes for one typical FE simulation is 2 million, which can be further reduced by optimizing the dimensions of the 3D FE box.

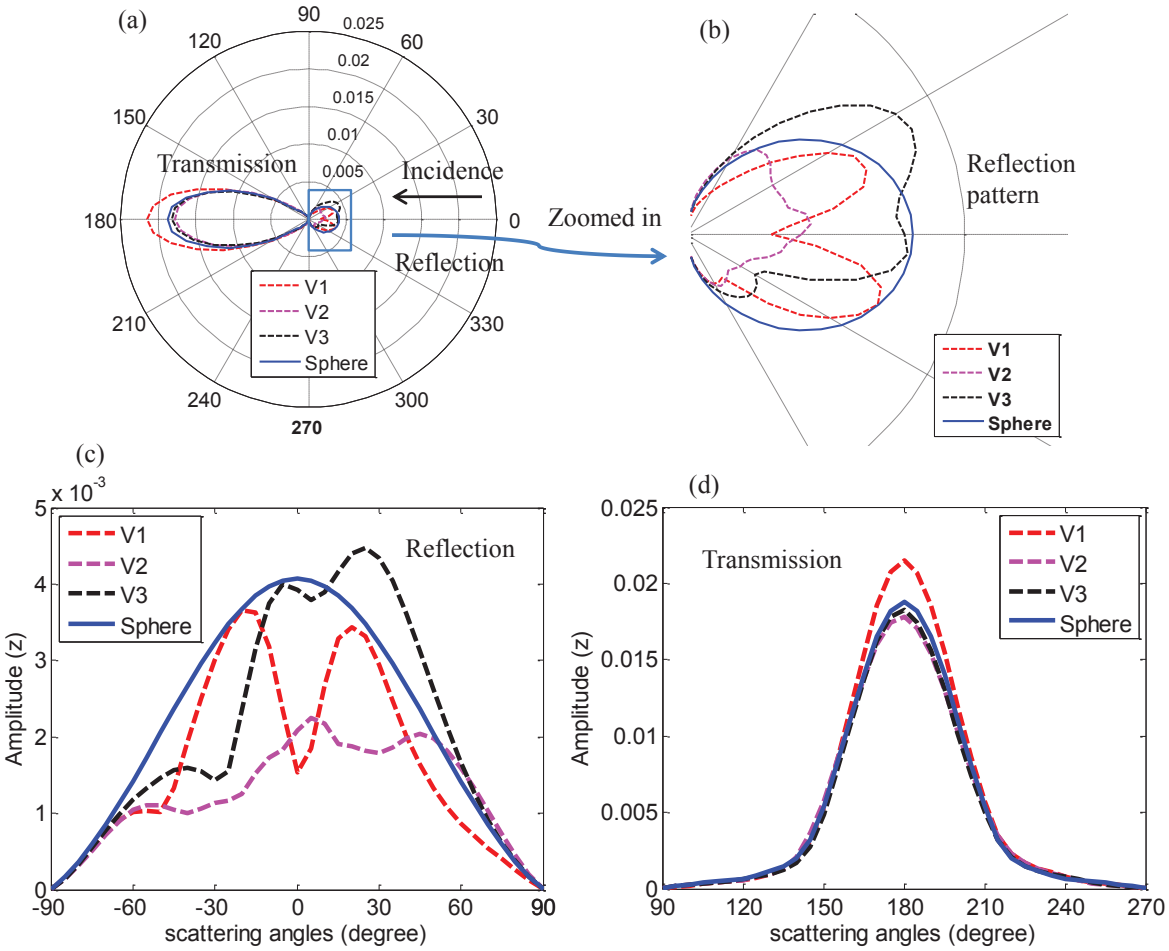

Figure 3.21: Scattering pattern for reconstructed voids and the spherical void. (a) Scattering pattern (u_z) in polar coordinates. (b) Zoomed-in reflection pattern (u_z) in polar coordinates. (c) Reflection pattern (u_z) in Cartesian coordinates. (d) Transmission pattern (u_z) in Cartesian coordinates.

Fig. 3.21 shows the scattering patterns of the P-P waves from $V1$ to $V3$ in polar

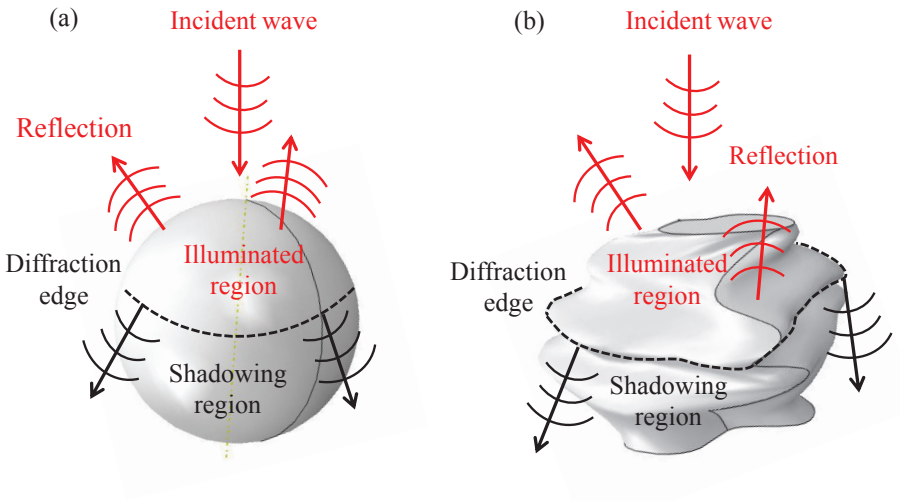

Figure 3.22: Sketch illustrating the reflection and the transmission of elastic waves for a 3D void. (a) Spherical void. (b) Non-spherical void (V1).

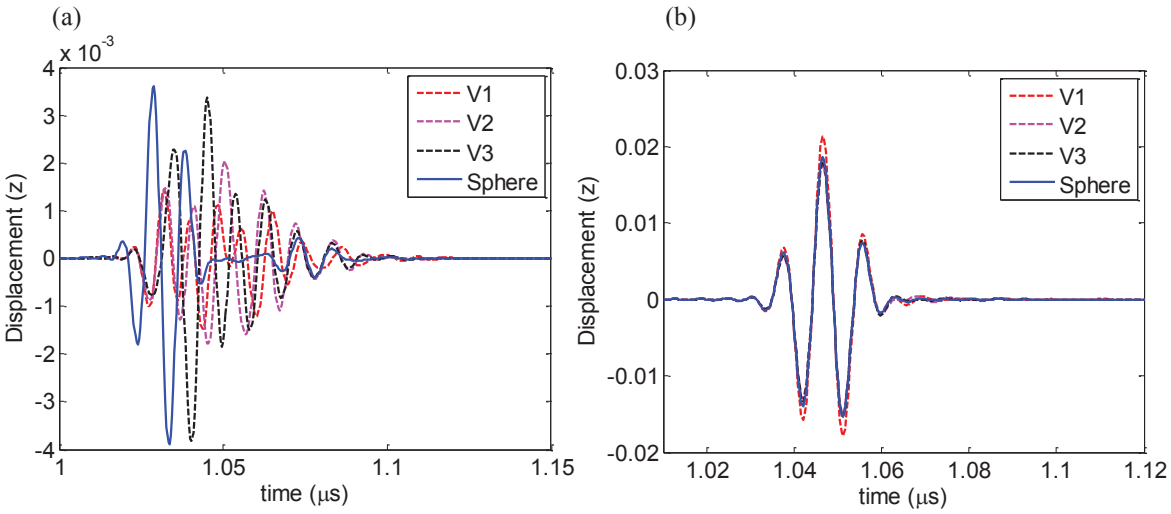

Figure 3.23: Scattering waveforms for different voids. (a) Backward reflection waveforms (u_z). (b) Forward transmission waveforms (u_z).

coordinates, along with the one for the best-fitted sphere. The amplitude has been normalized by that of the incident wave. The left part of Fig. 3.21(a) represents the transmission patterns and the right part refers to the reflection patterns. It is found that the transmission patterns are very similar with that from an ideal sphere, while the reflection patterns vary significantly with different reconstructed shapes as shown in the zoomed-in plot. $V3$ has the most similar pattern with that of the spherical void as expected. The change of the reflection patterns is more clearly demonstrated in Fig. 3.21(c) in Cartesian coordinates. Meantime the transmission patterns almost remain the same, although the amplitude for $V1$ is relatively larger

in Fig. 3.21(d).

A physical reasoning is given here to illustrate the difference between the reflection and the transmission behavior in Fig. 3.22. The whole surface of the void can be divided into the region illuminated by the incident wave and the shadowing region, between which there is a 'diffraction edge' connecting the two. Since the reflection mainly depends on the illuminated surface, the change of the illuminated surface for each void would cause a remarkable variation of the reflection pattern. In contrast, the transmitted waves are mostly contributed from the secondary-sources located at the 'diffraction edges', instead of the whole illuminated surface. Therefore compared with the reflection, the transmission is less affected when changing the shapes.

Fig. 3.23 shows the scattering waveforms in the backward (reflection) and forward (transmission) directions, in comparison with the reference from the best-fitted spherical void. The forward scattering waveforms when $\theta_s = 180^o$ are all similar with the one from the sphere as expected. However, the backward reflection signals when $\theta_s = 0^o$ become very complicated and deviate significantly compared with the reference. There is also a profound delay of the arrival time for each shape, since the top point of the reconstructed void is lower than that of the sphere. In summary, the irregularity of the reconstructed void has a profound effect on the reflection, rather than the transmission considering both the amplitude and the waveform.

3.8 Summary

A coupled finite element boundary integral numerical approach is applied and developed in the time domain, for accurate computation of the elastic wave scattering from irregular defects in both near and far fields. This methodology efficiently combines the time step FE simulation, absorbing layers, mixed meshing algorithm, internal forcing and the boundary integral. The accuracy is demonstrated by comparing the computation results with those from full FE models and the theoretical solutions, showing very good agreement in all numerical examples. In addition, the approach is applied to investigate the scattering field from realistic non-spherical voids. The effect of the irregularity of the void is studied and compared with a smooth spherical void. It is shown that the irregularity has a more considerably

influence on the reflection than the transmission. In particular, the numerical approach enables the study of the elastic wave scattering from randomly rough defects via the Monte Carlo simulations. In addition, it can also serve as a benchmark to evaluate analytical or approximation based scattering theory.

Chapter 4

Evaluation of the Elastodynamic Kirchhoff Approximation

4.1 Introduction

In this chapter the validity of the elastodynamic Kirchhoff approximation used for calculating the scattered waves from randomly rough surfaces is examined. A complete literature review is given regarding previous evaluation studies, which are mainly for acoustic/electromagnetic waves, and all of them are limited in 2D simulations with 1D surfaces. In order to evaluate the performance of the elastodynamic KA, Monte Carlo simulations are run on Gaussian surfaces with the elastic wave Kirchhoff model. The results are compared with those calculated using the numerical model developed from Chapter 3. Error analysis is provided to generalize empirical rules for the validity of the elastodynamic KA, and the rules are found to be different in 2D and 3D.

Although numerical methods as discussed in Chapter 3 can solve most elastic wave scattering problems, approximation based methods are still very attractive because of reduced requirements of the computation resources. Besides, approximation based methods are developed from physical assumptions with mathematical simplifications, which are often used to analyze the nature of the underlying wave physics. Among many such methods, the Kirchhoff approximation (KA) is a very powerful tool to calculate the scattering from rough surfaces. It has been widely applied in many fields, such as electromagnetic remote sensing [6], underwater acoustics

[28], and seismic waves [26, 37], to study the surface scattering statistics. For elastic waves there is also increasing interests in nondestructive evaluation (NDE) and ultrasonics in applying the KA to understand the scattering behavior from rough defects.

However, it is known that the Kirchhoff approximation is based on the tangential plane assumption and it neglects multiple scattering, surface waves etc.. Hence it is necessary to know when the use of KA should be anticipated to be reliable, particularly as it is applied for safety inspection. Historically there have been several attempts to evaluate the accuracy of KA, which are summarized in the book by Ogilvy [4]. The most frequently cited validity criterion for KA is $kr_c \cos^3 \theta_i \gg 1$, in which r_c is the local radius of curvature and θ_i is the global angle of incidence. However, this criterion is derived only from a simple geometrical argument. More rigorous approaches were also applied to give better evaluation results. For instance, in [29] a variational principle was adopted to quantify the accuracy of KA. Thorsos [28] performed a comparison of the acoustic scattering pattern using the numerical boundary integral method and the Kirchhoff model with random Gaussian surfaces. The correlation length λ_0 is concluded to be the most critical parameter rather than the surface curvature. A similar study was extended to a Pierson-Moskowitz sea surface [8], in which the KA was found to be accurate near the specular direction with incident grazing angles as low as 10^o; this is typical of the impressive accuracy and utility that led to the wide spread use of the Kirchhoff model.

The validity of the vector wave KA (e. g. electromagnetics and elastodynamics) differs from the scalar case. The difference is because restrictions on surface properties that arise from effects such as shadowing and multiple scattering can be made more severe by mode conversions, into bulk waves and surface waves. In [30], the scattering pattern from rough surfaces was computed using the method of moment and the Kirchhoff model, indicating that electromagnetic Kirchhoff KA is valid when $k\sigma \leq 0.2$ and $k\lambda_0 \leq 2$ even with small angles of incidence. Robertsson et al. [26] compared the elastodynamic KA with the finite difference method and the spectral element method (SEM) with an application in reflection seismology. In this work, some discrepancies between the KA and the other two methods were shown particularly in terms of amplitude. The accuracy of the elastic wave KA in the backscattering direction was studied [31] by comparison with the BEM, with application in NDE.

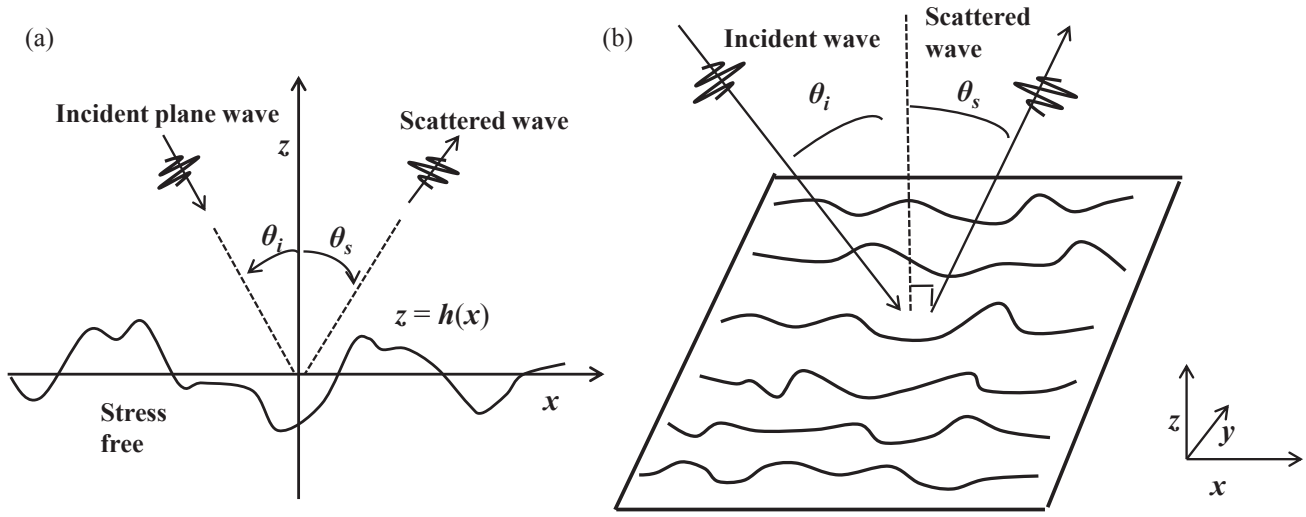

Figure 4.1: Sketch of the scattering geometry: Plane wave in an elastic material incident on an infinitely long surface with stress-free boundary condition. (a) 1D surface. (b) 2D surface.

Zhang et al. [23] calculated the scattering matrix from Gaussian rough defects in comparison with a finite element local scattering model and argued that the elastic KA is accurate with the roughness $\sigma \leq 0.3\lambda$ and $\lambda_0 \geq 0.5\lambda$ at incidence and scattering angles over the range from -80^o to 80^o. However, the conclusions were drawn from the modelling of the ultrasonic scattering from a crack. Hence the physical tip diffraction was included during the comparison, that might affect the comparison results at grazing angles.

In addition, all of the previous evaluation works are only based on 1D rough surfaces using 2D models due to limitations in the simulation approaches. The 3D scattering from a 2D rough surface is fundamentally different, and researchers developing modelling tools using 3D KA for NDE in the power industry have observed significant differences of several dB between experimentally measured reflections from rough defects and KA simulations of the same case [27]. The discrepancies arise because surface scattering is an inherently complex process, involving phenomena such as mode conversions, surface waves and shadowing, which are not at all included in the Kirchhoff approximation. These phenomena are known to cause the greatest errors when the angle of incidence or the roughness is large, and are also expected to be different for 2D and 3D. Therefore, to gain a comprehensive understanding of

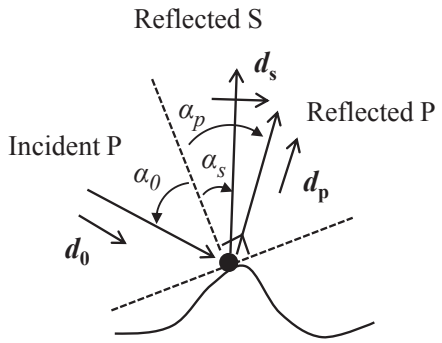

Figure 4.2: Sketch of the elastodynamic Kirchhoff approximation at one surface point.

the performance of the 3D Kirchhoff approximation on random rough surfaces, with height variations in both x- and y- directions, it is necessary to actually simulate the full 3D problems.

In this chapter the range of validity of both 2D and 3D elastodynamic KA are carefully examined by comparing results with those from the numerical method developed in Chapter 3. The comparison is performed in the time domain directly considering the measured signals during a real inspection. A brief review of the Kirchhoff approximation is given, along with the benchmark numerical model for comparison. The Monte Carlo simulations are then run for both methods using 1D and 2D surfaces with Gaussian spectra. Based on the simulation results, a thorough error analysis is performed to investigate the effects of surface roughness, scattering/incidence angle and the dimension on the accuracy of KA.

The scattering model in this chapter is, as close as possible, the scattering of a plane wave from an infinite rough surface and the scattering geometries are drawn in Fig. 4.1(a)(2D model with a 1D surface) and (b)(3D model with a 2D surface). Note that for the scattering in 3D, only incident/scattering waves in the x-z plane is investigated for simplicity.

4.2 Kirchhoff approximation

4.2.1 Tangential plane assumption

The elastic wave Kirchhoff approximation is depicted in Fig. 4.2, where a plane P wave is assumed to be incident on the rough surface. The KA assumes that the motion of one point on the surface is the same as if the point were part of an infinite tangential plane illuminated by the incident wave. The total displacement at this point is linearized as a summation of the incident P wave and the reflected P/S waves:

$$\boldsymbol{u}_p = \boldsymbol{d}_0 + r_{pp}\boldsymbol{d}_p + r_{ps}\boldsymbol{d}_s. \tag{4.1}$$

Here $\boldsymbol{u}_p$ represents the boundary displacement with an incident P wave, r_{pp} and r_{ps} are the reflection coefficients of P and S waves respectively, and $\boldsymbol{d}_0$, $\boldsymbol{d}_p$ and $\boldsymbol{d}_s$ are the displacement polarization vectors for the incident P and reflected P/S waves. According to the Snell's law:

$$\alpha_p = \alpha_0, \frac{\sin\alpha_s}{\sin\alpha_0} = \frac{c_s}{c_p} = \gamma \tag{4.2}$$

where γ is the S-to-P wave speed ratio, and α_0, α_p and α_s are local incidence/reflection angles with respect to the normal of the tangential plane. The local reflection coefficients are given by:

$$\begin{aligned} r_{pp} &= \frac{\gamma^2 \sin 2\alpha_0 \sin 2\alpha_s - \cos^2 2\alpha_s}{\gamma^2 \sin 2\alpha_0 \sin 2\alpha_s + \cos^2 2\alpha_s} \\ r_{ps} &= \frac{2\gamma \sin 2\alpha_0 \cos 2\alpha_s}{\gamma^2 \sin 2\alpha_0 \sin 2\alpha_s + \cos^2 2\alpha_s} \end{aligned} \tag{4.3}$$

The surface point effectively acts as a dipole and the scattered waves are formed by superposition of radiating waves from all dipoles. By substituting the boundary displacement approximated using Eq. (4.1) to (4.3) into the boundary integral formula Eq. (3.16), the scattered waves at the receiver can be calculated. The boundary integral can be performed either in the time domain directly, or in the frequency domain with the use of FFT to recover the signals.

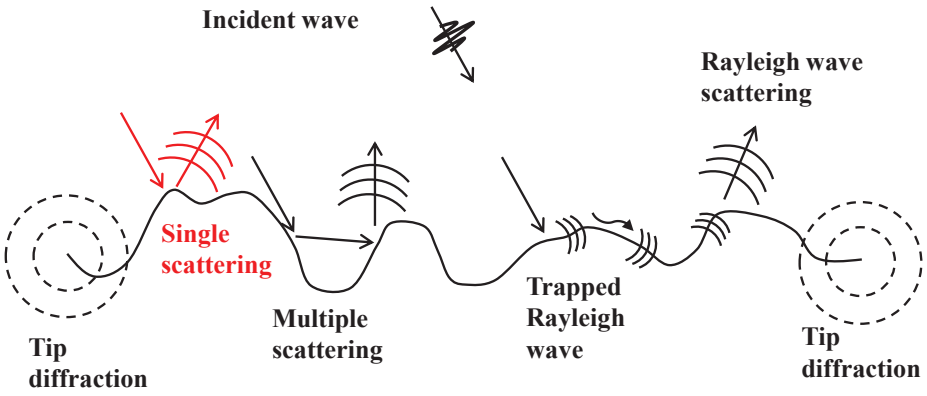

Figure 4.3: Sketch of the scattering from a rough surface including all the physical phenomena (Red color denotes the single scattering mechanism which the KA can model).

4.2.2 Local and global errors

The accuracy of the Kirchhoff assumption is determined by both the local and the global effects. From the mathematical basis of KA in Eq. (4.1), one can immediately realize that the validity of KA fundamentally depends on whether the tangential plane assumption is reliable or not, which relies on the local roughness at this surface point. According to the geometrical argument, the local radius of curvature must be large enough to obey $kr_c \cos^3 \theta_i \gg 1$ [4], And the resulting errors are hence called the local errors.

In contrast, the global errors are much more complicated since they are contributed from the global shape of the surface. Fig. 4.3 demonstrates different global wave phenomena that the KA cannot take into account. Note that the conventional KA assumes a single scattering mechanism, while in the community of optics, there are several studies considering high-order KA by including multiple scattering physics [61, 62]. In this thesis, the definition of the conventional KA is utilized. Apart from the multiple scattering, it is impossible to see the Rayleigh wave, and subsequently the conversions between the surface waves and the bulk waves. In addition, KA is also poor at modelling the edge diffraction. As can be seen, the gobal error is difficult to be quantified as it has different wave mechanisms stated by Thorsos [28]. Hence, more accurate numerical simulations are implemented as a full elastic wave benchmark to investigate accuracy of the KA, considering both global and local er-

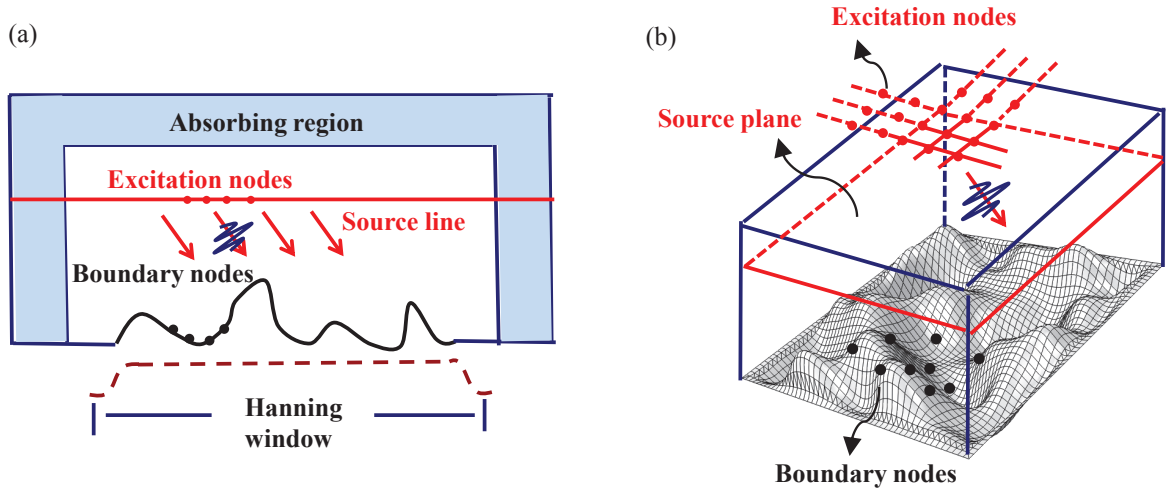

Figure 4.4: Sketches of the finite element boundary integral model to calculate the scattering waves from a rough backwall. (a) 2D model with a 1D surface. (b) 3D model model with a 2D surface.

rors. Generally speaking, in terms of the global effect the KA is reasonably good if the received scattering signals are mainly dependent on the single scattering mechanism. However, once one of the global effects outweighs the single scattering, the KA would not be reliable. For instance, higher roughness leads to severe multiple scattering, which is beyond the reach of KA.

4.3 Numerical benchmark model

The coupled FE-BI method as described in Chapter 3 is implemented here as a benchmark, since it offers sufficiently accurate results once the convergence criteria are satisfied. The software package Pogo [43] is incorporated to solve the FE problems, as thousands of realizations will be used for the Monte Carlo simulations.

The local FE box to calculate the scattering from a rough surface when internal waves are incident, is shown in Fig. 4.4. A rough surface with surrounding flat surfaces is constructed, and a spatial Hanning window is multiplied to achieve the smooth transition between the rough and the flat part. An internal plane P wave is excited by forcing along a line located just above the rough backwall. Forces calculated from the known incident wave displacement field using Eq. (3.2) in Chapter 3, are given into the excitation nodes. Two tips of the excitation line need to be

buried into the ends of the absorbing region to prevent any unwanted circular-crested waves, which would otherwise be generated from the two tips.

Boundary displacements on the rough surface computed from the FE simulation are used in Eq. (3.16) to calculate the scattered waves. Before substituting the displacements into the boundary integral, a Hanning window function is multiplied, to reduce the 'edge effects' for the approximation of an infinite surface. In 2D a popular way to approximate the plane wave scattering from a truncation to an infinite long surface is to use a tapered plane wave [56]. In this approximation the half beam width must be much smaller than the surface length to eliminate the tip effects, but roughly larger than 3λ to approximate the plane wave. This tapering idea was successfully applied in the second numerical example in Chapter 3 to simulate the scattering from a rough surface. Unfortunately in 3D it is difficult to satisfy both criteria simultaneously due to the limited size of the 2D surface that can be simulated. Hence a compromised approach is applied to smooth the boundary displacement with a Hanning window. Although circular-crested waves from the edges cannot be completely canceled, the method does mitigate the effect substantially. The 3D FE cubic box is also shown in Fig. 4.4(b). Note that, for brevity, the absorbing region in 3D is not drawn here.

4.4 Monte Carlo Method

The material for the simulation is Aluminium with Young's modulus of 70GPa, density of 2700kg/m^3 and Poisson's ratio of 0.33. Thus the compressional wave speed is 6198m/s, and the shear wave speed is 3122m/s. A five-cycle Hanning windowed tone burst signal with a centre frequency of 4MHz is assumed, and the compressional and shear wavelengths are $\lambda_p = 1.55$mm and $\lambda_s = 0.78$mm, respectively. The distance from the surface centre to the observing point is 50mm ($\approx 32\lambda_p$).

Surfaces with Gaussian power spectra are generated using the moving average method introduced in Chapter 2. In 2D models, 15 different 1D rough surface profiles are simulated with RMS $\sigma = \lambda_p/8$, $\lambda_p/6$, $\lambda_p/5$, $\lambda_p/4$, and $\lambda_p/3$, and correlation lengths $\lambda_0 = \lambda_p/2$, $\lambda_p/3$ and $\lambda_p/4$. While in 3D simulations, 10 isotropic rough surface

profiles are used with the same RMS values as those of the 2D cases, and with correlation lengths $\lambda_0 = \lambda_p/2$, $\lambda_p/3$.

For each roughness, simulations are run on 50 realizations of surfaces, to calculate the scattering signals with multiple incidence/scattering angles ($0^o \leq \theta_i \leq 30^o$, $-90^o \leq \theta_s \leq 90^o$, both in a step of 5^o). The number of realizations is chosen by considering the conflicting requirements of the statistical stability and the computational cost, especially in 3D. Hence in total it is required to run 5250 FE simulations in 2D, and 3500 simulations in 3D. NDT inspection always utilizes the amplitude rather than the phase of the scattering signals, since the probability of detection mainly depends on the amplitude [5]. It might also be interesting to study the phase, for example if the KA is used for imaging the surface. However the phase is not pursued here as the thesis focuses on the detection problem. The main quantity for comparison is therefore the sample averaged peak amplitude of the scattering signals. In addition, the mean and the variance of the error between the KA and the FE model are both investigated. In this study the simulations are run only for the P-P mode, and the similar procedure can be performed for other modes (e. g. P-S, S-P and S-S modes).

4.4.1 2D simulations using 1D rough surfaces

2D FE models with 1D surfaces are meshed by linear triangular elements (equivalent to CPE3 in Abaqus) with an element size of $\lambda_p/30$, sufficient for the convergence requirement. The length of the 1D surface is about 8mm ($\approx 5.2\lambda_p$). The mixed meshing is performed so that the region surrounding the rough surface is automatically meshed and the remaining region is regularly meshed. The 2D FE domain has a dimension of 14.8×9.4 mm^2 ($\approx 9.6\lambda_p \times 6.1\lambda_p$), and the thickness of the SRM [48] absorbing layers is 2.4mm ($\approx 1.5\lambda_p$). The element size is 0.05mm ($\approx \lambda_p/30$) and the number of nodes for one 2D model is around 5.5 thousand. The FE model is calculated with Pogo, and the time spent at each stage of the simulation is summarized in Table 4.1.

The scattering displacement along each scattering direction is extracted by using

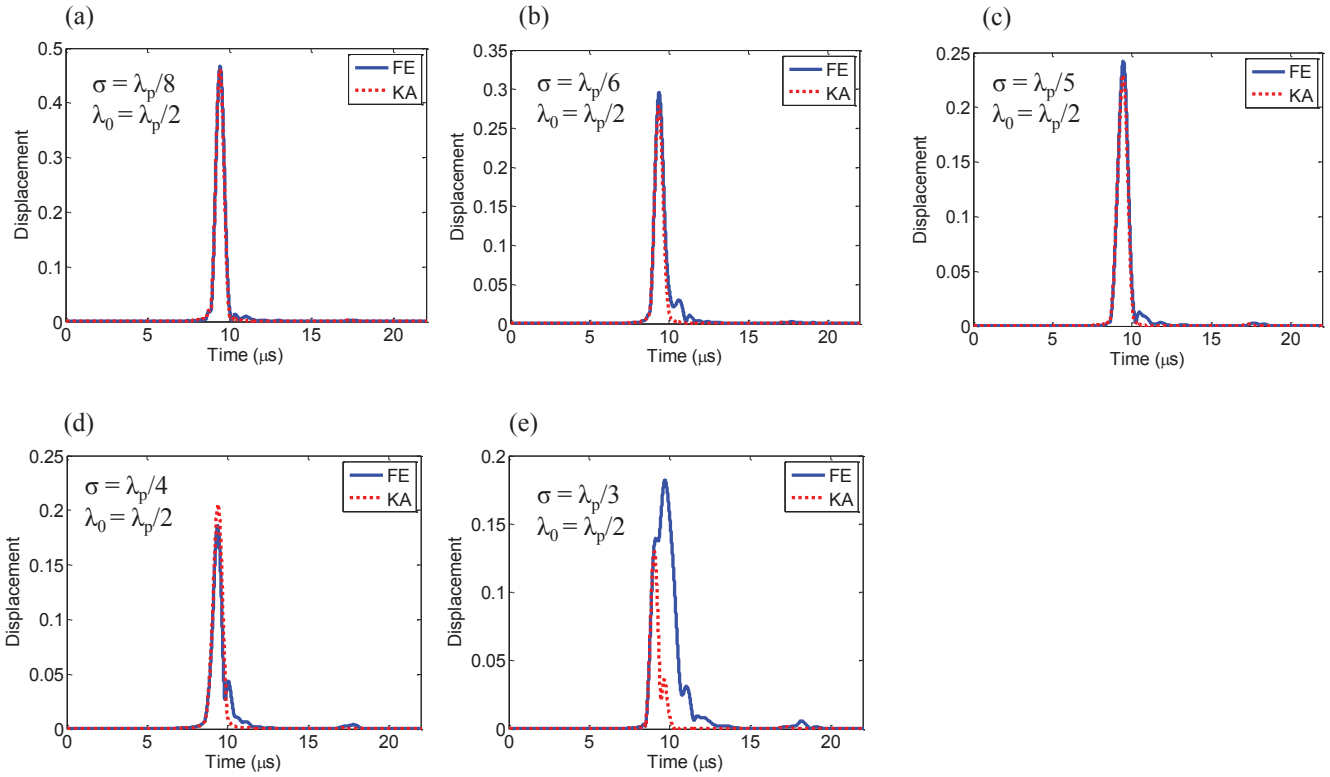

Figure 4.5: Envelopes of the normal pulse echo scattering signals from one realization of surfaces with different roughnesses. (a) $\sigma = \lambda_p/8$, $\lambda_0 = \lambda_p/2$. (b) $\sigma = \lambda_p/6$, $\lambda_0 = \lambda_p/2$. (c) $\sigma = \lambda_p/5$, $\lambda_0 = \lambda_p/2$. (d) $\sigma = \lambda_p/4$, $\lambda_0 = \lambda_p/2$. (e) $\sigma = \lambda_p/3$, $\lambda_0 = \lambda_p/2$.

$\boldsymbol{u}_p = \boldsymbol{u}_x \sin\theta_s + \boldsymbol{u}_z \cos\theta_s$. Fig. 4.5 shows envelopes of the scattering signals from one realization when $\theta_i = \theta_s = 0^o$, with increased RMS values and the same correlation length. The amplitude is shown on a linear scale, normalized by the peak of the normal pulse echo response from a flat surface of the same size. As can be seen from Fig. 4.5(a) to (d), the scattering signals calculated from KA agree well with those from the numerical approach, when $\sigma \leq \lambda_p/4$. Such a good agreement can no longer be seen in Fig. 4.5(e) ($\sigma = \lambda_p/3$), indicating that KA then becomes inaccurate. In addition, the amplitude of the scattered waves decays significantly as the roughness increases. The scattering waveforms become more complicated and a clear second arrival can be seen around 17μs. From an estimation of the arrival time, which equals to 4mm/(6198m/s) + 50mm/(3122m/s) = 16.7μs, one can notice that the second arrival is the mode converted shear wave due to the roughness.

By extracting the peak of the scattering signal at each angle, sample averaged scattering patterns are shown in Fig. 4.6 to further evaluate the accuracy of KA. Note

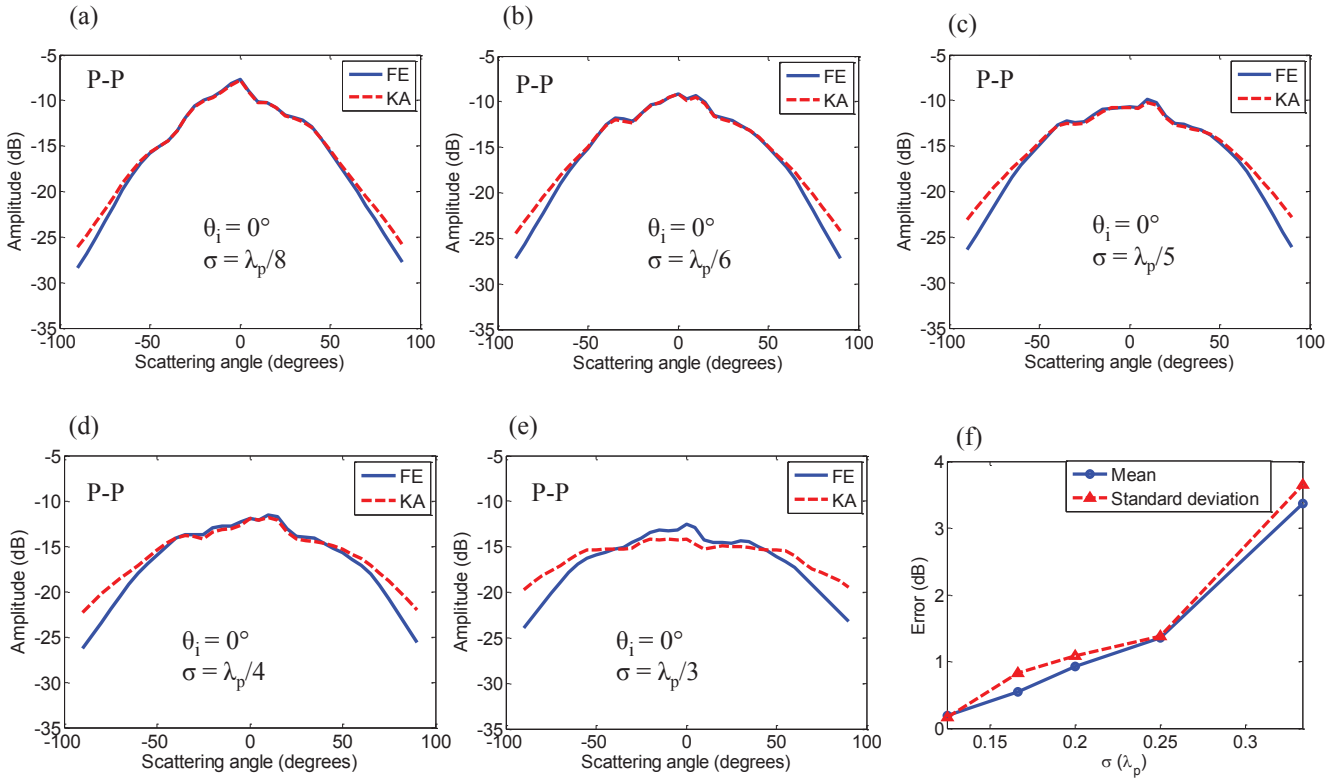

Figure 4.6: Comparison of the averaged peak amplitude of the scattering signals from 50 realizations between 2D FE and KA when $\theta_i = 0^o$ and $-90^o \leq \theta_s \leq 90^o$. (a) $\sigma = \lambda_p/8$, $\lambda_0 = \lambda_p/2$. (b) $\sigma = \lambda_p/6$, $\lambda_0 = \lambda_p/2$. (c) $\sigma = \lambda_p/5$, $\lambda_0 = \lambda_p/2$. (d) $\sigma = \lambda_p/4$, $\lambda_0 = \lambda_p/2$. (e) $\sigma = \lambda_p/3$, $\lambda_0 = \lambda_p/2$. (f) Mean value and the standard deviation of the error when $\theta_i = \theta_s = 0^o$.

that the angular spread of the pattern is caused by both the finite length of the crack and the presence of the roughness. Here the amplitude is shown on a dB scale, normalized by the normal pulse echo response from a flat surface. If more realizations are run the graph is expected to become symmetric about $\theta_s = 0^o$. The range of the scattering angle θ_s for which KA is acceptable is from -70^o to 70^o when $\sigma \leq \lambda_p/4$, assuming that the tolerance of error is set to be 1dB, as is commonly used in NDE.

However, the KA no longer agrees with the FE when $\sigma \geq \lambda_p/3$, even at the specular angle (0^o in Fig. 4.6). Furthermore, KA tends to underestimate the amplitude around the specular scattering angle, while it overestimates the amplitude at near grazing angles. This can be explained by the fact that KA does not include multiple scattering effects. The consequence is that less energy is reflected back to the specular direction, and more energy than expected is distributed at near grazing angles.

Stage	*Time* (2*D model*)	*Time* (3*D model*)
Preprocessing	12*secs*	4*mins*50*secs*
FE (*Pogo*)	7*secs*	1*min*21*secs*
Boundary integral (37 *angles*)	8*secs*	42*secs*
Total (*One realization*)	27*secs*	6*mins*53*secs*
Monte Carlo	$\approx 39hrs$	$\approx 16days$

Table 4.1: Time spent at each stage and the total time for 2D and 3D simulations

Fig. 4.6(f) shows that both the mean absolute value and the standard deviation of the error at the normal backscattering direction increase as RMS increases. The mean absolute error and the standard deviation are calculated using the following equations:

$$\begin{aligned} \bar{E} &= \frac{1}{N}\sum_{n=1}^{N} E_n = \frac{1}{N}\sum_{n=1}^{N} |A_n^{KA} - A_n^{FE}| \\ \mathrm{std(E)} &= \sqrt{\frac{1}{\mathrm{N}}\sum_{\mathrm{n=1}}^{\mathrm{N}}(\mathrm{E_n} - \bar{\mathrm{E}})^2} \end{aligned} \tag{4.4}$$

Here $\bar{E}$ is the mean absolute error, E_n is the absolute error for one realization, and N is the total number of realizations. A_n^{KA} and A_n^{FE} are the scattering amplitudes calculated from KA and FE for one realization respectively. The standard deviation of the error is std(E).

4.4.2 3D simulations using 2D rough surfaces

In this section, full 3D FE simulations are deployed using 2D surfaces with roughness in both x- and y- directions. All of the previous evaluation works only consider 1D surfaces to simplify the model [23, 28, 29]. Although the range of validity for the 3D KA might, intuitively, not differ from the 2D KA much, some discrepancy between the two is expected caused by more local and global effects.

Fig. 4.7(a) shows a 2D CAD rough surface created using the software Rhino (Robert McNeel & Associates, Seattle, WA). A surface point cloud is first generated using the moving average method, and a spline interpolation algorithm is applied to form a surface. Note that the interpolation needs to guarantee that the produced surface

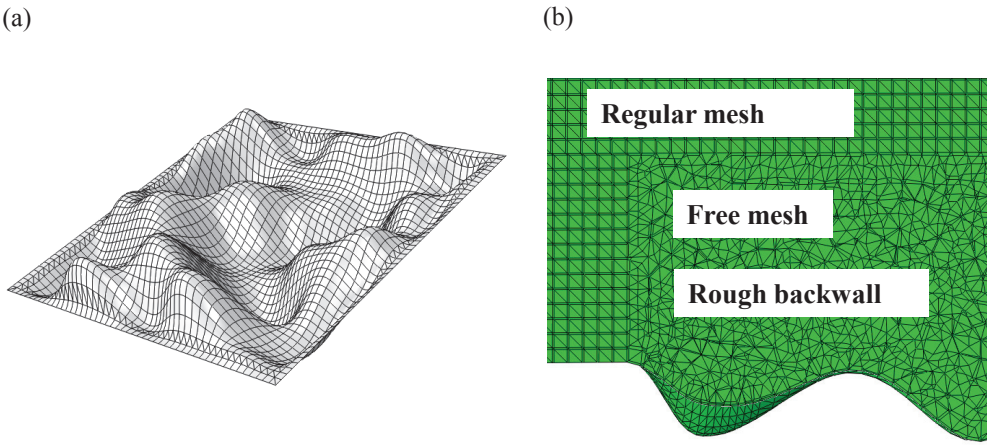

Figure 4.7: Construction of the 3D FE meshing. (a) CAD of the rough surface ($\sigma = \lambda/3$, $\lambda_0 = \lambda/2$). (b) Cross section view of the meshing domain.

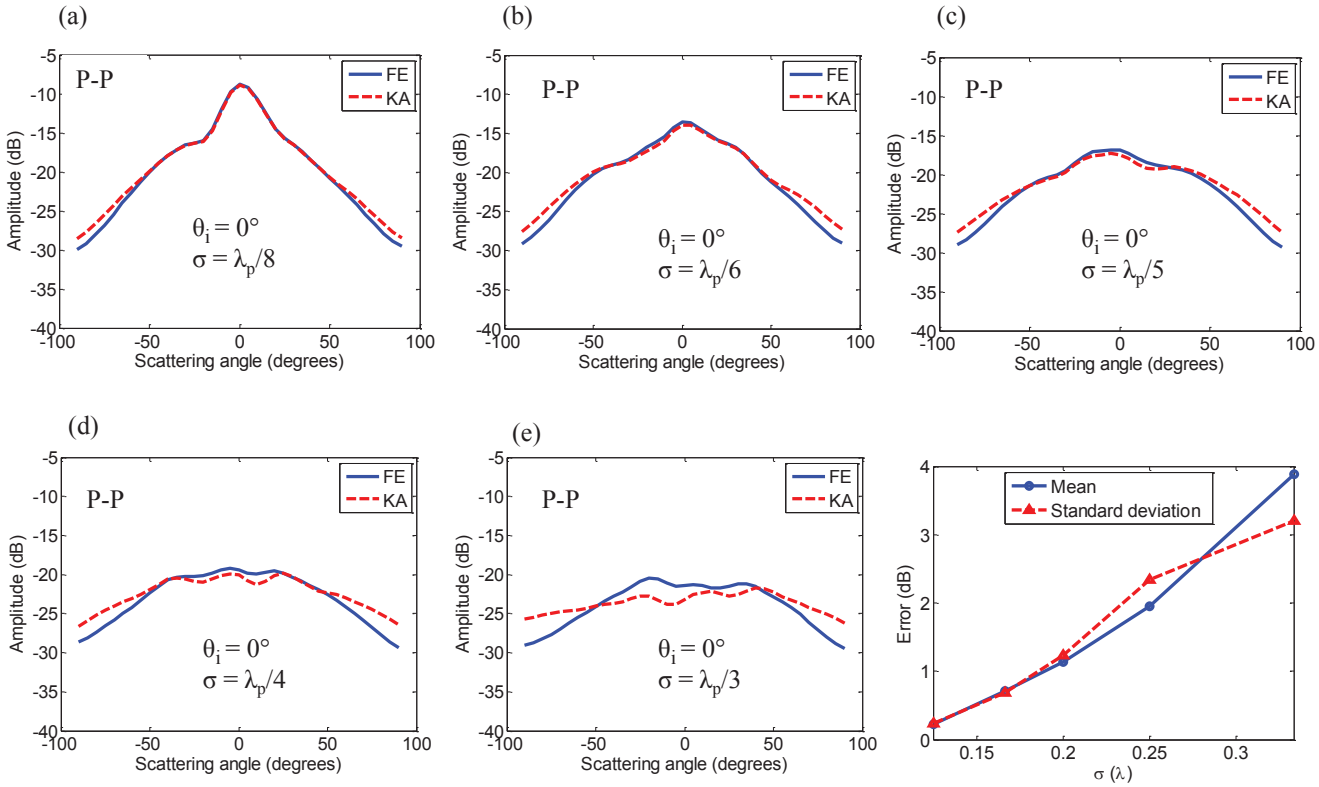

Figure 4.8: Comparison of the averaged peak amplitude of the scattering signals from 50 realizations between 3D FE and KA when $\theta_i = 0^o$ and $-90^o \leq \theta_s \leq 90^o$. (a) $\sigma = \lambda_p/8$, $\lambda_0 = \lambda_p/2$. (b) $\sigma = \lambda_p/6$, $\lambda_0 = \lambda_p/2$. (c) $\sigma = \lambda_p/5$, $\lambda_0 = \lambda_p/2$. (d) $\sigma = \lambda_p/4$, $\lambda_0 = \lambda_p/2$. (e) $\sigma = \lambda_p/3$, $\lambda_0 = \lambda_p/2$. (f) Mean value and the standard deviation of the error when $\theta_i = \theta_s = 0^o$.

exactly passes through the point cloud, to avoid any smoothing that would naturally be induced by most interpolation algorithms. The dimensions of the rough surface

are $5\times5\text{mm}^2$ ($\approx 3.3\lambda_p\times3.3\lambda_p$).

The corresponding 3D FE cubic box has dimensions of $12.8\times12.8\times4.4\text{mm}^3$ ($\approx 8.3\lambda_p\times8.3\lambda_p\times2.9\lambda_p$), with the thickness of the absorbing region equal to 2.4mm ($\approx 1.5\lambda$). The box is meshed using the mixed algorithm as introduced in Chapter 3 to combine the automatic and the regular meshing profiles with the tetrahedral elements. A cross section view of the 3D meshed FE domain is shown in Fig. 4.7(b). The element size is set to be 0.1mm ($\approx \lambda_p/16$), and hence the number of nodes for a typical 3D model is approximately 720 thousand. Again the time spent at each stage of the simulation is summarized in Table 4.1.

Monte Carlo simulations with multiple realizations are run in 3D in the same way as was deployed for the 2D models. The sample averaged scattering patterns within the x-z plane when $\theta_i = 0^o$ are shown in Fig. 4.8 for different roughnesses. Good agreement can be seen from -70^o to 70^o when $\sigma = \lambda_p/8$, $\lambda_p/6$, $\lambda_p/5$ and $\lambda_p/4$. However, the KA becomes inaccurate once σ increases to $\lambda_p/3$. Note that the errors between the KA and the FE are relatively higher than those from the corresponding 2D plots in Fig. 4.6. Again the mean absolute error and the corresponding standard deviation for each σ are plotted in Fig. 4.8(e).

4.5 Error analysis

4.5.1 Surface roughness

As discussed in Section. 4.2.2, the errors from the KA are not only from the 'local' tangential plane assumption (e. g. $kr_c\cos^3\theta_i \gg 1$), but also arise from 'global' effects, such as multiple scattering and shadowing due to the overall shape of the rough surface. These 'global' errors become larger as the roughness increases, which are not easy to quantify directly. In [28] the correlation length λ_0 is found to be a critical parameter including both the local and the global effects for acoustic waves. However, results were not shown when the roughness satisfies $\sigma \geq \lambda/10$ and $\lambda_0 \leq \lambda/2$ simultaneously, and for relatively small correlation lengths when $\lambda_0 \approx \lambda/4$. In this chapter a different surface parameter for elastic materials is proposed, as a

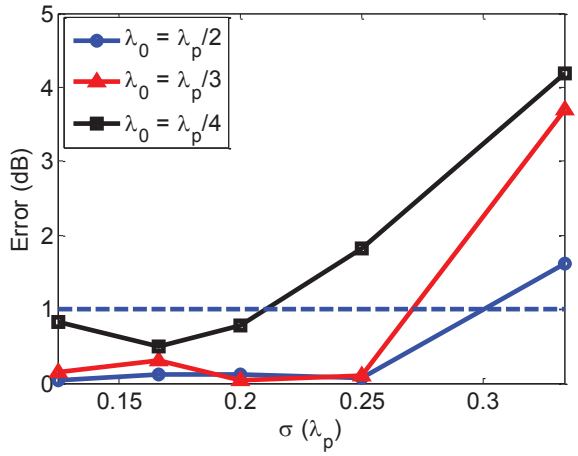

Figure 4.9: Error of the averaged peak amplitude ($\theta_i = \theta_s = 0^o$) between 2D FE and KA with respect to σ when $\lambda_0 = \lambda_p/2$, $\lambda_p/3$ and $\lambda_p/4$.

λ_0	$\lambda_p/2$	$\lambda_p/3$	$\lambda_p/4$
σ_{max2D}	$0.31\lambda_p$	$0.27\lambda_p$	$0.22\lambda_p$
σ_{max3D}	$0.27\lambda_p$	$0.22\lambda_p$	–

Table 4.2: Maximum values of σ for a known λ_0 with 1dB error of tolerance estimated from Fig. (4.9) (2D) and Fig. (4.12) (3D).

function of both λ_0 and σ to give an empirical principle when the use of the KA is valid. The generalized rule is offered as a practical guide, considering a larger range of roughness.

In Fig. 4.9 the data of errors of the averaged scattering amplitude between the 2D KA and the FE are plotted as a function of the RMS σ, when $\theta_s = \theta_i = 0^o$ for different correlation lengths. The flat dashed line at 1dB represents the commonly used tolerance of error in NDE applications. Hence the KA is defined as accurate as long as the corresponding error is below 1dB. According to the threshold one can estimate the maximum values of σ by observing the trend of error curves, which are summarized in Table 4.2.

Clearly, as can be seen from Fig. 4.9, increasing the RMS σ and decreasing the correlation length λ_0 result in a larger value of the error. This is because in this manner the radius of the curvature becomes smaller, which leads to larger errors due to the tangential plane assumption. In addition, more multiple scattering and

shadowing phenomena may occur. Hence a simple criterion expressed as a function of σ and λ_0 is proposed, based on the inverse proportionality relationship:

$$\frac{\sigma^a}{\lambda_0} \leq c \tag{4.5}$$

where a is the weighting factor for σ, and c is an unknown constant representing an upper bound for this inequality. Note that this form is not unique, for instance one may also assume a weighting factor for λ_0 instead of σ. However, in this chapter Eq. (4.5) is proposed and it will be shown that this formulation can approximately estimate the region of validity of the KA in both 2D and 3D.

The acceptable values of σ and λ_0 can be estimated from this formula once a and c are known. An alternative form converted from Eq. (4.5) is used here to calculate these two unknown coefficients:

$$\frac{\sigma_{\max}^a}{\lambda_0} = c \tag{4.6}$$

Substituting the values of $\sigma_{\max 2D}$ from Table 4.2 into Eq. (4.6) and taking the log of both sides yields the following form of matrix multiplication:

$$\begin{pmatrix} \log_{10}\sigma_{\max 1} & -1 \\ \log_{10}\sigma_{\max 2} & -1 \\ \log_{10}\sigma_{\max 3} & -1 \end{pmatrix} \begin{pmatrix} a \\ \log_{10} c \end{pmatrix} = \begin{pmatrix} \log_{10}\lambda_{01} \\ \log_{10}\lambda_{02} \\ \log_{10}\lambda_{03} \end{pmatrix} \tag{4.7}$$

By multiplying the term on the right-hand side with the pseudo inverse of the first term on the left side, the weighting factor a and the upper bound c are calculated in the sense of least squares. Recalling that the tolerance of 1dB is used, typical of NDE, from the calculation one can see that for this error $a \approx 2$. The value of a could change if a more or less stringent tolerance of error were required. The observed criterion for the validity of 2D KA can be expressed as:

$$\frac{\sigma^2}{\lambda_0} \leq 0.2\lambda_p \tag{4.8}$$

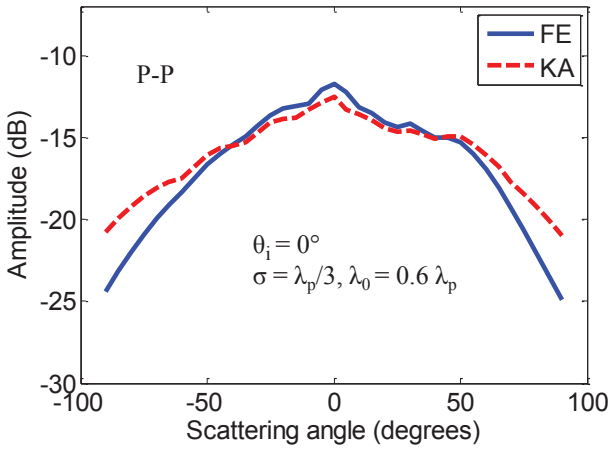

Figure 4.10: Comparison of the averaged peak amplitude of the scattering signals from 50 realizations ($\theta_i = 0^o$) between 2D FE and KA, when $\sigma = \lambda_p/3$, $\lambda_0 = 0.6\lambda_p$.

This criterion can be applied to find $\sigma_{\max}$ with a given λ_0 or the $\lambda_{0\min}$ with a given σ:

$$\sigma_{\max} = (0.2\lambda_p \times \lambda_0)^{\frac{1}{2}} \quad \text{and } \lambda_{0\min} = \frac{\sigma^2}{0.2\lambda_p} \tag{4.9}$$

In order to test the feasibility of the empirical criterion, numerical simulations with a chosen value of roughness are performed. From Fig. 4.9, one may notice that errors for all curves are larger than 1dB when $\sigma = \lambda_p/3$, which indicates that the acceptable λ_0 needs to be larger than $\lambda_p/2$. By substituting $\sigma = \lambda_p/3$ into Eq. (4.9), $\lambda_{0\min}$ is estimated to be roughly $0.6\lambda_p$. A Monte Carlo simulation with 50 surfaces is hence run for this specific σ and λ_0 to compare the KA and the FE. The error between the KA and the FE when $\theta_i = \theta_s = 0^o$ is 0.86dB, as observed from Fig. 4.10. This error is just below the 1dB threshold, implying that when $\sigma = \lambda_p/3$, $\lambda_{0\min} = 0.6\lambda_p$, which is the same as the value predicted from Eq. (4.9). Hence the simple empirical criterion proposed from observation can be applied to approximately estimate the region of validity of KA in terms of the surface roughness.

4.5.2 Scattering/incidence angle

At large scattering/incidence angles, it is well known that the KA is inaccurate to model the scattered waves [4]. For instance as noticed from Fig. 4.6(a) to (e), the

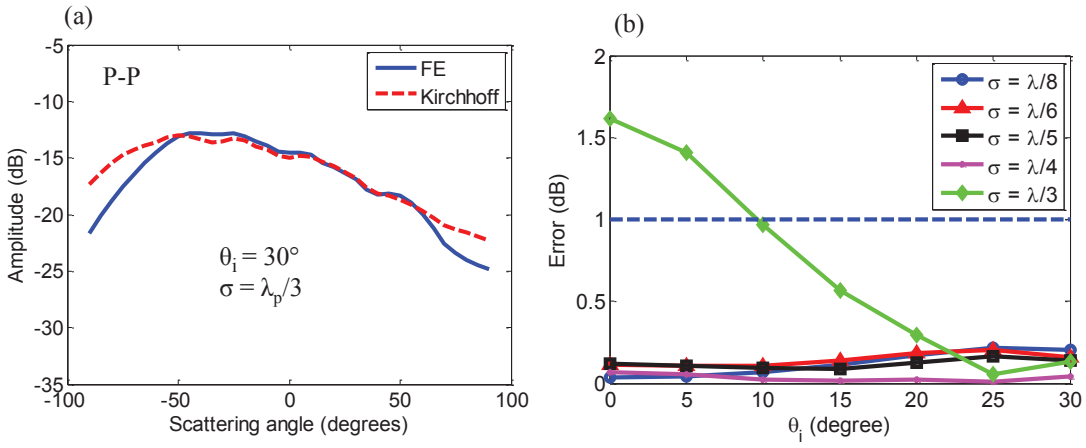

Figure 4.11: Effects of a modest incidence angle on the accuracy of KA in 2D. (a) Comparison of the averaged scattering amplitude from 50 realizations ($\theta_i = 30^o, -90^o \leq \theta_s \leq 90^o$) between 2D FE and KA when $\sigma = \lambda_p/3$, $\lambda_0 = \lambda_p/2$. (b) Error of the averaged peak amplitude between 2D FE and KA with respect to θ_i in the specular direction when $\sigma = \lambda_p/8$, $\lambda_p/6$, $\lambda_p/5$, $\lambda_p/4$, $\lambda_p/3$, and $\lambda_0 = \lambda_p/2$.

scattering amplitude calculated by the KA is several dB higher than that in the FE results when the scattering angle $\theta_s > 70^o$. The explanation given in section 4.4.1 is that the KA cannot account for multiple scattering effects.

A practical NDE inspection often seeks for inspection angles not larger than 45^o for improved detectability. Hence in this section, attention is drawn alternatively on the effect of modest incidence angles on the accuracy of the KA. This is equivalent to the illumination of a surface inclined with some modest angle. Specifically, the averaged scattering amplitude of the KA and the FE are compared, at incidence angles from 0^o to 30^o with an interval of 5^o.

The scattering patterns calculated using the KA and the FE are shown in Fig. 4.11(a) when $\theta_i = 30^o$ for one roughness ($\sigma = \lambda_p/3$, $\lambda_0 = \lambda_p/2$). An excellent agreement is found with the scattering angle θ_s ranging from -65^o to 65^o, especially at the specular angle. In contrast, with a normal incidence angle and the same roughness the error is above 1dB as shown in Fig. 4.6(e). Hence a modest incidence angle seems beneficial for the performance of the KA, for surfaces with a high roughness. To further illustrate this point, Fig. 4.11(b) shows the errors between KA and FE at the specular direction in terms of the incidence angle. The error decreases signif-

icantly as the incidence angle increases when $\sigma = \lambda_p/3$; for other curves when $\sigma < \lambda_p/3$, the error roughly remains the same, well within 1dB. The results for surfaces with a correlation length of $\lambda_p/2$ are shown here but the trend is typical for all other correlation lengths tested.

To explain the decay of the error, the 'Rayleigh parameter'[4] is quoted here as it is normally used to judge whether a surface is rough or relatively flat. The expression of the Rayleigh parameter is given here:

$$R_a = k\sigma \cos\theta_i \tag{4.10}$$

Physically, it represents the ensemble averaged relative phase difference of the waves scattered from two random surface points observed in the specular direction. The larger the value of R_a, the more destructively the two reflected waves interfere with each other, and hence the surface appears more rough to the incident wave. For example the two scattered waves will be completely cancelled if they have a phase difference of 180^o. According to Eq. (4.10), if the Rayleigh parameter R_a is fixed then the RMS σ is inversely a measure of $\cos\theta_i$. It suggests that for a fixed R_a, with a modest incidence angle the maximum value of σ can be relatively larger than that when $\theta_i = 0^o$. Therefore the accuracy of KA can be improved if the incidence angle is slightly oblique. Note that this finding cannot be applied in the same manner when the incidence angle is large.

4.5.3 Dimension (2D or 3D model)

In 3D, similar criteria for the KA can be found using the same methodology as in 2D. The errors between the KA and the FE are shown in Fig. 4.12 as a function of σ for different correlation lengths. Similar trends can be observed in the two curves but the errors are relatively higher, compared with those in Fig. 4.9 for the 2D KA. According to σ_{max3D} in Table 4.2, the unknown parameters in Eq. (4.5) can be estimated for 3D KA. Specifically, the values of σ_{max} for a given λ_0 in 3D are smaller than those in 2D as shown in Table 4.2; By using the least squares method, the best fitted weighting factor remains at $a \approx 2$, and the upper bound reduces to

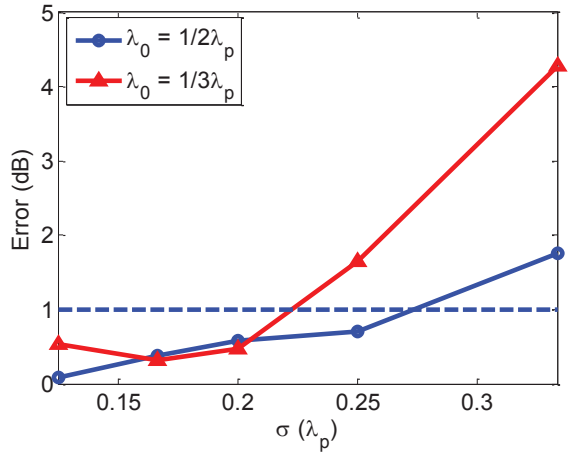

Figure 4.12: Error of the averaged scattering amplitude between 3D FE and KA ($\theta_i = \theta_s = 0^o$) with respect to σ when $\lambda_0 = \lambda_p/2$ and $\lambda_p/3$.

$c = 0.14\lambda_p$. The criterion in 3D can therefore be expressed as:

$$\frac{\sigma_{\max}^2}{\lambda_0} \leq 0.14\lambda_p \tag{4.11}$$

One may notice that the upper bound $0.14\lambda_p$ is smaller than the corresponding value $0.2\lambda_p$ in 2D, which highlights that the criterion for 3D KA is stricter than that in 2D. The physical reason is given here by considering both the local and the global errors.

Locally the magnitude of the gradient of one surface point in 2D and 3D can be expressed as

$$|\nabla h(x)|_{2\mathrm{D}} = \left|\frac{\partial h}{\partial x}\right|_{2\mathrm{D}} \quad \text{and,} \quad |\nabla h(x,y)|_{3\mathrm{D}} = \sqrt{\left|\frac{\partial h}{\partial x}\right|_{3\mathrm{D}}^2 + \left|\frac{\partial h}{\partial y}\right|_{3\mathrm{D}}^2}. \tag{4.12}$$

Obviously from the above equation, $|\nabla h(x,y)|_{3\mathrm{D}}$ is larger than $|\nabla h(x)|_{2\mathrm{D}}$ if it is assumed that $|\frac{\partial h}{\partial x}|_{2\mathrm{D}} = |\frac{\partial h}{\partial x}|_{3\mathrm{D}}$, which is due to adding an additional term $|\frac{\partial h}{\partial y}|_{3\mathrm{D}}$. The conclusion is that the rate of change of height is faster for the 2D surface which consequently appears more rough than the corresponding 1D surface.

In addition to the local effects, globally height variations in the y direction can contribute to out-of-plane scattering besides the scattered waves inside the x-z plane. More shadowing effects and multiple scattering would occur, which all lead to additional errors for the 3D KA. As a result, restrictions on the validity of 3D KA are

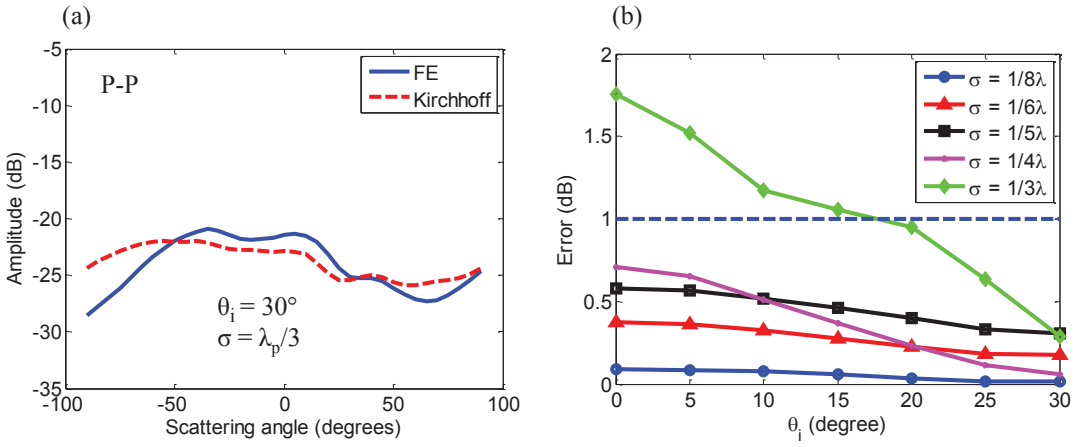

Figure 4.13: Effects of a modest incidence angle on the accuracy of KA in 3D. (a) Comparison of the averaged scattering amplitude from 50 realizations ($\theta_i = 30^o, -90^o \leq \theta_s \leq 90^o$) between 3D FE and KA when $\sigma = \lambda_p/3$, $\lambda_0 = \lambda_p/2$. (b) Error of the averaged peak amplitude between 3D FE and KA with respect to θ_i in the specular direction when $\sigma = \lambda_p/8$, $\lambda_p/6$, $\lambda_p/5$, $\lambda_p/4$, $\lambda_p/3$, and $\lambda_0 = \lambda_p/2$.

made more severe than the 2D KA due to one more dimension of roughness.

If the incidence angle is slightly oblique at 30^o as shown in Fig. 4.13(a), the FE and the KA models show agreement of the scattering pattern, but only within a very narrow angular range around the specular angle (30^o to 50^o). In contrast, the acceptable region of the scattering angles in 2D with the same roughness is much larger, ranging from -65^o to 65^o, as shown in Fig. 4.11(a). This rapidly reduced angular range in 3D when $\sigma = \lambda_p/3$ is another important feature of the assessment for the validity of 3D and 2D KA. It may be because in 3D there are more multiple scattering and mode conversions than 2D. The scattered waves contributed from these phenomena would spread to all scattering angles, reducing the accuracy of the 3D KA at non-specular directions. On the other hand, the effect of a modest incidence angle on the 3D KA is demonstrated in Fig. 4.13(b). All the curves representing different RMS show a decay of the error when increasing the incidence angle θ_i. The errors are relatively higher than those shown in Fig. 4.11(b) for the 2D cases.

4.6 Summary of findings

In this chapter, the numerical method developed in Chapter 3 is utilized to examine the validity of the elastodynamic KA from random rough surfaces. The Kirchhoff approximation is evaluated using 1D and 2D isotropic Gaussian surfaces with different roughnesses characterized by RMS σ and correlation length λ_0. Monte Carlo simulations of multiple realizations are run with a variety of incidence/scattering angles, and the averaged peaks of scattering signals are used for comparison. The conclusion is that, with a normal incidence angle $\theta_i = 0^o$, the KA is valid when $\sigma^2/\lambda_0 \leq c$, with -70^o $<\theta_s <$70^o. In addition, a modest incidence angle within 30^o can improve the accuracy of the KA, especially when σ^2/λ_0 exceeds the upper bound c. The above criteria are derived empirically for an estimation of the region of validity of the KA.

The difference of the valid region for 2D and 3D KA, corresponding to using 1D and 2D surfaces has been particularly examined and it has been found that the criterion for the 3D KA is stricter. First of all when $\theta_i = 0^o$, the upper bound c of σ^2/λ_0 in 2D is $0.20\lambda_p$, and in 3D it reduced to $0.14\lambda_p$. In other words, the acceptable range of σ and λ_0 in 3D is smaller than in 2D, which is the most important discrepancy between the 2D and 3D KA. This is caused by the increased local RMS gradient, and the global multiple reflections and shadowing effects as well. Furthermore, similar to 2D, a modest incidence angle of less than 30^o can also improve the accuracy of the 3D KA. However, the acceptable angular range of the scattering angle is dramatically reduced, being only around the specular angle, compared with the same situation in 2D.

These findings can be applied to judge when the use of the elastodynamic KA offers a reasonable result, given a candidate rough surface. In particular it highlights the importance to include 3D effects of the surface scattering, for practical purpose in a real NDT inspection.

Chapter 5

Elastodynamic Kirchhoff Theory for the Diffuse Field

5.1 Introduction

The Kirchhoff approximation is used in this chapter to develop an elastodynamic theory for predicting the diffuse field by randomly rough surfaces for the first time. Analytical expressions are derived incorporating surface statistics to represent the expected angular distribution of the diffuse intensity, which are then verified by Monte Carlo simulations and experiments. In a particular application, the theory is then utilized to analyze the effect of the roughness on the mode conversion and the depolarization caused by 2D roughness.

Elastic wave scattering from a rough surface of finite dimensions with arbitrary incidence/scattering angles is considered as shown in Fig. 5.1 and Fig. 5.2. The unit incident and scattering vectors are denoted in 2D as:

$$\begin{aligned} \hat{\boldsymbol{k}}_{\boldsymbol{in}} &= (\sin\theta_i, -\cos\theta_i) \\ \hat{\boldsymbol{k}}_{\boldsymbol{sc}} &= (\sin\theta_s, \cos\theta_s) \end{aligned} \tag{5.1}$$

and in 3D as:

$$\begin{aligned} \hat{\boldsymbol{k}}_{\boldsymbol{in}} &= (-\sin\theta_{iz}\cos\theta_{ix}, -\sin\theta_{iz}\sin\theta_{ix}, -\cos\theta_{iz}) \\ \hat{\boldsymbol{k}}_{\boldsymbol{sc}} &= (\sin\theta_{sz}\cos\theta_{sx}, \sin\theta_{sz}\sin\theta_{sx}, \cos\theta_{sz}) \end{aligned} \tag{5.2}$$

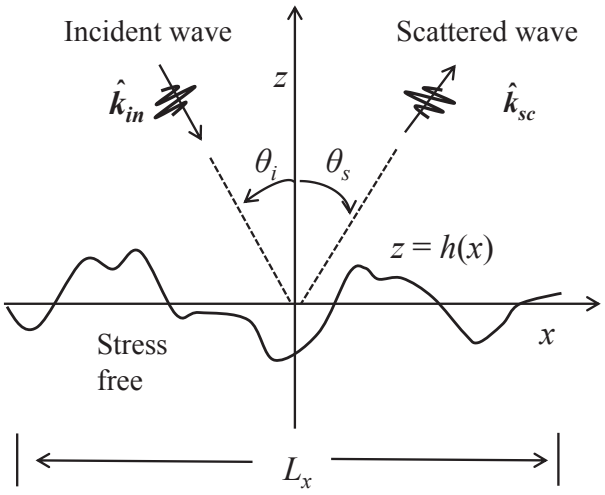

Figure 5.1: Sketch of a plane wave scattered from a 1D rough surface in a 2D model.

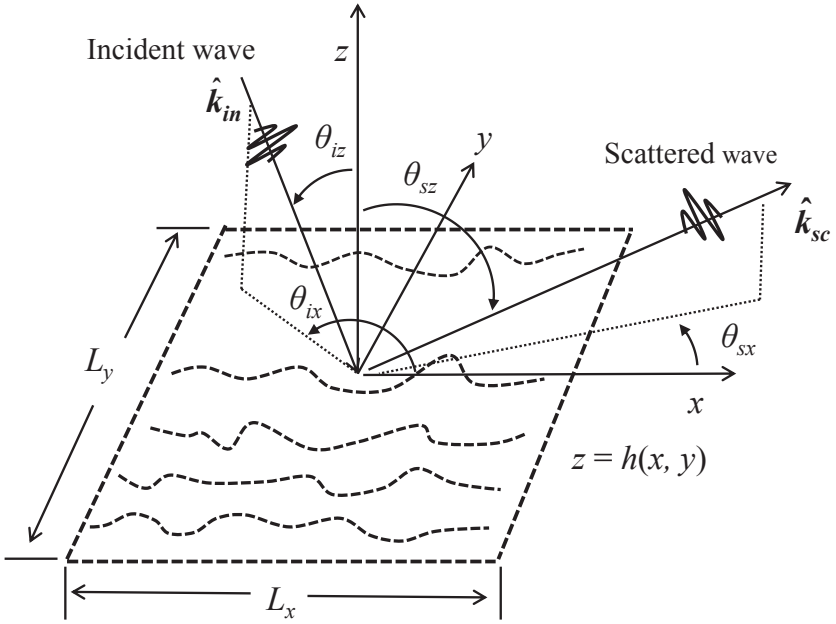

Figure 5.2: Sketch of a plane wave scattered from a 2D rough surface in a 3D model.

How surface roughness changes the expected scattering intensity and its angular distribution is a fundamental problem which remains open today. The application varies from boundary scattering of phonons for thermal transport relevant for terahertz elastic phonon devices [11, 63], ultrasound detection/imaging [2, 38] for NDE, to seismic wave exploration at infrasonic frequencies [26]. All of these problems share similar wave scattering theory mathematically (e. g. 2*nd*-order elastic wave equation) although with different scales of the wavelength.

Early works led by Ogilvy [9] have investigated the coherent scattering intensity at the specular angle:

$$I_c = I^{fs} \exp(-g_{\alpha\beta}), \alpha, \beta = p, s \tag{5.3}$$

in which I^{fs} is the response from a flat surface with the same dimension. In 2D the decay factor $g_{\alpha\beta} = (k_\alpha + k_\beta)^2 \cos\theta_i^2 \sigma^2$, where θ_i is the incidence angle and $k_{\alpha/\beta}$ represents the wavenumber for incident/scattered waves. Eq. (5.3) has resulted in a single expression for the reduction of the coherent intensity due to the increase of the surface RMS value σ. However, it is also known that this approach is very conservative for high roughness and non-specular angles [4, 9, 63], since the dominant diffuse field is not included in the equation. In practice it would be desirable, and valid, to obtain a value of the scattering that includes the contribution of the diffuse field, because in a single realization in a real setup (e. g. a single NDE measurement) it is not the coherent intensity that is measured but rather some addition of coherent and diffuse parts; this we can think of as the expected value of the scattering intensity [5]. Only a rough estimation of the elastodynamic diffuse intensity is given [4] due to lack of knowledge for a full calculation.

More recently, sophisticated numerical techniques have been adopted to study elastic waves scattered from randomly rough surfaces [5, 19, 23, 31, 64] with different applications in NDE. In [5], the diffuse field has been calculated with FE simulations using the Monte Carlo approach. However as is well known that numerical methods are computationally expensive, and it is not straightforward to find the connection between the surface statistics and the scattering field from purely numerical results. Analytical methods provide alternative ways to obtain simple mathematical expres-

sions for a rapid calculation of the intensity. More importantly they enable a direct incorporation of the statistical parameters of the surface into the formulae, so that the intrinsic relation between the roughness and the diffuse intensity can be revealed.

For example, the perturbation approach [65, 66] and the Kirchhoff approximation (KA) [8, 28, 67] have been extensively applied to study acoustic wave scattering. However, very few theoretical studies can be found for diffuse elastic wave scattering from randomly rough surfaces. One of the most recent works involves the perturbation analysis of elastic phonon scattering from a rough surface in a solid medium [11]. However, it is known that the perturbation approach is only valid for weakly rough surfaces, for instance $\sigma < \lambda/10$ if only considering the first-order approximation [66]. In the field of NDE and seismology, the typical RMS value has a much larger range approximately from $\lambda/20$ to $\lambda/3$ [9, 10, 38] where a perturbation method might not be reliable.

By contrast, the KA can handle scattering from surfaces with roughness up to $\sigma = \lambda/3$ according to the evaluation work in the previous chapter. At such a high roughness the scattering pattern is completely different from that for a weakly rough surface. For instance, the diffuse field is dominant and the scattering energy is more isotropically distributed. Such a theory using the Kirchhoff approximation can be found for acoustic waves [28, 32], by applying the Beckmann slope approximation derived from the integration by parts. But for decades the counterpart analytical expression has not yet been found for elastic waves, mainly restricted by the mode coupling at the rough boundary as mentioned by Ogilvy [4]. The local reflection coefficient/amplitude varies with respect to the surface gradient for elastic waves, so that one requires the two-point height-gradient average that are not generally known [9]. However, it is expected that the elastodynamic scattering is fundamentally different from that of acoustic waves mainly due to the mode conversion and the polarization, which are unique for elastic waves and also heavily rely on the roughness of the surface.

In this chapter, the problem is solved by deriving theoretical formulae to represent the elastic wave diffuse intensity with the KA for different modes. In addition, high frequency asymptotic solutions are found when the diffuse field is dominant. The

developed theory is numerically verified by comparison with Monte Carlo simulations, and also validated via experiments using phased arrays. A systematic physical analysis is provided for the effect of the roughness, elasticity on the mode conversion and the scattering intensity. The out-of-plane depolarization induced by the 2D roughness is also investigated for the first time.

5.2 Elastodynamic Kirchhoff theory

5.2.1 Slope approximations for different wave modes

The elastodynamic Helmholtz integral formula to calculate the scattering displacement with a stress-free boundary condition is [2]:

$$u_k^{sc}(\boldsymbol{R}) = \int_{\mathcal{S}} \Sigma_{ij;k}(|\boldsymbol{R}-\boldsymbol{r}|)u_i(\boldsymbol{r})n_j(\boldsymbol{r})d\mathcal{S}(\boldsymbol{r}) \tag{5.4}$$

where $\Sigma_{ij;k}$ is the stress Green's tensor, u_i is the ith component of the total displacement at the boundary point $\boldsymbol{r}$, n_j is the jth component of the unit normal vector surface pointing towards the observation point at $\boldsymbol{R}$. With the first order far field approximation that $|\boldsymbol{R}-\boldsymbol{r}| \approx R - \hat{\boldsymbol{R}}\cdot\boldsymbol{r}$, Eq. (5.4) can be simplified and converted into the integral along the mean plane of the surface:

$$\boldsymbol{u}^{sc}(\boldsymbol{R}) = -ik_\beta \frac{\exp(ik_\beta r)}{4\pi r}\int_{\mathcal{S}_m} \boldsymbol{U}_{\alpha\beta}\exp(ik_\beta\phi_{\alpha\beta})d\mathcal{S}_m, \alpha,\beta = p,s \tag{5.5}$$

where $\phi_{\alpha\beta} = A_{\alpha\beta}x + B_{\alpha\beta}y + C_{\alpha\beta}h(x,y)$, and

$$\begin{aligned} A_{\alpha\beta} &= \frac{k_\alpha}{k_\beta} sin\theta_{iz} cos\theta_{ix} - sin\theta_{sz} cos\theta_{sx} \\ B_{\alpha\beta} &= -\frac{k_\alpha}{k_\beta} sin\theta_{iz} sin\theta_{ix} - sin\theta_{sz} sin\theta_{sx} \\ C_{\alpha\beta} &= -\left(\frac{k_\alpha}{k_\beta} cos\theta_{iz} + cos\theta_{sz}\right) \end{aligned} \tag{5.6}$$

The term $\boldsymbol{U}_{\alpha\beta}$ represents the decomposed displacement for different wave modes

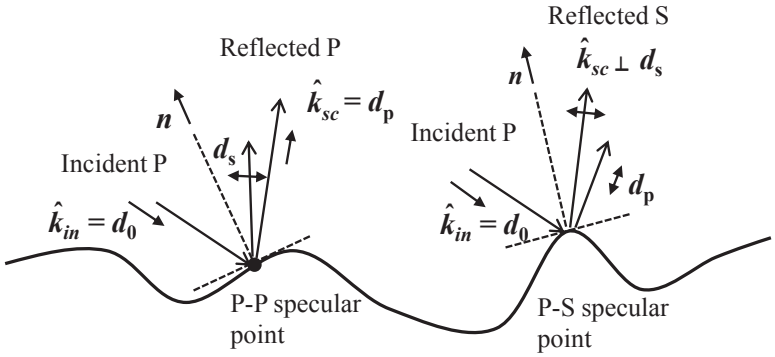

Figure 5.3: Sketch of the 'specular points' for P-P and P-S modes.

and can be expressed as:

$$\begin{aligned} \boldsymbol{U}_{\alpha p}(\boldsymbol{r}, \hat{\boldsymbol{k}}_{\boldsymbol{sc}}) &= \left[(\boldsymbol{u}_\alpha \cdot \boldsymbol{N})\left(1 - 2\gamma^2\right) + 2\gamma^2(\boldsymbol{u}_\alpha \cdot \hat{\boldsymbol{k}}_{\boldsymbol{sc}})(\boldsymbol{N} \cdot \hat{\boldsymbol{k}}_{\boldsymbol{sc}})\right]\hat{\boldsymbol{k}}_{\boldsymbol{sc}} \\ \boldsymbol{U}_{\alpha s}(\boldsymbol{r}, \hat{\boldsymbol{k}}_{\boldsymbol{sc}}) &= (\boldsymbol{N} \cdot \hat{\boldsymbol{k}}_{\boldsymbol{sc}})\boldsymbol{u}_\alpha + (\boldsymbol{u}_\alpha \cdot \hat{\boldsymbol{k}}_{\boldsymbol{sc}})\boldsymbol{N} - 2(\boldsymbol{u}_\alpha \cdot \hat{\boldsymbol{k}}_{\boldsymbol{sc}})(\boldsymbol{N} \cdot \hat{\boldsymbol{k}}_{\boldsymbol{sc}})\hat{\boldsymbol{k}}_{\boldsymbol{sc}} \end{aligned} \tag{5.7}$$

Note that $\boldsymbol{N}$ is the unnormalized vector, which equals to $(-\frac{\partial h}{\partial x}, -\frac{\partial h}{\partial y}, 1)$. The total boundary displacement $\boldsymbol{u}_\alpha$ can be obtained from the Kirchhoff approximation using Eq. (4.1) to Eq. (4.3) in Chapter 4.

By examining Eq. (4.1)—(4.3), and Eq. (5.7), it is immediately noticed that $\boldsymbol{U}_{\alpha\beta}$ is a function involving the incidence/scattering angles and surface slopes, which rely on the positions of the surface points. It is critical to remove the surface slopes from the integration Eq. (5.5), to enable the analytical manipulation of the ensemble averaging $< u_k^{sc} \bar{u}_k^{sc} >$. However the Beckmann integration by parts used for acoustic waves cannot be applied for elastic waves due to the complicated form of $\boldsymbol{U}_{\alpha\beta}$, which restricted previous studies for further derivation of the ensemble averaging [4].

Here instead we apply a stationary phase approach to Eq. (5.5) to approximate $\boldsymbol{U}_{\alpha\beta}$. In this way, the first order derivative of the phase term $\phi_{\alpha\beta}$ with respect to x and y are both set to be zero to locate the stationary points, and the following expressions are obtained:

$$\frac{\partial h}{\partial x} = -\frac{A_{\alpha\beta}}{C_{\alpha\beta}}, \frac{\partial h}{\partial y} = -\frac{B_{\alpha\beta}}{C_{\alpha\beta}} \tag{5.8}$$

Physically Eq. (5.8) indicates that the slope across the whole surface is approximated as a constant for given incidence/scattering angles and the ratio of the shear-to-compressional wave speed. One may notice that the approximated slope actually corresponds to those surface points, where the scattering direction is locally viewed to be the same as the specular direction to the incidence angle with respect to the local normal vector $\boldsymbol{n}$. They are called the 'specular points' originated from the optical Kirchhoff theory [68], and the elastodynamic 'specular points' are depicted in Fig. 5.3 for both P-P and P-S modes. The P-P 'specular points' are located where the scattering direction coincides with the P wave polarization vector ($\hat{\boldsymbol{k}}_{\boldsymbol{sc}} = \boldsymbol{d}_{\boldsymbol{p}}$), while the P-S 'specular points' are those where the scattering direction is perpendicular to the S wave polarization vector ($\hat{\boldsymbol{k}}_{\boldsymbol{sc}} \perp \boldsymbol{d}_{\boldsymbol{s}}$). The principal contribution to the integral Eq. (5.5) is hence made at these 'specular points' corresponding to the stationary points.

By substituting the slope approximation in Eq. (5.8) into Eq. (4.1)—(4.3), and Eq. (5.7), the decomposed $\boldsymbol{U}_{\alpha\beta}$ at the 'specular points' can be obtained. For comparison with the acoustic and electromagnetic waves [32], here it is assumed that $\boldsymbol{F}_{\alpha\beta}$= $1/2\boldsymbol{U}_{\alpha\beta}$. By eliminating the dependence of surface gradient, $\boldsymbol{F}_{\alpha\beta}$ can now be removed from the Kirchhoff integral, and Eq. (5.5) is simplified as:

$$\boldsymbol{u}^{sc}(\boldsymbol{R}) = -ik_\beta \frac{\exp(ik_\beta r)}{4\pi r} 2\boldsymbol{F}_{\boldsymbol{\alpha\beta}} \int_{\mathcal{S}} \exp(ik_\beta \phi_{\alpha\beta}) d\mathcal{S} \tag{5.9}$$

where $\boldsymbol{F}_{\alpha\beta}$ is called the elastodynamic angular factor hereinafter, only depending on the incidence/scattering angles and the modes. Note that $\boldsymbol{F}_{\alpha\beta}$ is a vector containing three components due to the polarization of the displacement. Now only terms related with the surface height h are left inside the Kirchhoff integral, and hence the ensemble averaging $< u_k^{sc} \bar{u}_k^{sc} >$ can be performed analytically.

5.2.2 Ensemble averaging

The mathematical derivation of the ensemble averaging for elastic waves follows the acoustic case [4]. For simplicity the scattering intensity in this chapter is defined as

the modulus of the displacement:

$$\begin{aligned} &< I_i >=< u_i^{sc}\bar{u}_i^{sc} >, \quad \text{i = x, y, z} \\ &< I >= \sum_{x,y,z} < I_i >, \end{aligned} \tag{5.10}$$

The expected scattering intensity in 3D can be expressed as:

$$\begin{aligned} < I_{i,\alpha\beta} > &= \frac{k_\beta^2}{(4\pi r)^2} 4F_{i,\alpha\beta}^2 \int_{\mathcal{S}} \int_{\mathcal{S}} e^{ik_\beta[A_{\alpha\beta}(x_0-x_1)+B_{\alpha\beta}(y_0-y_1)]} \\ &\times < e^{ik_\beta C_{\alpha\beta}(h_0-h_1)} > dx_0 dx_1 dy_0 dy_1 \end{aligned} \tag{5.11}$$

By assuming that $\Delta x = x_0 - x_1$ and $\Delta y = y_0 - y_1$, Eq. (5.11) can be simplified via a change of variables:

$$\begin{aligned} < I_{i,\alpha\beta} > &= \frac{k_\beta^2}{(4\pi r)^2} 4F_{i,\alpha\beta}^2 L_x L_y \int_{-\infty}^{\infty} \int_{-\infty}^{\infty} e^{ik_\beta(A_{\alpha\beta}\Delta x+B_{\alpha\beta}\Delta y)} \\ &\times \chi_2(k_\beta C_{\alpha\beta}, -k_\beta C_{\alpha\beta}, \Delta x, \Delta y) d\Delta x d\Delta y \end{aligned} \tag{5.12}$$

where $\chi_2(k_\beta C_{\alpha\beta}, -k_\beta C_{\alpha\beta}, \Delta x, \Delta y) = < \exp[ik_\beta C_{\alpha\beta}(h_0 - h_1)] >$, which is the two-dimensional characteristic function as defined in Eq. (2.8). The dimension of the surface is $L_x \times L_y$. For a surface following a Gaussian distribution, χ_2 has an analytical form:

$$\chi_2(k_\beta C_{\alpha\beta}, -k_\beta C_{\alpha\beta}, \Delta x, \Delta y) = \exp(-g_{\alpha\beta}[1 - C(\Delta x, \Delta y)]) \tag{5.13}$$

Where $g_{\alpha\beta} = k_\beta^2 C_{\alpha\beta}^2 \sigma^2$. There is no requirement for a specific form of the correlation function $C(\Delta x, \Delta y)$, except that physically it needs to satisfy the following criteria: (1) C(0,0) = 1; and (2) C($\Delta x \to \infty$ or $\Delta y \to \infty$) = 0. Eq. (5.13) can be expanded as a Taylor series and substituted into Eq. (5.12) to obtain the following expression:

$$\begin{aligned} < I_{i,\alpha\beta} > &= \frac{k_\beta^2 F_{i,\alpha\beta}^2 e^{-g_{\alpha\beta}}}{4\pi^2 r^2} L_x L_y \Sigma_{n=0}^{\infty} \frac{g_{\alpha\beta}^n}{n!} \int_{-\infty}^{\infty} \int_{-\infty}^{\infty} e^{ik_\beta(A_{\alpha\beta}\Delta x+B_{\alpha\beta}\Delta y)} \\ &\times C^n(\Delta x, \Delta y) d\Delta x d\Delta y \end{aligned} \tag{5.14}$$

Substituting the Gaussian correlation function Eq. (2.9) into Eq. (5.14) yields a separation of the total intensity into the coherent and the diffuse parts:

$$
\begin{aligned}
&< I_{i,\alpha\beta} >= I^c_{i,\alpha\beta} + I^d_{i,\alpha\beta} \\
&I^c_{i,\alpha\beta} = I^{fs}_{i,\alpha\beta} e^{-g_{\alpha\beta}}, && \text{coherent} \\
&I^d_{i,\alpha\beta} = \frac{k_\beta^2 F^2_{i,\alpha\beta} \lambda_x \lambda_y e^{-g_{\alpha\beta}}}{4\pi r^2} L_x L_y \Sigma_{n=1}^{\infty} \frac{g^n_{\alpha\beta}}{n! n} \exp\left[-\frac{k_\beta^2 (A^2_{\alpha\beta}\lambda_x^2 + B^2_{\alpha\beta}\lambda_y^2))}{4n} \right] && \text{diffuse}
\end{aligned}
\tag{5.15}
$$

In 2D the coherent intensity has the same form as that in 3D, but the diffuse intensity needs to be revised as:

$$
< I^d_{i,\alpha\beta} >= \frac{k_\beta F^2_{i,\alpha\beta} \lambda_x \sqrt{\pi} e^{-g_{\alpha\beta}}}{2\pi r} L_x \Sigma_{n=1}^{\infty} \frac{g^n_{\alpha\beta}}{n! \sqrt{n}} \exp\left[-\frac{k_\beta^2 A^2_{\alpha\beta} \lambda_x^2}{4n} \right] \tag{5.16}
$$

By examining Eq. (5.15) and Eq. (5.16), the mode coupling for the diffuse field is embedded in the angular factor $F_{i,\alpha\beta}$, the decay factor $g_{\alpha\beta}$, and the exponential term inside the finite summation.

5.2.3 Asymptotic solutions

The diffuse field is dominant when the roughness or the frequency is high. By passing the Kirchhoff integral to the high frequency limit that $k_\beta C_{\alpha\beta}(h_0 - h_1) \approx k_\beta C_{\alpha\beta}(\frac{\partial h}{\partial x}\Delta x + \frac{\partial h}{\partial y}\Delta y)$ when $k \to \infty$, the diffuse field can be approximated as:

$$
\begin{aligned}
< I_{i,\alpha\beta} > &= \frac{k_\beta^2 F^2_{i,\alpha\beta}}{4\pi^2 r^2} L_x L_y \int_{-\infty}^{\infty}\int_{-\infty}^{\infty} < e^{ik_\beta[(A_{\alpha\beta}+C_{\alpha\beta}\frac{\partial h}{\partial x})\Delta x + (B_{\alpha\beta}+C_{\alpha\beta}\frac{\partial h}{\partial y})\Delta y]} > d\Delta x d\Delta y \\
&= \frac{k_\beta^2 F^2_{i,\alpha\beta}}{4\pi^2 r^2} L_x L_y \times \frac{(2\pi)^2}{k_\beta^2 C^2_{\alpha\beta}} < \delta(\frac{\partial h}{\partial x} + \frac{A_{\alpha\beta}}{C_{\alpha\beta}}, \frac{\partial h}{\partial y} + \frac{B_{\alpha\beta}}{C_{\alpha\beta}}) > \\
&= \frac{F^2_{i,\alpha\beta}}{r^2 C^2_{\alpha\beta}} L_x L_y \int_{-\infty}^{\infty}\int_{-\infty}^{\infty} p_g(\gamma_x, \gamma_y) d\gamma_x d\gamma_y \delta(\gamma_x + \frac{A_{\alpha\beta}}{C_{\alpha\beta}}, \gamma_y + \frac{B_{\alpha\beta}}{C_{\alpha\beta}}) \\
&= \frac{F^2_{i,\alpha\beta}}{r^2 C^2_{\alpha\beta}} L_x L_y \times p_g(\frac{\partial h}{\partial x} = -\frac{A_{\alpha\beta}}{C_{\alpha\beta}}, \frac{\partial h}{\partial y} = -\frac{B_{\alpha\beta}}{C_{\alpha\beta}})
\end{aligned}
\tag{5.17}
$$

In 2D, a similar equation can be expressed as:

$$< I_{i,\alpha\beta} >= \frac{F_{i,\alpha\beta}^2}{rC_{\alpha\beta}} L_x \times p_g(\frac{\partial h}{\partial x} = -\frac{A_{\alpha\beta}}{C_{\alpha\beta}}) \tag{5.18}$$

where p_g is the distribution for the surface slopes shown in Eq. (2.13). As can be seen, in the high frequency limit the scattering intensity is proportional to the angular factor and the pdf of the surface slopes only at the 'specular points'. Contributions from 'non-specular points' vanish rapidly due to fast oscillation of the phase, and hence have almost no effects on the Kirchhoff integral. The total intensity is equivalent to the dominant diffuse intensity. In contrast, when the roughness is small a low frequency approximation can be obtained from Eq. (5.15) in 3D or Eq. (5.16) in 2D by only keeping the first few terms. The number of terms for the convergence depends on both the RMS and the correlation length. Generally it is found that keeping the first four terms is sufficient for the convergence when $\sigma \leq \lambda_p/8$. Note that the high frequency asymptotic solution does not require any restriction on the pdf of the height or the height gradient.

5.3 Monte Carlo verification

5.3.1 Simulation parameters

In this section, Monte Carlo simulations are run using Gaussian surfaces from low to high roughness to assess the accuracy of the developed elastodynamic theory. For each realization of the surface profile, the Kirchhoff integral in Eq. (5.4) is evaluated numerically without the stationary phase approximation, and the mean total intensity is obtained as the sample averaging of intensities from 500 realizations of surfaces for each roughness. A more accurate way is to apply a purely numerical method described in Chapter 3 instead of the Kirchhoff model as a benchmark. However, the validity of the Kirchhoff approximation has been carefully evaluated by comparison with the numerical method in both 2D and 3D in Chapter 3. Hence for the roughness values considered here ($\sigma \leq \lambda_p/3, \lambda_x \geq \lambda_p/2$), the choice of either method would lead to the same conclusion since the KA is within the valid region. The bulk medium is chosen to be Aluminium with Young's modulus of 70GPa, density of 2700kg/m^3 and Poisson's ratio of 0.33. The S-to-P wave speed ratio γ is

therefore approximately 0.5 with $c_p = 6198$m/s, and $c_s = 3122$m/s. The incident wave on the surface is assumed to be a 4MHz monochromatic plane P wave, and the corresponding wavelengths for P and S modes are 1.54mm and 0.77mm.

5.3.2 2D scattering pattern

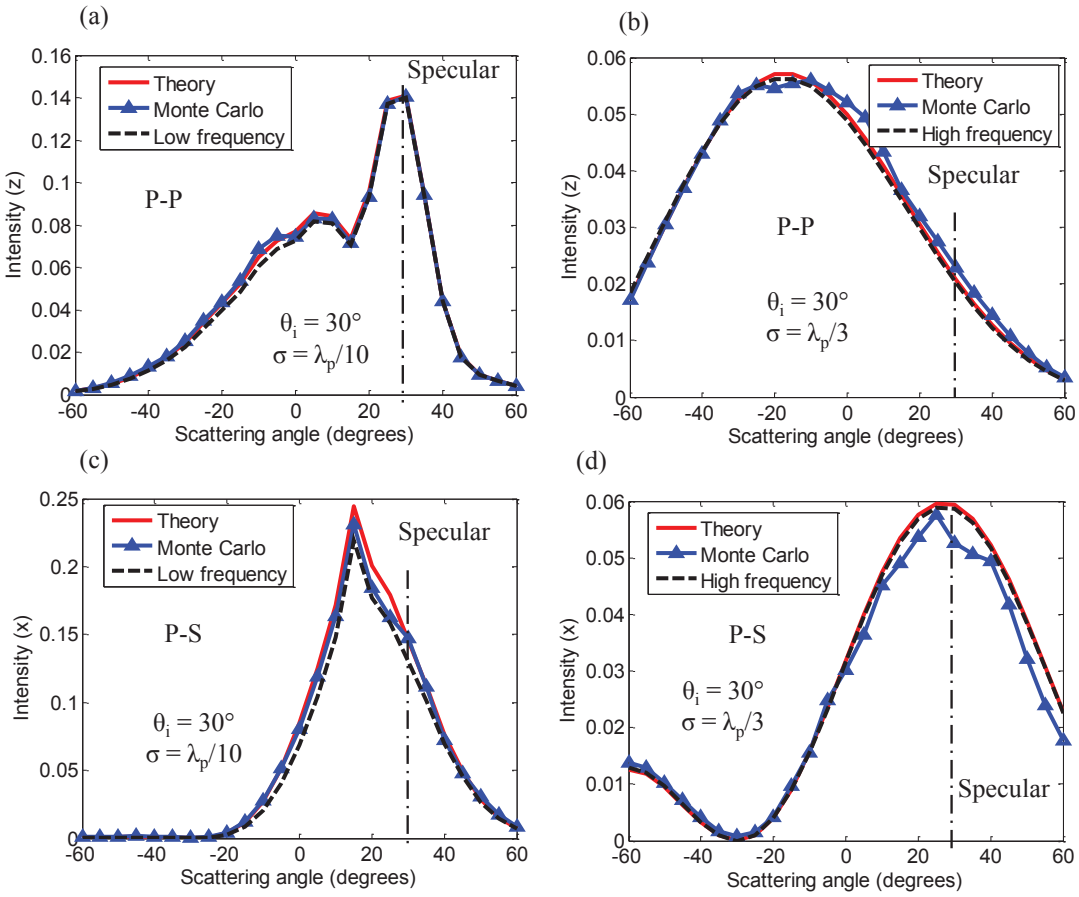

Figure 5.4: 2D scattering patterns obtained from the elastodynamic theory, Monte Carlo simulations and high/low frequency solutions, with an oblique incidence angle of 30^o. (a) P-P mode, $\sigma = \lambda_p/10$, $\lambda_x = \lambda_p/2$. (b) P-P mode, $\sigma = \lambda_p/3$, $\lambda_x = \lambda_p/2$. (c) P-S mode, $\sigma = \lambda_p/10$, $\lambda_x = \lambda_p/2$. (d) P-S mode, $\sigma = \lambda_p/3$, $\lambda_x = \lambda_p/2$.

In 2D the length of the 1D surface is 6mm ($\approx 4\lambda_p$) and the roughness parameters are $\sigma = \lambda_p/10$ to $\lambda_p/3$, and $\lambda_x = \lambda/2$. A modest incidence angle θ_i of 30^o is assumed when the mode conversion is strong. Fig. 5.4 shows the comparison of the expected scattering pattern for different modes predicted from the analytical Kirchhoff formulae and the benchmark Monte Carlo simulations. The high frequency asymptotic solution calculated from Eq. (5.18), and the low frequency approximation from Eq.

(5.15) and (5.16) with the first four terms are both plotted as well. The low and high frequency solutions actually correspond to low and high roughnesses, as the roughness is defined in terms of the wavelength. The quantities for comparison are $< I_{z,pp} >$ for the P-P mode and $< I_{x,ps} >$ for the P-S mode, defined in Eq. (5.10) as the z- and x- components of the scattering intensity. The values of the intensities have been normalized by the normal pulse echo response for the P-P mode from a flat surface with the same dimension. As can be seen, the theoretical results show excellent agreement with the numerical results from Monte Carlo simulations, and the agreement is found from low ($\sigma = \lambda_p/10$) to high roughness ($\sigma = \lambda_p/3$). In addition, the low and high frequency solutions are both very accurate as well.

It is noticeable that in Fig. 5.4(a), there is a sharp peak at the specular direction (θ_s = 30^o) for the P-P mode, contributed from the dominant coherent components. As the roughness increases to $\sigma = \lambda_p/3$, a clear peak is observed around the backward angle instead (θ_s = -30^o) in Fig. 5.4(b). Note that the backscattering peak is not as concentrated as the specular peak shown in Fig. 5.4(a) because it is formed by the dominant diffuse field, whose energy is more widely distributed. Furthermore, as noticed in Fig. 5.4(d), at high roughness the scattered S waves show a dipole-like pattern, with the peak located around the specular angle and the valley at the backward angle. A detailed physical analysis regarding the mode conversion is provided in the last section of this chapter.

5.3.3 3D scattering pattern

The elastodynamic theory is also evaluated on 2D Gaussian surfaces in 3D with the same bulk medium as the 2D models. The surface has a dimension of 6×6 mm^2 ($\approx 4\lambda_p \times \lambda_p$), with $\sigma = \lambda_p/10$ to $\lambda_p/4$, and $\lambda_x = \lambda_y = \lambda_p/2$. The incident P wave is within the x-z plane with a fixed incidence angle of 30^o ($\theta_{ix} = 180^o$, $\theta_{iz} = 30^o$). By changing θ_{sx} from 0^o to 360^o and θ_{sz} from 0^o to 60^o, the entire 3D scattering pattern can be obtained.

Fig. 5.5 and 5.6 show the comparison of the scattering patterns between the elastodynamic theory (first row), and the sample mean from the Monte Carlo simulations

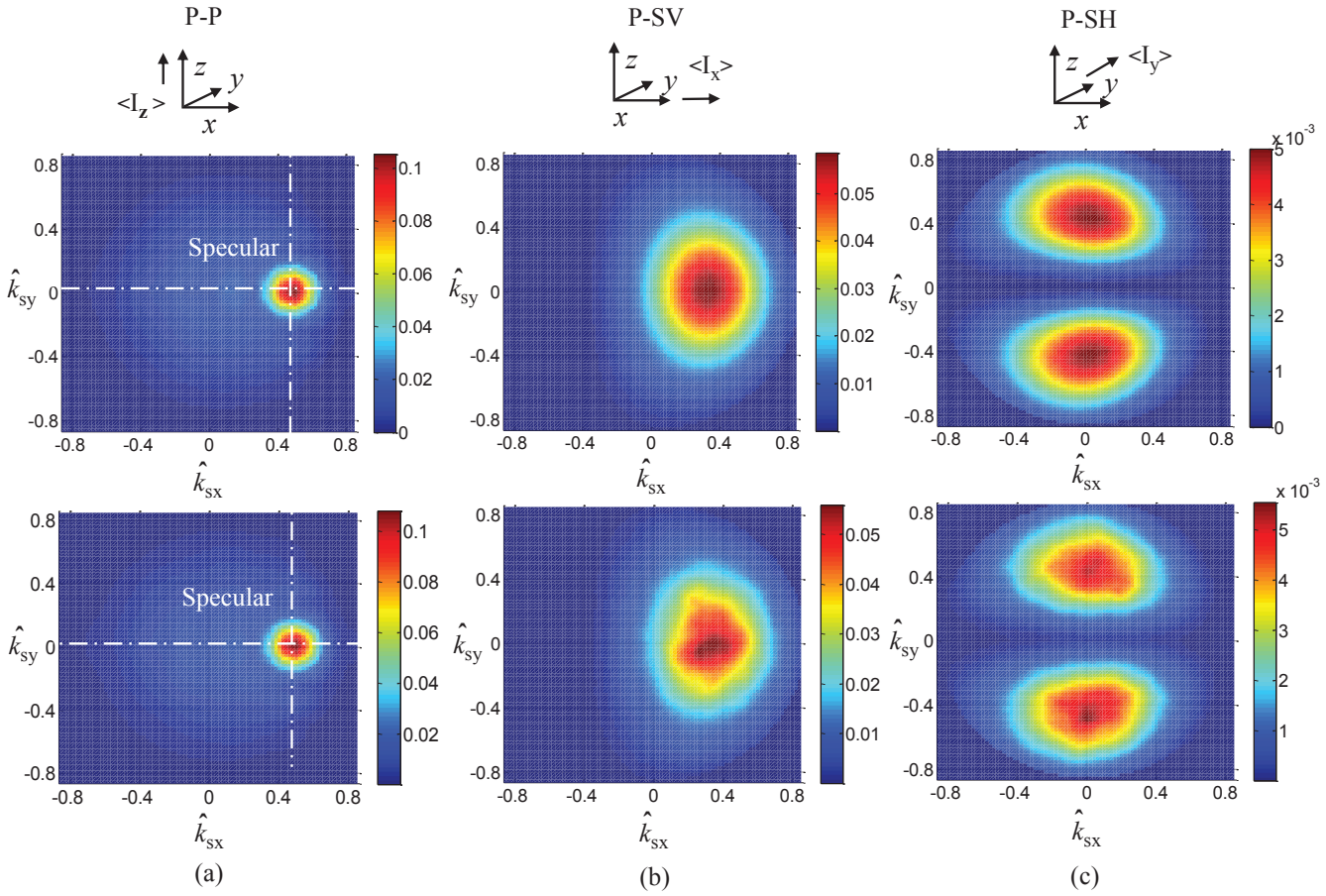

Figure 5.5: 3D scattering patterns obtained from the elastodynamic theory and the Monte Carlo simulations when $\sigma = \lambda_p/10$ and $\lambda_x = \lambda_y = \lambda_p/2$, with a modest incidence angle ($\theta_{iz} = 30^o, \theta_{ix} = 180^o$). (a) P-P mode. (b) P-SV mode. (c) P-SH mode. (Plots in the first row represent the ensemble average from the theory; Plots in the second row represent the sample average from Monte Carlo simulations)

(second row) for different wave modes, from low to high roughness. The scattering patterns are plotted as a function of the unit scattering vectors $\hat{k}_{sx}$ and $\hat{k}_{sy}$. It is equivalent to an angular projection of the scattering field into the x-y plane viewed from the z direction. The pixels represent the value of the scattering intensity, which are again normalized by that of a normal pulse echo response with the P-P mode from a flat 3D surface of the same dimension. Three intensities are shown here, with $< I_{z,p-p} >, < I_{x,p-sv} >$ and $< I_{y,p-sh} >$ plotted for P-P, P-SV and P-SH mode, respectively. Good agreement between the theory and the Monte Carlo simulations can be seen for all modes from low to high roughness.

The coherent peaks can be found around the specular directions for both P-P and

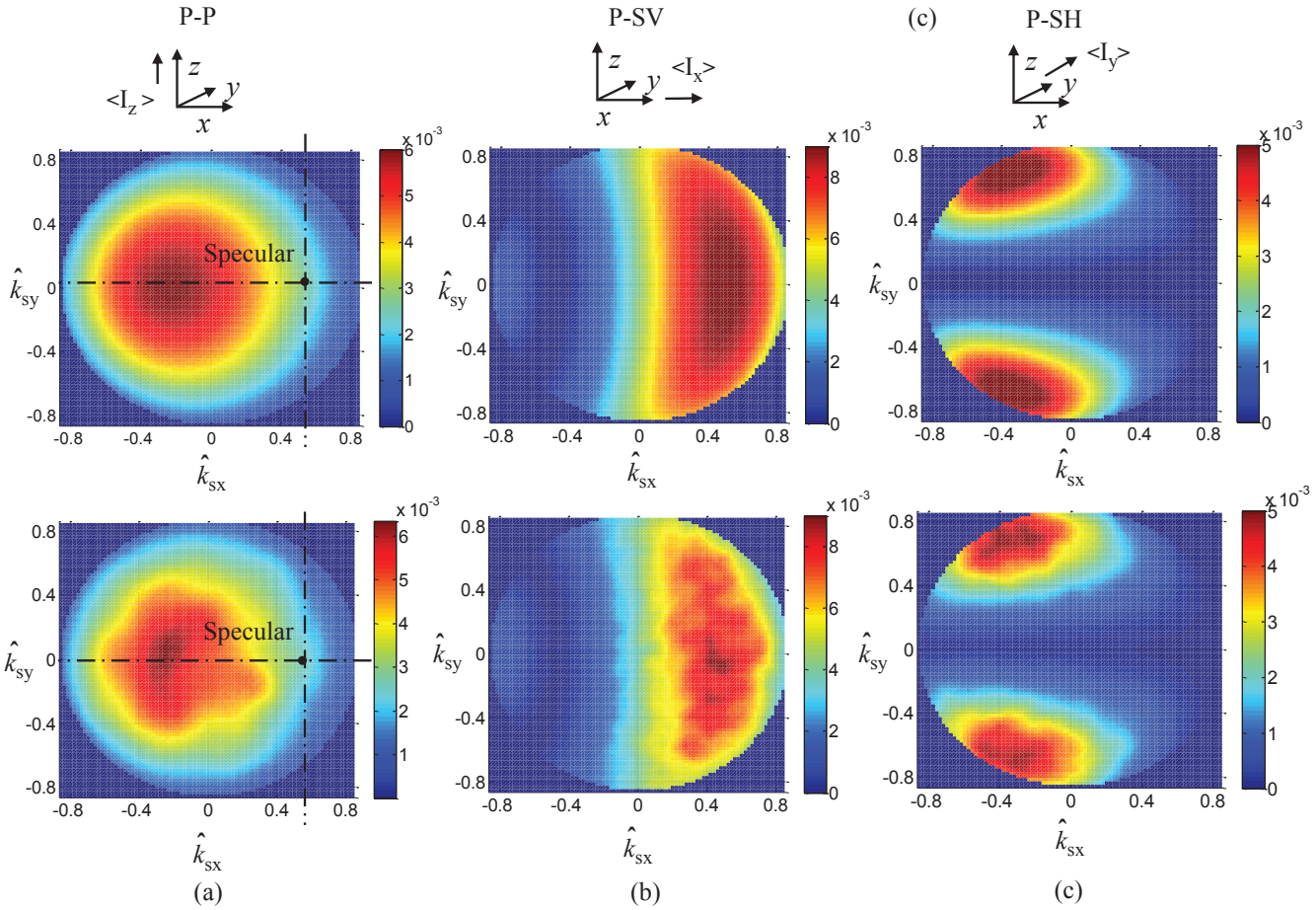

Figure 5.6: 3D scattering pattern obtained from the elastic theory and the Monte Carlo simulations when $\sigma = \lambda_p/4$ and $\lambda_x = \lambda_y = \lambda_p/2$, with a modest incidence angle ($\theta_{iz} = 30^o, \theta_{ix} = 180^o$). (a) P-P mode. (b) P-SV mode. (c) P-SH mode. (Plots in the first row represent the ensemble average from the theory; Plots in the second row represent the sample average from Monte Carlo simulations)

P-SV modes in Fig. 5.5(a) and (b). When the roughness increases, a more widely spread peak towards the backscattering angle is seen for the P-P mode in Fig. 5.6(a), due to the diffuse field and the mode conversion similar with the 2D plots shown in Fig. 5.4. Furthermore, the scattering pattern for the SH mode is symmetric about the plane of the incidence for both low and high roughness as noticed in Fig. 5.5(c) and Fig. 5.6(c), which is mainly due to the isotropic nature of the surface.

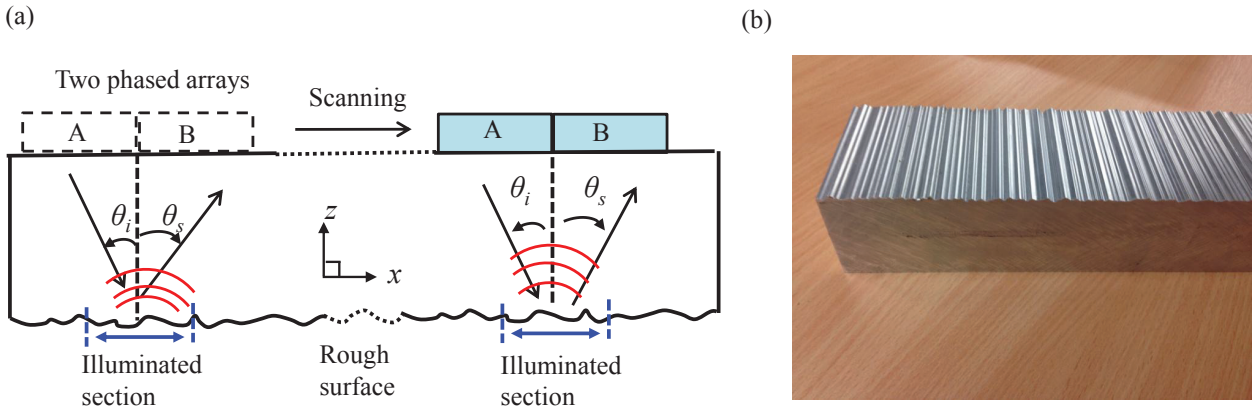

Figure 5.7: Experimental setup. (a) Illustration of the experimental methodology. (b) Picture of the sample (Length: 260mm; Width: 80mm; Height: 60mm).

5.4 Experimental validation

5.4.1 Experiment setup

To yet further validate the elastodynamic theory an experiment with two ultrasonic phased arrays is performed, which is illustrated in Fig. 5.7(a). The rough surface is manufactured on the bottom of an Aluminum block ($260\times80\times60\text{mm}^3$), and it is corrugated so that the height remains invariant in the y- direction shown in Fig. 5.7(b). The surface is made by a CNC (computer numerical control) milling machine using a drilling cutter, and follows a profile generated by a Gaussian distribution of heights. Two 2D linear phased arrays both with 32 elements are placed tightly together on the top flat surface of the sample. The parameters of the phased array are given in Table 5.1. In practice, elements numbered from 7 to 14 of array A are fired to produce the P wave beam with an incidence angle of 30^o using a time delay law. And in total all the 64 elements are used for receiving the scattered waves, corresponding to different scattering angles. The input signal is assumed to be a five-cycle tone burst with a centre frequency of 2MHz, and hence the P wavelength is 3.1mm. The RMS and the correlation length of the corrugated surface are 0.75mm ($\lambda_p/4$) and 1.54mm ($\lambda_p/2$) respectively. Note that the minimum dimension of the drilling cutter is 2mm, which might somewhat reduce the accuracy of the manufactured shapes of some 'peaks' and 'valleys' of the surface. However, this would not affect the main conclusion which will be shown later.

$Parameters\,of\,the\,ultrasonic\,phased\,array$	
$Number\,of\,elements\,per\,array$	32
$Element\,width$	$20mm$
$Inter\,element\,pitch$	$1.6mm$
$Inter\,element\,space$	$0.25mm$
$Centre\,frequency$	$2MHz$
$Bandwidth(-6dB)$	$1.3MHz$

Table 5.1: Parameters of the ultrasonic phased array

To acquire multiple realizations of the illuminated surfaces, the phased arrays are moved, or scanned across the top flat surface with a spatial interval of 8mm. In this manner, scattering from 16 different surfaces with the same statistics can be obtained, and the displacements (u_z) are recorded in each scan. By transferring the received signals into the frequency domain and extracting the amplitude at the centre frequency, the scattering amplitude and hence the intensity can be obtained for each realization/scan. The expected value of the scattering intensity is approximated by an arithmetic average from all scans.

5.4.2 Numerical simulation of the experiment

The experiment is first numerically simulated using a full FE model with Abaqus. The purpose of the numerical simulation is to test the feasibility of the experimental methodology and gain more confidence before conducting the real experiment. The FE simulation is performed in 2D as the surface height is invariant in the y-direction. Fig. 5.8 shows the animation for waves scattered from the sample surface for one scan. The FE model has a dimension of 259×66mm^2 ($\approx 168\lambda_p \times 43\lambda_p$), including the absorbing region with a thickness of 4.5mm ($\approx 3\lambda_p$) [47]. According to the parameters of the phased array, the lengths of the source line and the receiving line are 12.75mm ($\approx 8\lambda_p$) and 113mm ($\approx 73\lambda_p$), respectively. The scanning with phased arrays is simulated by selecting different nodes representing the source and the receiving line. After running multiple FE simulations, the scattered P waves can be simply separated from the S waves from the received waveforms using a time window. As can be seen in Fig. 5.7(a), the propagation distances r of the scattered waves from the illuminated surface to array elements vary, corresponding to different

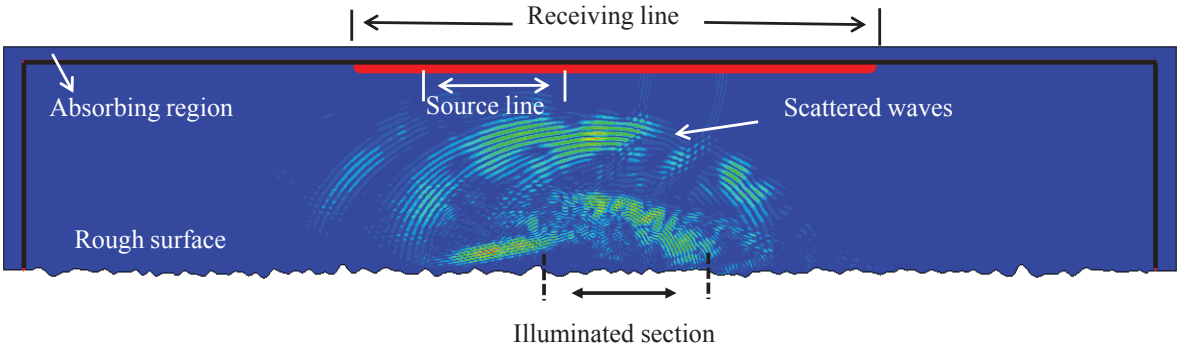

Figure 5.8: Snapshot of animation showing the waves scattered from the sample corrugated rough surface.

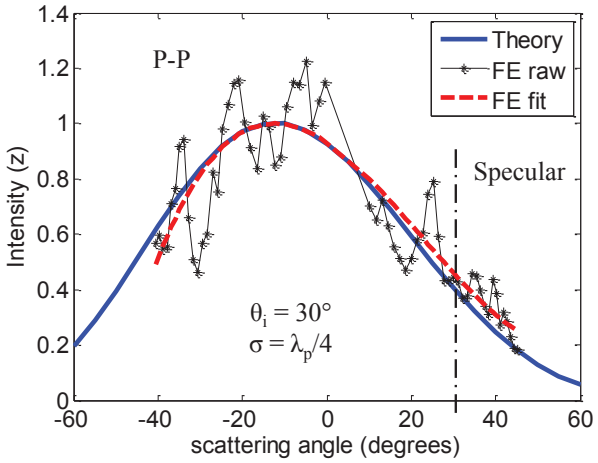

Figure 5.9: Comparison of the scattering pattern between the theory and the simulation (The FE fit curve is obtained from a 3rd-order polynomial fit of the FE raw data).

spatial decay factors $1/\sqrt{r}$ in 2D. To account for this spatial attenuation, the obtained scattering intensity at each angle needs to be normalized by a factor of $\cos\theta_s$.

The sample averaged scattering intensity from 16 scans using the FE simulation is plotted in Fig. 5.9, in comparison with that predicted from the elastodynamic theory. As can be found, the FE results match the shape of the theoretical curve. A peak can be seen when the scattering angle is around -20^o due to the dominant diffuse field at such a high roughness. The variations of the FE raw data are caused by the limited number of realizations used for averaging in the simulation. The variation or the spread of the intensity can be predicted from Monte Carlo simulations with the same number of surface realizations using the Kirchhoff model. However,

a best fit of the simulated FE raw data using a polynomial up to the 3rd-order can give a smooth curve, which shows very good agreement with the theoretical curve.

5.4.3 Experimental results

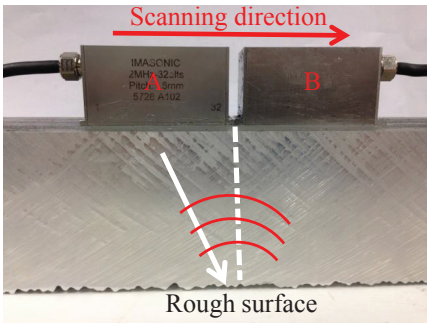

Figure 5.10: Picture of the experiment with two phased arrays

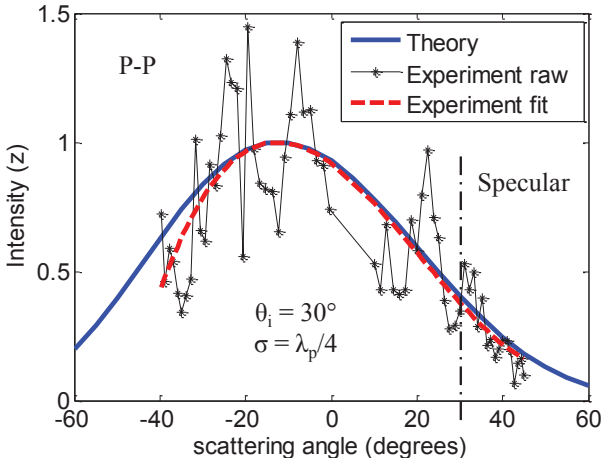

Figure 5.11: Comparison of the scattering pattern between the theory and the experiment (The experimental fit curve is obtained from a 3rd-order polynomial fit of the experimental raw data).

After the numerical simulation, the experiment using two phased arrays (Imasonic, Besancon, France) is performed, shown in Fig. 5.10, in the same scanning manner as the FE simulation. Apart from the spatial attenuation factor $\cos\theta_s$, in a real experiment the measured scattering intensity at each angle needs to be further scaled

by a directivity factor [69]. The averaged scattering pattern, denoted as the experiment raw data, from multiple scans, is shown in Fig. 5.11 along with the theoretical curve. As can be seen the experimental raw data follows the shape of the theoretical solution, although large variations can be seen. A best fit using the 3rd-order polynomial is applied on the measured data to compensate for the limited number of scans, and a very good match can now be found between the theory and the experiment.

Note that the theoretical formulae are derived from the assumption of an ideal plane wave scattering in the far field. To avoid the difference caused by a finite beam in the simulation and the experiment, the scattering intensity is normalized by the peak of the fitted data. A more rigorous comparison needs to incorporate the beam model into Eq. (5.15) and (5.16) to revise the theoretical formulae to represent the expected intensity, but this is not pursued here. However, the agreement of the shape of the patterns is clearly demonstrated in Fig. 5.9 and 5.11 between the experiment, FE simulation and the theory.

5.5 Physical discussion on the mode conversion

5.5.1 P-P mode

In this section, the developed theory is utilized to analyze the effect of roughness on the elastic wave scattering intensity, with focus on the mode conversion. The P-P scattering patterns of $< I_{pp} >$ with different S-to-P wave speed ratio γ when $\sigma = \lambda_p/3$ are shown in Fig. 5.12(a), along with the acoustic intensity when no mode conversion occurs. The intensity plotted here is the sum of its components in both x- and z- directions. The backscattering intensity is much larger than the specular intensity at such a high roughness, when the diffuse field is dominant. The elastic and the acoustic intensities coincide at the backscattering angle, and start to diverge as the scattering angle is away from the backward direction due to the mode conversion. The specular intensity is decaying quickly as γ increases, which results in a clearer peak around the backward angle for the elastic wave. The peak would become more pronounced if plotting only the z- directional scattering intensity $< I_{z,pp} >$ as shown in Fig. 5.4(b), which is the actual quantity that is measured

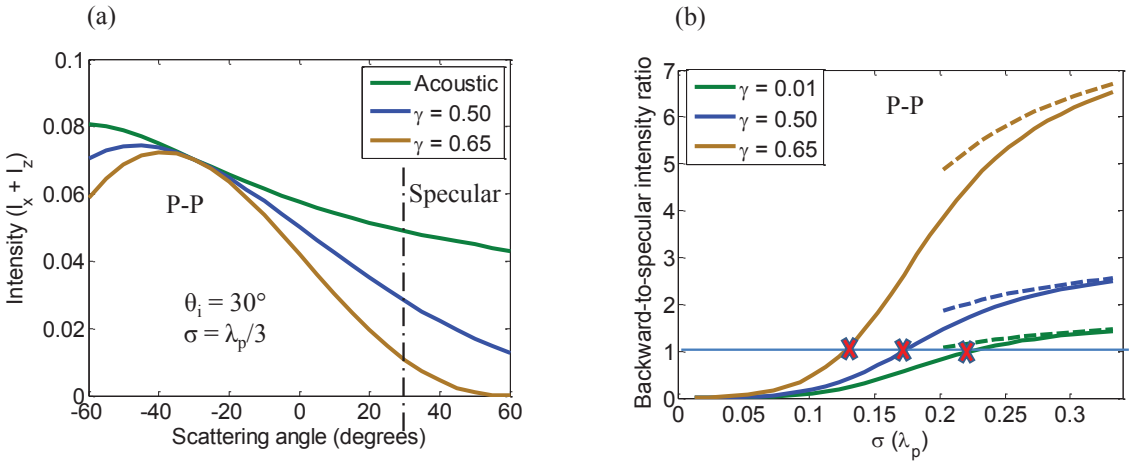

Figure 5.12: Scattering intensity for the P-P mode with an oblique incidence angle of 30^o. (a) Scattering patterns when $\sigma = \lambda_p/3$. (b) Backward-to-specular intensity ratio for the P-P mode as a function of σ. (The dashed lines denote the high frequency asymptotic solutions.)

in a real inspection. In contrast, the acoustic intensity has no peak since it is almost isotropically distributed. Hence the appearance of the backscattering peak is caused by both the diffuse field and the elasticity, which includes the mode conversion and the displacement polarization.

In Fig. 5.12(b) the backward-to-specular intensity ratio for the P-P mode is shown as a function of the RMS value of the surface roughness. The dashed line denotes the high frequency asymptotic solutions from Eq. (5.18). Apparently the ratio is increasing quickly as the surface appears to be more rough, and it is also relatively larger when the S-to-P wave speed ratio increases. By setting $\theta_s = -\theta_i$ or $\theta_s = \theta_i$ in Eq. (5.18), the 2D backward/specular intensity and the relative ratio with a high roughness can be expressed as:

$$
\begin{aligned}
&< I_{pp}(\theta_s = -\theta_i) >= \frac{L_x}{2\sqrt{2\pi}\cos^3\theta_i r} \cdot \frac{1}{\sigma_g} \exp[-\frac{\tan^2\theta_i}{2\sigma_g^2}], \quad \text{Backward intensity} \\
&< I_{pp}(\theta_s = \theta_i) >= \frac{L_x F_{pp}^2(\theta_s = \theta_i)}{2\sqrt{2\pi}\cos\theta_i r} \cdot \frac{1}{\sigma_g}, \quad \text{Specular intensity} \\
&\frac{< I_{pp}(\theta_s = -\theta_i) >}{< I_{pp}(\theta_s = \theta_i) >} = \frac{\exp[-\frac{\tan^2\theta_i}{2\sigma_g^2}]}{\cos^2\theta_i F_{pp}^2(\theta_s = \theta_i)}
\end{aligned}
\tag{5.19}
$$

Recall that the RMS gradient $\sigma_g = \sqrt{2}\sigma/\lambda_x$ in 2D, and in the high frequency limit the intensity should be only related to the surface gradient as shown in Eq. (5.18).

Clearly the backward intensity is only a function of roughness and it has the same value as the acoustic case. This is not surprising since for any stress-free flaw in an isotropic elastic solid the Kirchhoff approximation for the pulse-echo far-field scattering amplitude is identical to the Kirchhoff approximation for the scalar scattering amplitude of a void in a fluid [70]. Hence the specific observation of the lines meeting at the backward angle in Fig. 5.12(a) can be generalized to other values of roughness. However, the specular intensity does not only rely on the roughness σ_g, but also on the mode conversion through $F_{pp}(\theta_i = \theta_s)$, as part of the incident P waves are converted to S waves. Note that for the P-P mode the effects from the mode conversion and the roughness are decoupled. Specifically, the mode conversion is only included in the angular factor $F_{pp}(\theta_s = \theta_i)$, and the effect of the roughness is shown in σ_g. Furthermore, From Eq. (5.19) it is easy to find that the backward-to-specular intensity ratio increases as the roughness increases, as shown in Fig. 5.12(b).

It might be interesting to calculate the roughness value when the backward and the specular intensity are equivalent, marked as the intersection points in Fig. 5.12(b). To estimate the corresponding σ, one may use the full solution Eq. (5.15) and let the backward and the specular intensity be equal, by keeping the first four terms. The resulting equation has only one unknown variable σ, which then can be solved numerically. For example, in this way the RMS value σ when $\gamma = 0.5$ is calculated approximately as $0.17\lambda_p$.

5.5.2 P-S mode

To further illustrate the effects of the roughness and the elasticity on mode converted S waves, Fig. 5.13(a) shows the dipole-like scattering patterns for the P-S mode with different S-to-P wave speed ratio when $\sigma = \lambda_p/3$. As can be seen at the backward direction the S wave intensity vanishes as expected, and it reaches a peak around the specular angle, indicating a strong mode conversion effect. It needs to be mentioned that in [64] the valid region of the Kirchhoff approximation was established only for the P-P mode. Hence for the roughness shown here ($\sigma = \lambda_p/3 = \lambda_s/1.5$), we cannot be as confident about the accuracy of the scattering intensity for the P-S mode as for the P-P mode, since the scattered S wave shows a shorter wavelength. However, the trend of the scattering pattern for the P-S mode should remain the same as the

roughness is not extremely high.

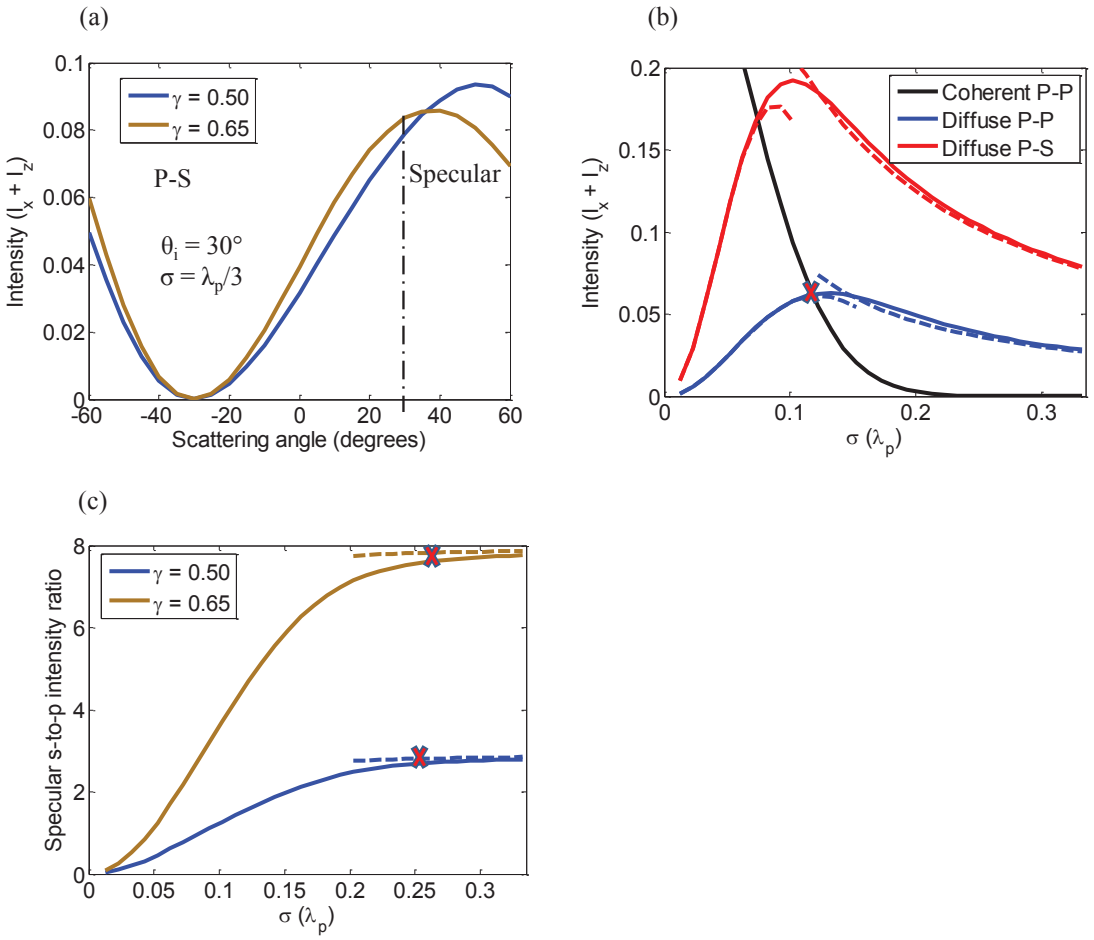

Figure 5.13: Mode converted S waves with an oblique incidence angle of 30^o. (a) Scattering patterns for the P-S mode when $\sigma = \lambda_p/3$. (b) Coherent and diffuse intensities for P-P and P-S modes in the specular direction. (c) Specular S-to-P intensity ratio as a function of σ The dashed lines in (b) represent both the low and high frequency solutions, and the dashed lines in (c) are the high frequency solutions).

In Fig. 5.13(b) the coherent and the diffuse intensity in the specular direction ($\theta_s = 30^o$) are plotted separately for both P-P and P-S modes. Again the dashed lines represent the low frequency approximation by keeping the first four terms in Eq. (5.16) and the high frequency asymptotic solution, which connect well around $\sigma = \lambda_p/8$ to give the intensity covering the entire frequency range. Apparently the diffuse intensity for the mode converted S waves is much larger than for the P waves, which implies a significant energy leakage from the incident P to scattered S waves.

To quantify the mode conversion effect, the Specular S-to-P intensity ratio is shown

in Fig. 5.13(c) with respect to the RMS value σ. It can be seen that the mode conversion effect increases when the surface becomes more rough in the specular angle, and levels off approximately after $\sigma = \lambda_p/4$. By using Eq. (5.18), the high frequency asymptotic solution for the P-S mode scattering intensity at the specular angle can be expressed as:

$$< I_{ps}(\theta_s = \theta_i) >= \frac{F_{ps}^2 L_x}{(\gamma+1)\sqrt{2\pi}\cos\theta_i r\sigma_g} \exp\left[-(\frac{\gamma-1}{\gamma+1})^2 \frac{\tan^2\theta_i}{2\sigma_g^2}\right] \tag{5.20}$$

In Eq. (5.20), for the P-S mode the effects of the roughness and the mode conversion are no longer decoupled, which is different from the P-P mode case shown in Eq. (5.19). The Specular S-to-P intensity ratio can hence be expressed as:

$$\frac{< I_{ps}(\theta_s = \theta_i) >}{< I_{pp}(\theta_s = \theta_i) >} = \frac{F_{ps}^2}{F_{pp}^2}\frac{2}{\gamma+1} \exp\left[-(\frac{\gamma-1}{\gamma+1})^2 \frac{\tan\theta_i^2}{2\sigma_g^2}\right] \tag{5.21}$$

When pushing Eq. (5.21) to the extreme high frequency limit by assuming that $\sigma_g \to \infty$, Eq. (5.21) can be simplified as:

$$\frac{< I_{ps}(\theta_s = \theta_i) >}{< I_{pp}(\theta_s = \theta_i) >} = \frac{F_{ps}^2}{F_{pp}^2}\frac{2}{\gamma+1} \tag{5.22}$$

which only depends on the incidence angle and the S-to-P wave speed ratio. Using Eq. (5.22), the value of the plateau in the high frequency for the S-to-P intensity ratio can be predicted. For instance, by substituting $\gamma = 0.50$ and 0.65 into Eq. (5.22), the S-to-P intensity ratio is calculated as 2.91 and 7.93 as marked in Fig. 5.11(c), showing very good agreement with the curves.

In addition, from Fig. 5.13(b) a noticeable peak is seen at an intermediate roughness ($\sigma \approx \lambda_p/8$) for both diffuse P-P and P-S intensity, and for the P-P mode it almost coincides with the intersection point when the coherent and the diffuse intensities are equivalent, as marked by the red cross in the plot. Small roughness ($\sigma \leq \lambda_p/8$) causes the appearance of the diffuse field, which then starts to be attenuated by increased roughness after σ is larger than some intermediate value σ_{med}. Hence σ_{med} is some measure of the roughness of the surface, indicating whether the roughness constructively or destructively affects the diffuse intensity. According to Eq. (5.16),

the value of σ_{med} can be found by letting $\frac{\partial I_{pp}^d}{\partial \sigma} = 0$ and solving the resulting equation:

$$\sum_{n=1}^{\infty} \frac{(n-g)g^{n-1}}{n!\sqrt{n}} = 0 \tag{5.23}$$

Where $g = 4k_p^2\sigma^2 cos^2\theta_i$. By keeping the first four terms of Eq. (5.16), the value of σ is found as $\lambda_p/7.5$.

To better understand the intermediate RMS value around $\lambda_p/7.5$, the Rayleigh parameter is quoted here [4]:

$$R_a = k_p\sigma \cos\theta_i \tag{5.24}$$

It represents the averaged relative phase difference of scattered waves from two surface points in the specular direction. The Rayleigh criterion states that if $R_a \leq \pi/4$, then the surface is 'smooth', otherwise it is 'rough'. By substituting θ_i =30^o into Eq. (5.24), the critical σ can be calculated as $\lambda_p/7$, which is almost the same as the value solved from Eq. (5.23) corresponding to the peak of the diffuse intensity. Therefore the critical RMS from the conventional Rayleigh criterion agrees with the RMS for the peak point of the diffuse intensity, and also the intersection point of the coherent and the diffuse intensity.

5.5.3 2D roughness induced SH mode and depolarization

For an elastic wave scattered from a flat surface or a corrugated surface infinitely long in the y- direction, the displacement polarization is within the x-z plane, often called the in-plane motion. If the surface is rough as a function of both x and y, the in-plane waves are coupled with the scattered shear horizontal (SH) waves in the y- direction. The 'depolarization' occurs, as the displacement is now composed of both in-plane (x-z plane) and out-of-plane (y- direction) motions induced by the roughness in the y-axis.

In this section, a study is performed to analyze the depolarization effect for the SH mode using the developed formulae. The incidence angles of P waves are still fixed

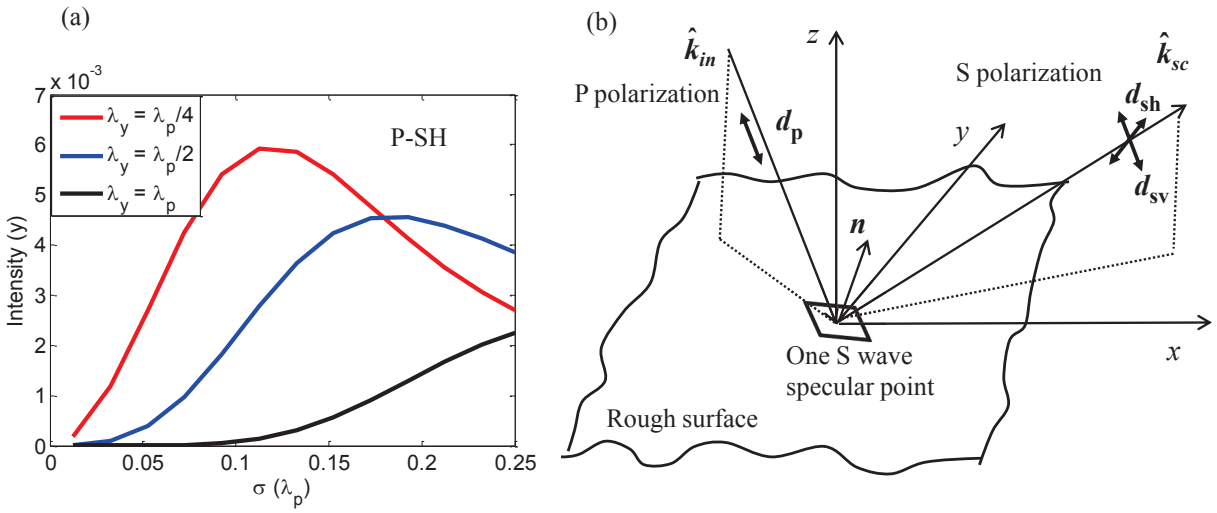

Figure 5.14: (a) Scattering intensity $< I_{y,ps} >$ as a function of σ for different correlation lengths in the y- direction. (b) Sketch of the S wave specular point to illustrate the polarization in 3D.

as $\theta_{ix} = 180^o$ and $\theta_{iz} = 30^o$. Specifically, the quantity $I_{y,ps}$ which is the intensity in the y- direction, is investigated since it is the main feature of the depolarization. As noticed in Eq. (5.15) the coherent component of $I_{y,ps}$ is proportional to that from a flat surface. Hence the coherent field in the y- direction is zero, as when $L_y \to \infty$ no motion in the y- dimension is induced for a flat surface. Therefore the depolarization effect for a surface infinitely long in the y- dimension is purely contributed from the diffuse field.

The scattering patterns of the SH mode from low to high roughness are shown in Fig. 5.5(c) and Fig. 5.6(c), respectively. The increased roughness causes a considerable shift of two symmetric peaks from $\theta_{sx} = 90^o, |\theta_{sz}| = 25^o$ roughly to $\theta_{sx} = 115^o, |\theta_{sz}| = 50^o$. Fig. 5.14 shows $I_{y,ps}$ as a function of the RMS value when $\theta_{sx} = 90^o, |\theta_{sz}| = 45^o$, with different out-of-plane correlation lengths λ_y. As λ_y increases the SH mode intensity decays quickly, and the decay is more prominent when λ_y reaches one wavelength. It is because in this manner the surface is becoming smoother in the y- direction. As can be imagined in the extreme situation when $\lambda_y \to \infty$, the SH mode intensity would vanish since no depolarization takes place.

To quantify how the SV motion converts to the SH motion when the roughness in the y- direction is imposed, a depolarization factor is defined here for the scattered

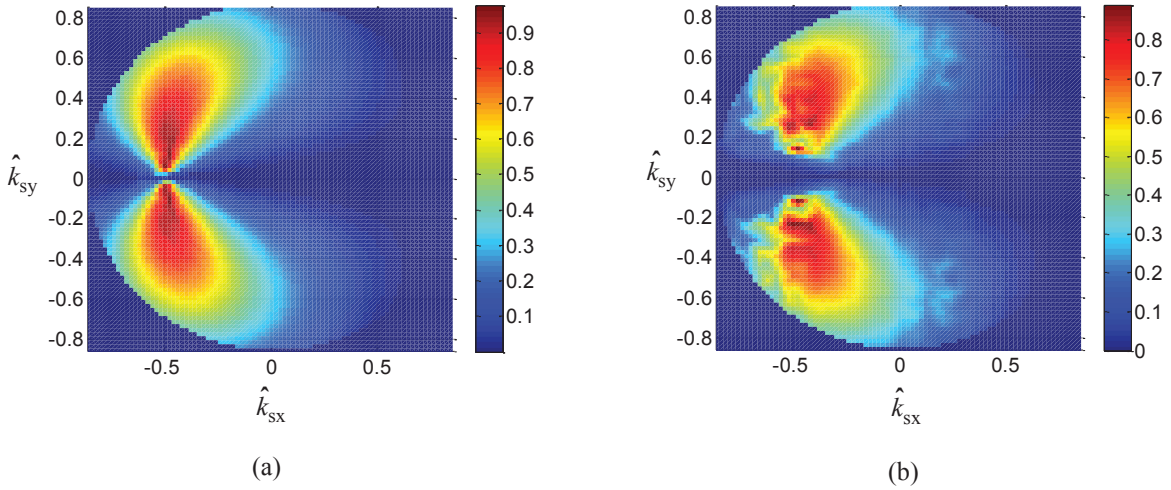

Figure 5.15: Depolarization pattern in terms of $\hat{k}_x$ and $\hat{k}_y$ when $\theta_{ix} = 180^o, \theta_{iz} = 30^o$. (a) Diffuse intensity. (b) Total intensity when $\sigma = \lambda_p/30 \approx \lambda_s/15$.

S waves, as the ratio between the y- directional intensity and the sum of all the components of intensities:

$$Q = I_{y,ps}/I_{ps} \tag{5.25}$$

As we know the depolarization is purely due to the diffuse field when the surface is infinitely long in the y- direction within the Kirchhoff approximation. According to Eq. (5.15), for the diffuse field the finite sum of the exponential terms can be cancelled when dividing $I^d_{y,ps}$ by I^d_{ps} in Eq. (5.25). Only the angular factors are left and the depolarization factor for the diffuse intensity in Eq. (5.25) can be simplified as:

$$Q = F^2_{y,ps}/F^2_{ps} \tag{5.26}$$

Eq. (5.26) indicates that the depolarization factor for the diffuse field does not rely on the roughness, and it is only a function of the incidence/scattering angle and the S-to-P wave speed ratio. In fact, according to the slope approximation, the scattered waves are mainly contributed from the 'specular points', especially for the diffuse field. Hence, the polarization vectors for the scattered waves physically should be the same as those from 'specular points' for the S mode as shown in Fig. 5.14(b). As a result, the depolarization factor determined by the polarization vector is also

the same as that from the 'specular points', and hence for the diffuse field it is independent of the actual value of the roughness. Fig. 5.15(a) shows the diffuse wave depolarization factor as a function of the scattering angles in 3D, with a 30^o oblique incident wave within the x-z plane.

The angular distribution of the depolarization factor for the diffuse field can be described by Fig. 5.15(a), However, in reality the surface has a finite dimension in the y- direction, so that the coherence effect needs to be included since the coherent intensity in the y- direction is no longer zero. The depolarization factor would be a function of the roughness, which is shown in Fig. 5.15(b) for slightly rough surfaces when $\sigma = \lambda_p/30 \approx \lambda_s/15$. As can be seen the pattern in Fig. 5.15(b) is not the same as that in Fig. 5.15(a), as some coherence effects are included. Note that when the roughness is high, the diffuse field is dominant and the coherent field is negligible. The depolarization pattern follows Fig. 5.15(a), which is independent of the actual roughness. In contrast when the roughness is small the coherent field increases and it affects the depolarization. Although the two patterns in Fig. 5.15(a) and (b) are not the same, they roughly remain the similar shape.

5.6 Summary

In this chapter, an elastodynamic theory to predict the expected scattering intensity, especially the diffuse field from randomly rough surfaces, is presented. Slope approximations are applied assuming 'specular points' for different modes, which enables the analytical manipulation of the ensemble averaging of the diffuse intensity as well as the high frequency asymptotic solution. The theory is verified by comparison with the numerical Monte Carlo simulations and experiment, within the valid region of the Kirchhoff assumption. In particular, the effects of the roughness on the mode conversion, and consequently on the scattering intensity, are discussed. It is found that a considerable proportion of the incident P waves are converted to scattered S waves, and this effect is very strong around the specular direction. The mode conversion effect increases as the surface appears to be more rough, which results in unique scattering patterns for different modes. For instance, a remarkable peak around the backward angle can be seen for the P-P mode for surfaces with a high roughness. In addition, the 2D roughness-induced out-of-plane SH mode and

the depolarization is quantitatively analyzed. It is found that the amplitude of the out-of-plane intensity depends on the roughness, and is very sensitive to the out-of-plane correlation length. However, the depolarization factor for the diffuse field remains a constant with respect to the roughness. The coherent field affects this factor for surfaces of finite dimensions, although it does not change the main shape of the depolarization pattern.

Chapter 6

Conclusions

6.1 Thesis Review

In this thesis a systematic study of the elastic wave scattering from randomly rough surfaces was performed, in order to acquire fundamental understanding of the surface scattering mechanisms, and develop and assess modelling capabilities, with the ultimate motivation of improving the detectability of rough defects for NDE. Chapter 1 introduced the basic background, and the motivations for both industrial applications and wave physics. Chapter 2 provided statistical knowledge of rough surfaces for the use of later chapters. The main novel contributions of this study were conducted in three subsequent parts in a logical sequence: (a) the numerical method developed in Chapter 3, (b) the validity of the elastodynamic Kirchhoff approximation in Chapter 4, and (c) theoretical solutions for the diffuse field in Chapter 5.

In Chapter 3, a detailed literature review was given to cover numerical methods which have been used to calculate surface scattering problems. The basic hybrid idea to link the local computational model and the global analytical approach was introduced, based on which a new method was developed with improved efficiency. The approach combines the explicit FE formulation and the boundary integral in the time domain to compute the scattered waves in both near and far fields, and is verified by different numerical examples.

Chapter 4 examined the validity of the elastodynamic Kirchhoff approximation for

calculating scattering from randomly rough surfaces. Monte Carlo simulations were run on Gaussian surfaces, using both the Kirchhoff model and the benchmark numerical method developed in Chapter 3. Comparisons were made regarding the averaged scattering amplitude from multiple realizations, and different empirical rules in 2D and 3D were generalized to judge when the use of KA is reliable given a candidate rough defect.

Chapter 5 developed a theory for predicting the expected intensity for elastic wave scattering according to the statistical model of the surface. The Kirchhoff approximation that has been carefully evaluated in Chapter 4 was applied to derive the analytical solutions for both the diffuse and the coherent intensity. Both Monte Carlo simulations and experiments were performed, and the results agree well with those predicted by the developed theory. In addition, the analytical solutions were applied to theoretically investigate the effect of the roughness on mode conversions, including the depolarization caused by the 2D roughness.

6.2 Summary of Findings

6.2.1 Extension of the hybrid method

Analytical solutions are only capable of solving scattering problems for defects with regular geometries. For scattering from randomly rough surfaces, different numerical methods can be implemented, among which the hybrid method is very promising since it combines the advantages of both FE and BI. In the time domain, a generic hybrid approach for the application in NDE has been developed [22].

In our work, the existing capability of the time-domain hybrid method has been extended, and the new approach is feasible for modelling the rough surface scattering. In particular, the excitation nodes for the local FE model and the monitoring nodes for the boundary integral are now located on the surface of the scatterer. Hence the size of the FE domain can be further reduced, and the computational effort for the boundary integral is also minimized. The boundary integral is calculated using the surface displacement and traction instead of the wave potential used in the previous

hybrid model, and it is accurate in both near and far fields. The previous hybrid scheme for integration is programmed in the frequency domain, so that a loop of FFT and inverse FFT is needed to recover the scattering waveform. In contrast, the boundary integral in Chapter 3 is numerically represented as a superposition of retarded time traces. As a result, it avoids the need of FFT and improves the efficiency especially for a wide band signal. In addition, the new approach has shown good accuracy for simulations with rough surfaces in a half space, and also scatterers with non stress-free boundary conditions. It significantly extends the modelling capability of the previous hybrid method to include more complex inspection scenarios.

6.2.2 Evaluation of the elastodynamic Kirchhoff approximation

The Kirchhoff approximation has been widely applied by many people for a quick calculation of the scattering from randomly rough surfaces, and it is particularly suitable for Monte Carlo simulations. However, the KA is based on the tangential plane assumption and it neglects multiple scattering, shadowing effects and surface waves. Hence the validity of KA needs to be established before the implementation. There have been some evaluation works for acoustic and electromagnetic waves, but very few studies can be found related to elastic waves. Besides, all previous works with different waves have been limited in 2D models.

In Chapter 4, the elastodynamic Kirchhoff approximation has been examined in both 2D and 3D by comparison with a benchmark numerical method described in Chapter 3 in the time domain. Monte Carlo simulations have been performed using multiple realizations of Gaussian surfaces with different roughnesses, and the sample averaged amplitude of the scattering signals is used for comparison . Rules for the validity of the KA in terms of the roughness have been found, which can serve as empirical guides for use in industry. Particularly, the corresponding rules for the validity in 3D have been shown to be stricter than those in 2D, and the discrepancy is caused by the increased local and global errors, due to the variation of height in one additional direction. The study has highlighted the importance of taking 3D effects into consideration when modelling the rough surface scattering using the KA,

as all realistic rough defects are expected to be 3D. In addition, simulations with slightly oblique incident angles have been run, concluding that a modest incident angle can improve the performance of the KA compared with the normal incident case, as the surface in this view appears to be relatively 'less rough'.

6.2.3 Development of the elastodynamic Kirchhoff theory

The expected scattering intensity can be obtained by a sample average from sufficient surface realizations, via the Monte Carlo approach with either the numerical method shown in Chapter 3 or the Kirchhoff model. However, it is difficult to generalize the physical relation linking the surface statistics and the expected scattering field. In this sense the theoretical solutions are preferred as they are explicit expressions, from which the effect of roughness on the expected intensity can be easily revealed. The theory for the coherent intensity can be found for elastic waves but not for the more complicated diffuse intensity.

In Chapter 5, an elastodynamic theory has been developed for predicting both the diffuse and the coherent intensity from randomly rough surfaces. The derivation is based on the Kirchhoff approximation whose region of validity has been known from the studies in Chapter 4. The theory of 'specular points' has been adopted from the community of optics to approximate the slope terms inside the boundary integral, enabling further analytical manipulations of the ensemble averaging for the diffuse intensity. Furthermore, a high frequency asymptotic solution has been derived which is proportional to the distribution of the surface slopes. Monte Carlo simulations have been run to approximate the expected intensity from the sample average, which has shown excellent agreement with the theoretical results and also with the asymptotic solutions. Experiments have also been undertaken by using two phased arrays with a corrugated surface sample. The expected intensity is approximated as an average of measured scattering intensities by scanning different sections of the surface. Good agreement between the theory and the experimental data has been found by comparing the scattering patterns.

The theory has been applied to analytically investigate the impact of the roughness

and elasticity on the mode conversion. Significant amounts of incident energy have been found to be leaked to mode converted scattered waves, and the leakage becomes more severe when the scattering angle is away from the backward direction. As a consequence, the scattering patterns for different incident/scattering modes are greatly affected by the roughness. For instance, it has been observed that a peak appears around the backward angle with a high roughness for the P-P mode, caused by both the increased diffuse field and the elasticity of the material. The S-to-P intensity ratio in the specular direction has been shown to increase as the surface appears to be more rough, and level off after some high roughness when the diffuse field dominates. In addition, the 2D roughness-caused depolarization for elastic waves has also been studied by examining the out-of-plane intensity of the SH mode. It was found that the intensity of the SH mode highly relies on the roughness, and is very sensitive to the out-of-plane correlation length. In contrast, the depolarization factor describing to what extent the SH polarization deviates from the SV polarization, has been found to be almost unchanged for the diffuse field regardless of the roughness.

6.3 Future works

6.3.1 Computational method and its application

As mentioned in Chapter 3, the Perfect Matched Layer (PML) is known to be the most efficient method to absorb waves at the exterior of a model when simulating scattering in an unbounded domain. However although established for use with elastic waves in the frequency domain, it has not been successfully incorporated with the 2nd-order explicit scheme for the elastodynamic problems in a time-domain FE simulation. Hence it would be useful to find a way of implementing the PML since it can greatly reduce the size of the local FE domain compared with the existing techniques of absorbing layers.

The FE-BI approach can be very useful with applications on sizing and imaging algorithms requiring time-domain signals. One of the potential applications for NDE is modelling the tip diffraction from rough defects, based on which one may investi-

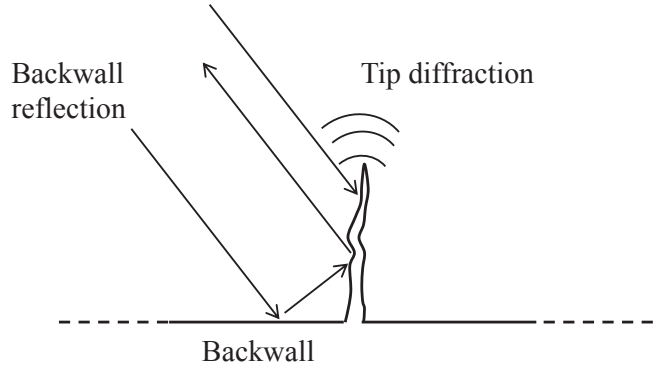

Figure 6.1: Illustration of the waves scattered from a branched crack growing from a backwall.

gate the effects of roughness on the time-of-flight sizing algorithm. As can be seen in Fig. 1.2 the tip diffraction is mixed with the randomly reflected signals from different parts of the rough surface, and hence it is challenging to size the length of the defect according to the time difference of the two tip signals. A possible solution is to use a shorter incident pulse to separate the tip signals from the waveform. Another way worth trying is to transfer the scattering signal into the frequency domain, and extract some coherent feature to enhance the amplitude of the tip signals. A similar application can be carried out for imaging branched smooth/rough cracks, when the scattering signals are polluted with reflections from the smooth/rough backwall as shown in Fig. 6.1. The FE-BI approach would be useful to study the scattering behavior, and hopefully help the development of a more accurate imaging algorithm.

6.3.2 Inverse problems

In Chapter 5, analytical solutions have been derived to calculate the mean scattering intensity from the knowledge of surface statistics, which is known as a forward problem. Conversely, one can solve the inverse problem using the same formulae to recover the surface statistics by measuring the angular distribution of the intensity. The simple analytical formulae provide a straightforward inversion procedure within the valid region of the Kirchhoff approximation. The RMS value and the pdf of the surface height can be estimated from the coherent intensity by changing the frequency with a normal pulse echo inspection. In practice it can be realized

by sending low frequency incident waves when the coherent field is dominant. The recovery of the correlation function is much more complicated since it relates with the inversion of a N-dimensional function. However, since the theoretical expression for the diffuse intensity has been obtained, it is possible to invert the complete correlation function by measuring the diffuse field at multiple scattering angles. In addition, it would be interesting to investigate the performance of different wave modes on the inversion procedure. It is expected that different modes should give similar recovered results, as a check of the consistency of the algorithm.

Two practical issues have to be addressed for the experiment and real applications. The theory in Chapter 5 is based on an ideal plane wave incident on a surface with a finite length, and one of the proposed future works is to include the beam model into the theoretical solution and the inverse algorithms as well. In this manner the energy illuminated on the surface can be calculated precisely, so that the inversion results can be compared directly with the experiment. Furthermore, one potential application of the inverse algorithm would be for the monitoring of corrosion on the inside surface of a pipe or vessel, as it could provide a way to 'see' the surface condition. For a typical wall thickness of 8mm to 20mm, the transducer or the array is within the near field of the rough surface. Hence the theoretical formulae originally derived using the far field assumption would need to be adjusted, in order to take the near field effect into consideration. The inverse problem of the surface statistics is currently under development by the author, and some ideas will be implemented in future.

6.3.3 Physical study of the random scattering field

Although in Chapter 5 a theory was presented which well explains the scattering behavior from randomly rough surfaces using the KA, it might not be reliable when the roughness of the surface is beyond the valid region of the Kirchhoff theory. For example, for surfaces with extremely high RMS values ($\sigma \geq 0.8\lambda$), the multiple scattering phenomena become comparable with the single scattering, or even dominant. The FE-BI method is a good way to model such situations since it includes all wave scattering physics. Alternatively the multiple scattering theory could be

incorporated with the Kirchhoff approximation, which could possibly lead to some analytical expressions. In addition, the study in this thesis has been focused on the effect of roughness on the bulk wave scattering, while it is also important to investigate the scattering of Rayleigh waves by rough surfaces. Intuitively higher roughness leads to severe loss of the surface wave energy as waves are scattered into the half space. However, a fraction of the energy might also be trapped inside some 'valleys' of the rough surface also due to the high roughness. Again the surface wave is not included in the Kirchhoff theory so that the FE-BI method can be implemented to study the Rayleigh wave scattering in the future.

References

[1] J. A. Ogilvy. Computer simulation of acoustic wave scattering from rough surfaces. *J. Phys. D: Appl. Phys.*, 21:260–277, 1988.

[2] J. A. Ogilvy and I. D. Culverwell. Elastic model for simulating ultrasonic inspection of smooth and rough defects. *Ultrasonics*, 29:490–496, 1991.

[3] P. Rajagopal, M. Drozdz, and M. J. S. Lowe. Towards improved finite element modelling of the interaction of elastic waves with complex defect geometries. In D. O. Thompson and D. E. Chimenti, editors, *Review of Progress in Quantitative NDE*, volume 28a of *AIP Conference Proceedings*, pages 49–56. American Institute of Physics, Chicago, IL, 2009.

[4] J. A. Ogilvy. *Theory of Wave Scattering from Random Rough Surfaces*. Adam Hilger Ltd, 1991.

[5] J. Pettit, A. E. Walker, and M. J. S. Lowe. Improved detection of rough defects for ultrasonic nondestructive evaluation inspections based on finite element modeling of elastic wave scattering. *IEEE Trans. Ultrason. Ferroelectr. Freq. Control.*, 62:1797–1808, 2015.

[6] M. V. Berry. The statistical properties of echoes diffracted from rough surfaces. *Phil. Trans. R. Soc. Lond. A*, 273:611–654, 1972.

[7] H. Lawrence, F. Demontoux, J. P. Wigneron, P. Paillou, T. D. Wu, and Y. H. Kerr. Evaluation of numerical modeling approach based on the finite-element method for calculating the rough surface scattering and emission of a soil layer. *IEEE Geosci. Remo. Sens. Lett.*, 8:953–957, 2011.

[8] E. I. Thorsos. Acoustic scattering from a 'Pierson-Moskowitz' sea surface. *J. Acoust. Soc. Am.*, 88:335–349, 1990.

[9] J. A. Ogilvy. Theoretical comparison of ultrasonic signal amplitudes from smooth and rough defects. *NDT & E Int.*, 19(6):371–385, 1986.

[10] W. Makinde, N. F-Cristini, and E. d. Bazelaire. Numerical modelling of interface scattering of seismic wavefield from a random rough interface in an acoustic medium: comparison between 2D and 3D cases. *Geophys. Prospect.*, 53:373–397, 2005.

[11] A. A. Maznev. Boundary scattering of phonons: Specularity of randomly rough surface in the small-perturbation limit. *Phys. Rev. B: Condens. Matter*, 91(134306):1–9, 2015.

[12] K. F. Warnick and W. C. Chew. Numerical simulation methods for rough surfae scattering. *Waves Random Media*, 11:R1–R30, 2001.

[13] M. Frehner, S. M. Schmalholz, E. H. Saenger, and H. Steeb. Comparison of finite difference and finite element methods for simulating two-dimensional scattering of elastic waves. *Phys. Earth Planet. Inter.*, 171(1–4):112–121, 2008.

[14] P. Moczo, Kristek J, M. Galis, P. Pazak, and M. Babazovjech. The finite-difference and finite-element modeling of seismic wave propagation and earthquake motion. *Acta Phys. Slovaca*, 57(2):177–406, 2007.

[15] P. Rajagopal and M. J. S. Lowe. Scattering of fundamental shear horizontal guided wave by a part-thickness crack in an isotropic plate. *J. Acoust. Soc. Am.*, 124(1):78–92, 2008.

[16] M. B. Drozdz. Efficient finite element modelling of ultrasound waves in elastic media. *Phd thesis, Department of Mechanical Engineering, Imperial College London*, 2008.

[17] F. Janod and O. Coutant. Seismic response of three-dimensional topographies using a time-domain boundary element method. *Geophys. J. Int.*, 142:603–614, 2000.

[18] O. von Estorff and M. J. Prabucki. Dynamic response in the time domain by coupled boundary and finite elements. *Comp. Mech.*, 6:35–46, 1990.

[19] A. J. .C. Jarvis and F. B. Cegla. Application of the distributed point source method to rough surface scattering and ultrasonic wall thickness measurement. *J. Acoust. Soc. Am.*, 132(3):1325–1335, 2012.

[20] P. D. Wilcox and A. Velichko. Efficient frequency-domain finite element modeling of two-dimensional elastodynamic scattering. *J. Acoust. Soc. Am.*, 127(1):155–165, 2010.

[21] A. Velichko and P. D. Wilcox. A generalized approach for efficient finite element modeling of elastodynamic scattering in two and three dimensions. *J. Acoust. Soc. Am.*, 128(3):1004–1014, 2010.

[22] P. Rajagopal, E. A. Skelton, W. Choi, M. J. S. Lowe, and R. V. Craster. A generic hybrid model for bulk elastodynamics, with application in ultrasonic nondestructive evaluation. *IEEE Trans. Ultrason. Ferroelectr. Freq. Control*, 50(6):1239–1252, 2012.

[23] J. Zhang, B. W. Drinkwater, and P. D. Wilcox. Longitudinal wave scattering from rough crack-like defects. *IEEE Trans. Ultrason. Ferroelectr. Freq. Control.*, 58:2171–2180, 2011.

[24] J. A. Ogilvy and J. A. G. Temple. Diffraction of elastic waves by cracks: application to time-of-flight inspection. *Ultrasonics*, pages 259–269, 1983.

[25] J. A. Ogilvy. Model for the ultrasonic inspection of rough defects. *Ultrasonics*, 27:69–79, 1989.

[26] J. O. A. Robertsson, R. Laws, C. Chapman, J. P. Vilotte, and E. Delavaud. Modelling of scattering of seismic waves from a corrugated rough sea surface: a comparison of three methods. *Geophys. J. Int.*, 167:70–76, 2006.

[27] R. K. Chapman, J. E. Pearce, S. F. Burch, L. Fradkin, and M. W. Toft. Recent in-house developments in theoretical modelling of ultrasonic inspection. *Insight*, 49:93–97, 2007.

[28] E. I. Thorsos. The validity of the Kirchhoff approximation for rough surface scattering using a Gaussian roughness spectrum. *J. Acoust. Soc. Am.*, 83:78–92, 1988.

[29] J. A. Ogilvy. An estimate of the accuracy of the Kirchhoff approximation in acoustic wave scattering from rough surfaces. *J. Phys. D: Appl. Phys.*, 19:2085–2113, 1986.

[30] M. F. Chen and A. K. Fung. A numerical study of the regions of validity of the Kirchhoff and small-perturbation rough surface scattering models. *Radio Science*, 23:163–170, 1988.

[31] R. A. Roberts. The effect of crack morphology on ultrasonic response. In D. O. Thompson and D. E. Chimenti, editors, *Review of Progress in Quantitative NDE*, volume 1430 of *AIP Conference Proceedings*, pages 150–157. American Institute of Physics, Denver, CO, 2012.

[32] P. Beckmann and A. Spizzichino. *The scattering of electromagnetic waves from rough surfaces.* Artech House, INC, 1987.

[33] C. W. Horton. Theoretical studies on the scattering of acoustic waves from a rough surface. *J. Acoust. Soc. Am.*, 41(3):627–634, 1966.

[34] D. E. Barrick. Unacceptable height correlation coefficients and the quasi-specular component in rough surface scattering. *Radio Science*, 5(4):647–654, 1970.

[35] P. Meakin. *Fractals, Scaling and Growth Far from Equilibrium.* Cambridge University Press, Cambridge, England, 1998.

[36] I. Simonsen, D. Vandembroucq, and S. Roux. Wave scattering from self-affine surfaces. *Phy. Rev. E*, 61(5):5914–5917, 2000.

[37] R. Laws and E. Kragh. Rough seas and time lapse seismic. *Geophys. Propect.*, 167:195–208, 2002.

[38] J. Zhang, B. W. Drinkwater, and P. D. Wilcox. Effect of roughness on imaging and sizing rough crack-like defects using ultrasonic arrays. *IEEE Trans. Ultrason. Ferroelectr. Freq. Control.*, 59:939–948, 2012.

[39] C. F. Ying and R. Truell. Scattering of a plane longitudinal wave by spherical obstacle in an isotropically elastic solid. *J. Appl.Phys.*, 27:1086–1097, 1956.

[40] J. D. Achenbach. *Reciprocity in elastodynamics*. Cambridge University Express, Cambridge, UK, 2003.

[41] A. Frankel and R. W. Clayton. Finite difference simulations of seismic scattering: Implications for the propagation of short-period seismic waves in the crust and models of crustal heterogeneity. *J. Geophys. Res*, 91(B6):6465–6489, 1986.

[42] A. S. M. Israil and P. K. Banerjee. Two-dimensional transient wave-propagation problems by time-domain BEM. *Int. J. Solids Structures*, 26(8):851–864, 1990.

[43] P. Huthwaite. Accelerated finite element elastodynamic simulations using the GPU. *J. Comput. Phys.*, 257:687–707, 2014.

[44] F. Ihlenburg. Finite element analysis of acoustic scattering. *Springer-Verlag New York, Inc*, 1998.

[45] N. Gengembre, A. Lhemery, R. Omote, T. Fouquet, and A. Schumm. A semi-analytic FEM hybrid model for simulating UT configurations involving complicated interactions of waves with defects. In D. O. Thompson and D. E. Chimenti, editors, *Review of Progress in Quantitative NDE*, volume 23 of *AIP Conference Proceedings*, pages 74–80. American Institute of Physics, Green Bay, WI, 2004.

[46] D. L. Karabalis and D. E. Beskos. Dynamic response of 3-D flexible foundations by time domain BEM and FEM. *Soil. Dyn. Earthq. Eng.*, 4(2):91–101, 1985.

[47] P. Rajagopal, M. Drozdz, E. A. Skelton, M. J. S. Lowe, and R. V. Craster. On the use of absorbing layers to simulate the propagation of elastic waves in unbounded isotropic media using commercially available finite element packages. *NDT & E Int.*, 51:30–40, 2012.

[48] J. R. Pettit, A. Walker, P. Cawley, and M. J. S. Lowe. A Stiffness Reduction Method for efficient absorption of waves at boundaries for use in commercial Finite Element codes. *Ultrasonics*, 54(7):1868–1879, 2014.

[49] E. Becache, P. Joly, and C. Tsogka. A new family of mixed finite elements for the linear elastodynamic problem. *SIAM J. Numer. Anal.*, 39(6):2109–2132, 2002.

[50] J. Virieux and S. Operto. An overview of full-waveform inversion in exploration geophysics. *Geophysics*, 74(6):1–26, 2009.

[51] K. F. Graff. Wave motion in elastic solids. *Dover Publication, INC, New York*, 1975.

[52] F. Collino and C. Tsogka. Application of th perfectly matched absorbing layer model to the linear elastodynamic problem in anisotropic heterogeneous media. *Geophysics*, 66(1):294–307, 2001.

[53] D. Schaubert, D. R. Wilton, and A. W. Glisson. A tetrahedral modeling method for electromagnetic scattering by arbitrarily shaped inhomogeneous dielectric bodies. *IEEE Trans. Antennas. Propagation.*, 32:77–85, 1984.

[54] F. Shi, W. Choi, E. A. Skelton, M. J. S. Lowe, and R. V. Craster. A time domain finite element boundary integration method for ultrasonic nondestructive evaluation. *IEEE Trans. Ultrason. Ferroelectr. Freq. Control*, 61(12):2054–2066, 2014.

[55] C. A. Balanis. *Antenna Theory: Analysis and Design, 3rd Edition.* John Wiley & Sons, 2005.

[56] C. A. Schultz and M. N. Toksoz. Enhanced backscattering of seismic waves from a highly irregular, random interface: SH case. *Geophys. J. Int.*, 114:91–102, 1993.

[57] S. H. Lo and C. K. Lee. On using different recovery procedures for the construction of smoothed stress in finite element method. *Int. J. Numer. Meth. Engng.*, 43:1223–1252, 1998.

[58] D. J. Payen and K. J. Bathe. The use of nodal point forces to improve element stresses. *Comput. Struct.*, 89:485–495, 2011.

[59] Private communication with Svenska Kullagerfabriken AB (SKF).

[60] C. F. Bohren. Backscattering by non-spherical particles: A review of methods and suggested new approaches. *J. Geophys. Res*, 96(D3):5269–5277, 1991.

[61] N. C. Bruce. Multiple scattering of pulses from randomly rough surfaces. *J. Mod. Opt.*, 46(13):1893–1903, 1999.

[62] N. C. Bruce. Multiple scatter of vector electromagnetic waves from rough metal surfaces with infinite slopes using the Kirchhoff approximation. *Waves Random Media*, 21(2):362–377, 2011.

[63] H. Sun and K. P. Pipe. Perturbation analysis of acoustic wave scattering at rough solid-solid interface. *J. Appl. Phys.*, 111(023510):1–6, 2012.

[64] F. Shi, W. Choi, M. J. S. Lowe, E. A. Skelton, and R. V. Craster. The validity of Kirchhoff theory for scattering of elastic waves from rough surfaces. *Proc. R. Soc. A*, 471:1–19, 2015.

[65] E. Y. Harper and F. M. Labianca. Perturbation theory for scattering of sound from a point source by a moving rough surface in the presence of refraction. *J. Acoust. Soc. Am.*, 57(5):1044–1051, 1975.

[66] E. I. Thorsos and D. R. Jackson. The validity of the perturbation approximation for rough surface scattering using a gaussian roughness spectrum. *J. Acoust. Soc. Am.*, 86(1):261–277, 1989.

[67] C. Eckart. The scattering of sound from the sea surface. *J. Acoust. Soc. Am.*, 25(3):566–570, 1953.

[68] R. D. Kodis. A note on the theory of scattering from an irregular surface. *IEEE Trans. Antennas. Propag.*, 14(1):77–82, 1966.

[69] B. W. Drinkwater and P. D. Wilcox. Ultrasonic arrays for non-destructive evaluation: A review. *NDT & E Int.*, 39:525–541, 2006.

[70] L. W. Schmerr Jr. and S. J. Song. *Ultrasonic Nondestructive Evaluation Systems: Models and Measurements*. Springer, 2007.

List of Publications

[P1] F. Shi, J. E. Michaels, and S. J. Lee. An ultrasonic guided wave method to estimate applied biaxial loads. In D. O. Thompson and D. E. Chimenti, editor, in *Review of Progress in Quantitative NDE*, volume 1430 of *AIP Conference Proceedings*, pages 1567-1574. American Institute of Physics, Burlington, VT, 2011.

[P2] F. Shi, J. E. Michaels, and S. J. Lee. In situ estimation of applied biaxial loads with Lamb waves. *Journal of the Acoustical Society of America*, 133(2):677-687, 2013.

[P3] F. Shi, W. Choi, E. A. Skelton, M. J. S. Lowe, and R. V. Craster. A time domain finite element boundary integration method for ultrasonic non-destructive evaluation. *IEEE Transactions on Ultrasonics Ferroelectrics and Frequency Control*, 61(12):2054-2066, 2014.

[P4] W. Choi, E. A. Skelton, F. Shi, M. J. S. Lowe, and R. V. Craster. Rough surface reconstruction for ultrasonic NDE simulations. In D. O. Thompson and D. E. Chimenti, editor, *Review of Progress in Quantitative NDE*, volume 1581 of *AIP Conference Proceedings*, pages 587-594. American Institute of Physics, Boise, Idaho, 2014.

[P5] F. Shi, W. Choi, M. J. S. Lowe, E. A. Skelton and R. V. Craster. The validity of Kirchhoff theory for scattering of elastic waves from rough surfaces. *Proceedings of Royal Society A*, 471:1-19, 2015.

[P6] F. Shi, W. Choi, E. A. Skelton, M. J. S. Lowe, and R. V. Craster. Investigation of the validity of the elastic Kirchhoff approximation for rough cracks using a finite element approach. In D. O. Thompson and D. E. Chimenti, editor, *Review of Progress in Quantitative NDE*, volume 1650 of *AIP Conference Proceedings*,

pages 1722-1729. American Institute of Physics, Boise, Idaho, 2015.

[P7] F. Shi, M. J. S. Lowe, E. A. Skelton, and R. V. Craster. Transient elastic wave scattering problems by a time domain finite element boundary integral approach. *Journal of Computational Physics*, ready for submission.

[P8] F. Shi, M. J. S. Lowe, X. Xi, and R. V. Craster. Diffuse scattered field of elastic waves by randomly rough surfaces using an analytical Kirchhoff theory. *Journal of the Mechanics and Physics of Solids*, submitted.